The Spatial Distribution of Star Formation in Merging Galaxies

A thesis submitted by

Nicole Jenkins, BSc.

For the award of

Bachelor of Science (Honours)

2025

ABSTRACT

Star formation (SF) is central to galaxy evolution, yet its spatial distribution remains an open question. Using spatially resolved spectroscopy from the SAMI Galaxy Survey, combined with GAMA-derived morphology, environment, and merger classifications, I investigate how mergers and structural features regulate both the location and efficiency of SF.

Merging systems consistently exhibit both enhanced star formation rate (SFR) and specific SFR (sSFR) relative to isolated galaxies, producing broader distributions with extended high activity tails. Radial profiles show that SF is centrally concentrated across all systems, but mergers induce significant enhancements in outer regions, albeit in lower density. Pair separation further modulates activity: the closest pairs display the strongest boosts in SF activity, while widely separated systems exhibit diminished efficiency.

Merger ratio and morphology introduce further complexity. Minor mergers produce the highest median SFR and sSFR, whereas major mergers display the widest spread in SF activity. Bulge-dominated galaxies respond most strongly to interactions, displaying pronounced merger-driven starbursts across the nucleus and intermediate radii. In contrast, late-type systems exhibit moderate enhancements, and early-type galaxies remain largely quiescent. Bars elevate global SF in merging galaxies, but exert little radial influence during mergers compared with isolated systems.

This work demonstrates that mergers enhance star formation across all galactic regions, with the most substantial effects concentrated in nuclear cores and shaped by merger ratio, morphology, and pair separation. These results underscore the importance of spatially resolved analyses in disentangling the diverse pathways through which galaxies grow and transform.

CERTIFICATION OF THESIS

I, Nicole Jenkins, declare that the Honours thesis entitled *The Spatial Distribution of Star Formation in Merging Galaxies* is not more than 15,000 words in length including quotes and exclusive of tables, figures, appendices, bibliography, references, and footnotes. This thesis is the work of Nicole Jenkins except where otherwise acknowledged, with the majority of the contribution to the papers presented as a thesis by publication undertaken by the student. The work is original and has not previously been submitted for any other award, except where acknowledged.

Signed:  Date: 12 December 2025

Endorsed by:

Dr Rebecca McElroy
Principal Supervisor

Student and supervisors' signatures of endorsement are held at UniSQ.

ACKNOWLEDGEMENTS

Firstly, I would like to thank my supervisor, Dr Rebecca McElroy, without whom this work would have been nothing more than a pipe dream. Your encouragement and acceptance of my oddities and strange way of doing things, and your continued lessons that never make me feel like I "should have known that" are things I am forever grateful for.

The support of the SAMI team at Sydney University has been invaluable as well. Without your encouragement, support, and very difficult questions, I would not have learned to think outside the box and consider all possibilities.

My fellow Honours student, Thomas Dunn, has also been a source of unending support and hard questions during our weekly meetings. I appreciate you not only helping me to prepare, but also turning up to every presentation I gave, and for making sure I wasn't the only one a little lost and confused this year.

Lastly, I would like to thank my mostly-patient family and friends, who have had to put up with an awful lot from me this year. You have all reminded me to eat food, drink water, and sometimes extract myself from behind the screen to experience the world a little closer to home than the galaxies I've spent the year pursuing. I know I would not have made it even half as far as I have without each and every one of you.

The UniSQ Toowoomba campus is located on lands of the Giabal and Jarowair peoples. I acknowledge the traditional custodians of the lands where the university is located. Further, I acknowledge the cultural diversity of Aboriginal and Torres Strait Islander peoples and pay respect to elders past, present and future.

TABLE OF CONTENTS

LIST OF FIGURES

LIST OF TABLES

LIST OF ABBREVIATIONS

6df Six-Degree Field 4, 11

AAO Australian Astronomical Observatory 19

AAT Anglo-Australian Telescope 5, 19

AGN Active Galactic Nuclei 1, 4, 7, 12, 15, 42

CALIFA Calar Alto Legacy Integral Field Area Survey 12, 21

DR3 Third Data Release 22

EAGLE Evolution and Assembly of GaLaxies and their Environments 15

FIRE Feedback in Realistic Environments 15

FLAMES Fibre Large Array Multi Element Spectrograph 4

GAMA Galaxy And Mass Assembly 7, 17, 19, 20, 22–24, 28, 37, 40–42, 51, 52

Hα H-alpha 20, 21, 28, 29

Hβ H-Beta 20

HSC Hyper-Suprime Cam 3

IFS Integral Field Spectroscopy 4–6, 11, 12, 17, 19, 21

IFU Integral Field Unit 7, 11, 17

IRAS Infrared Astronomical Satellite 9

KDE Kernel Density Plot . . . . . vi, 38, 39, 41–44

kpc kiloparsec 5, 7, 8, 12, 24, 35, 45

KS Kolmogorov-Smirnov 30, 31, 34, 35

MaNGA Mapping Nearby Galaxies at Apache Point Observatory 12, 21, 52

MUSE Multi-Unit Spectroscopic Explorer 4–6, 12

MWU Mann-Whitney U 30, 31, 34, 35

r/R_e fractional effective radius 28, 31–33, 36, 37, 45

R_e effective radius 5, 23, 28, 29, 31–33, 48

S/N Signal-to-Noise 24, 25

SAMI Sydney-AAO Multi-object Integral field spectrograph . vi, 5, 7, 11, 12, 15–26, 28, 29, 31, 32, 35, 40, 45, 49–52

SDSS Sloan Digital Sky Survey . . . . . vi, 4, 5, 11

SF Star Formation 1, 3, 4, 7–9, 11–17, 19, 21, 22, 24, 27, 28, 30–53

SFMS star-forming main sequence 22, 32, 49

SFR Star Formation Rate . . . . . vi, viii, 4, 7, 8, 12, 14–16, 18, 22, 24, 25, 28–39, 41–52

SNR Signal-to-Noise ratio 24

sSFR Specific Star Formation Rate . . . . . vi, viii, 28, 30, 32–39, 45, 47–50

UniSQ University of Southern Queensland . . . . . ii, iii

UVIT UltraViolet Imaging Telescope 14

VLT Very Large Telescope 4

CHAPTER 1: INTRODUCTION

> There was so much I didn't know. So much I wanted to know. I didn't even know what I wanted to know.
>
> *All Systems Red - The Murderbot Diaries*, Martha Wells

1.1 Star Formation in the Context of Galaxy Evolution

Star Formation (SF) is a central process in galaxy evolution, governing the growth of stellar mass, fuelling chemical enrichment, and influencing the structural evolution of galaxies over cosmic time (Toomre and Toomre 1972; White 1978; Kennicutt and Evans 2012). Although the fundamental mechanisms of SF are broadly understood, questions remain regarding the spatial and temporal conditions under which SF is triggered, particularly in the context of galaxy mergers.

Galaxies are not isolated systems; they are dynamic, evolving through a complex range of internal and external processes. Internally, SF is regulated by mechanisms such as gas heating and cooling, supernovae and Active Galactic Nuclei (AGN), and secular evolution (Bournaud 2011; Chien 2010; Ellison et al. 2013; Das et al. 2023). However, external mechanisms can dramatically influence these internal balances. Among the most transformative of these mechanisms are interactions and mergers, events in which galaxies gravitationally influence or collide with one another, which can dramatically alter morphology, redistribute gas, and ignite intense episodes of SF (Thorp et al. 2019; McElroy et al. 2022; Robin et al. 2024).

Galaxy mergers are a cornerstone of hierarchical evolution, in which smaller structures combine to create larger, more complex structures over time (Figure 1.1; Tinsley and Larson 1979; White and Rees 1978). These events not only reshape galaxies and their dynamics, but also play a critical role in regulating SF. Understanding how mergers modulate SF is essential to construct a coherent picture of galaxy evolution. This enhanced perspective enables astronomers to trace how galaxies assemble mass, undergo structural transformation, and eventually quench their star-forming activity (Moreno et al. 2015; Ellison et al. 2022). In this context, the spatial and temporal distribution of SF serves not as a peripheral detail, but as a diagnostic tool for probing the underlying physical processes that govern galaxy growth and transformation.

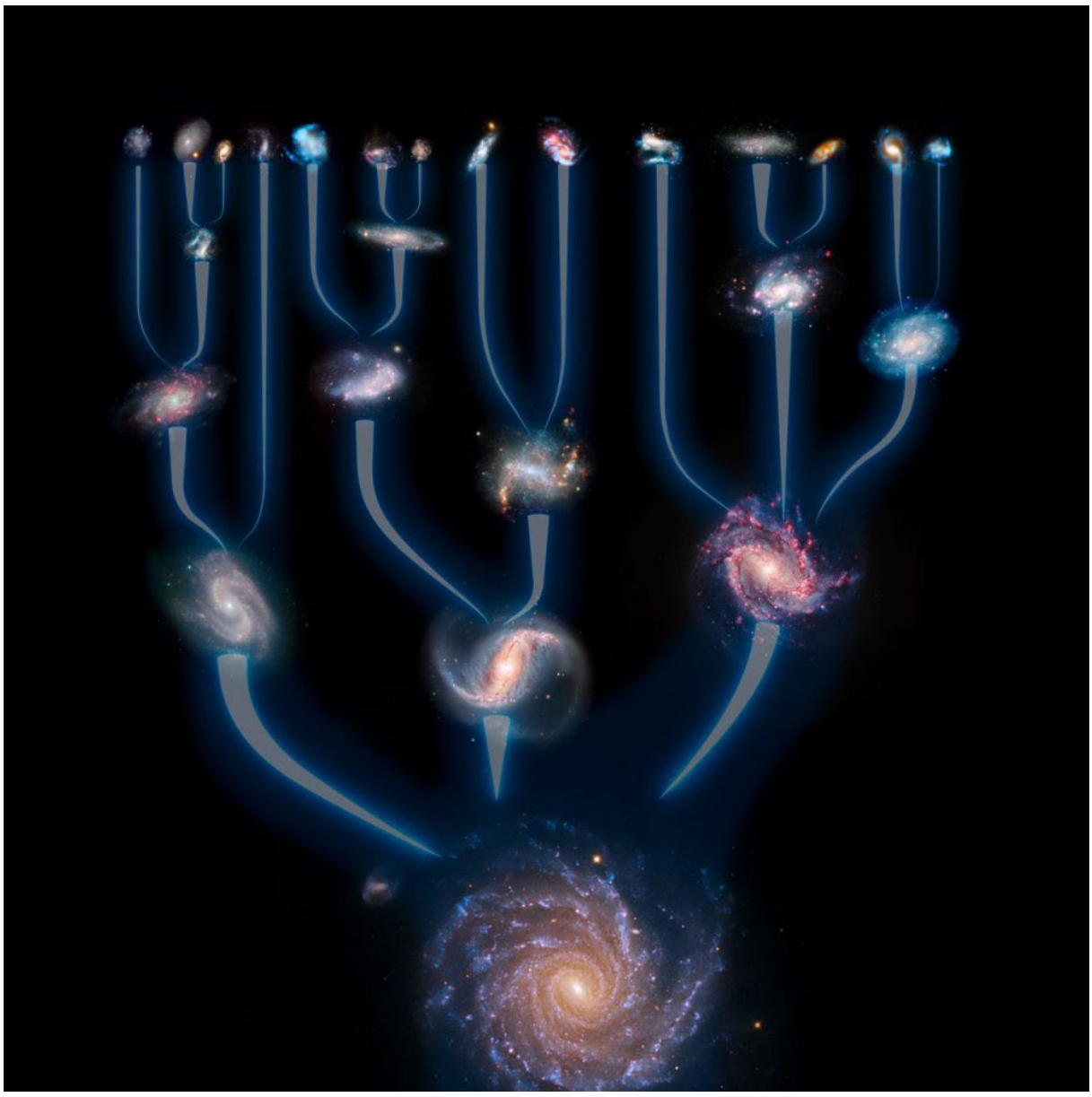

Figure 1.1: Conceptual diagram illustrating hierarchical structure formation, in which galaxies at redshift $z = 0$ are assembled through successive mergers over cosmic time. Each branch represents a progenitor system contributing to the final galaxy, highlighting the cumulative nature of mass assembly and morphological transformation. This framework underpins the role of mergers in shaping galaxy evolution, from early irregulars to mature ellipticals. *Image: ESA/Hubble and NASA (2018).*

1.2 Mergers as Catalysts for Transformation

Galaxy mergers are widely recognised as powerful drivers of galactic transformation, particularly in their ability to trigger SF (Villumsen 1982; Darg et al. 2010b; Oh et al. 2019; Mesa et al. 2021; Das et al. 2023). Decades of observational (Larson and Tinsley 1978; Kennicutt et al. 1987b; Ellison et al. 2013) and simulated (Toomre and Toomre 1972; Mihos and Hernquist 1996; Teyssier et al. 2010) studies have demonstrated that mergers can induce both central starbursts and extended star-forming regions (Mihos and Hernquist 1996; Ellison et al. 2008). However, understanding of the spatial distribution of this activity is incomplete. A key question persists: do mergers primarily concentrate SF in central galactic nuclei (Mihos and Hernquist 1996; Ellison et al. 2013), or do they induce more widespread SF across the disc and in tidal features (Toomre and Toomre 1972; Robin et al. 2024)? This question, followed up in more detail in Chapter 2, is central to understanding how mergers reshape galaxies and influence their evolutionary trajectories.

Figure 1.2: An example of a merging galaxy pair from the SAMI survey: merging galaxies 618993 (left) and 618992 (right). This system exhibits clear signs of interaction, including a tidal bridge linking the pair, bulge growth, and faint shell structures in the primary galaxy. Image: Nicole Jenkins, Hyper-Suprime Cam (HSC) Subaru Telescope.

Mergers profoundly affect galaxy morphology (Thorp et al. 2019), altering dynamics and producing features such as bulge growth, or tidal tails and shells, as illustrated in Figure 1.2. These structures are not only aesthetic; they trace the redistribution of angular momentum and gas, which can funnel material into central regions and ignite intense starbursts (Toomre and Toomre 1972; Saintonge et al. 2012; Thorp et al. 2019; Li et al. 2021). Such inflows are often accompanied by shocks, compression,

and turbulence, further amplifying SF in localised regions.

However, global Star Formation Rates (SFRs) can only offer a coarse measure of this activity. Integrated measures of SFR obscure the underlying spatial complexity, masking whether SF is centrally concentrated, clumpy, or extended across the galactic disc. Spatially resolved analysis, enabled by Integral Field Spectroscopy (IFS), is essential to disentangle the physical mechanisms at play. These include gravitational torques that drive nuclear inflows and lead to central starbursts (Ellison et al. 2013; Medling et al. 2018), feedback from AGN that may suppress or quench SF (Lambas et al. 2012; Ellison et al. 2022; McElroy et al. 2022), and tidal forces that can induce SF in outer regions, including in tidal tails and bridges (Bournaud 2011; Schmidt et al. 2013).

Pinpointing the spatial distribution of SF during mergers is not just a technical exercise. It provides insight into the long-term evolution of galaxies, their chemical enrichment histories, and the mechanisms that govern quenching or rejuvenation. Analyses of past merger events can offer a window into how galaxies like the Milky Way may have evolved through similar interactions.

1.3 Spectroscopy of galaxies

Spectroscopy is one of the most powerful tools in extragalactic astronomy, enabling detailed analysis of galaxy properties such as stellar populations, gas content, kinematics, and SFRs. Large-scale spectroscopic surveys have transformed our understanding of galaxy evolution by providing robust samples across cosmic time. Pioneering efforts such as the Six-Degree Field (6df) Galaxy Survey (Jones et al. 2009) and the Sloan Digital Sky Survey (SDSS, York et al. 2000) collected spectra for hundreds of thousands of galaxies using single-fibre spectroscopy, establishing the foundation for modern extragalactic studies. Their legacy continues through successive generations (e.g. SDSS DR19 (SDSS Collaboration et al. 2025), yet their reliance on single-aperture observations, typically centred on the galactic nucleus, meant that spatial variations within galaxies were averaged out, obscuring internal structure.

The limitations of single-fibre spectroscopy prompted the development of IFS, which revolutionised the field by enabling spatially resolved measurements across multiple regions of a galaxy (Hopkins et al. 2013a). Instead of collapsing spectra into global averages, IFS allows astronomers to take spectra across the face of galaxies, revealing internal dynamics, ionisation structure, and spatially resolved SF (Bryant et al. 2012; Croom et al. 2012). Figure 1.3 illustrates the difference between traditional single-fibre spectroscopy, a single spectrum centred on the galaxy nucleus, and modern hexabundle-based IFS, many spectra taken from across the galaxy. This shift from integrated to resolved measurements has opened new avenues for understanding how galaxies grow, interact, and evolve (Bland-Hawthorn 2016).

The range of IFS instruments have since expanded the scope of resolved galaxy studies. Early systems such as the Fibre Large Array Multi Element Spectrograph (FLAMES) on the Very Large Telescope (VLT) provided versatile multi-object capabilities able to feed up to 132 deployable fibres to individual targets (Pasquini et al. 2002). Modern systems, such as MUSE, which samples continuous fields at fine spatial scales of 0.2" across a 1′ x 1′ field of view, now yield approximately 90,000 spectra per exposure, enabling deep, contiguous 3D spectroscopy of complex fields (Bacon et al. 2010). An example of the

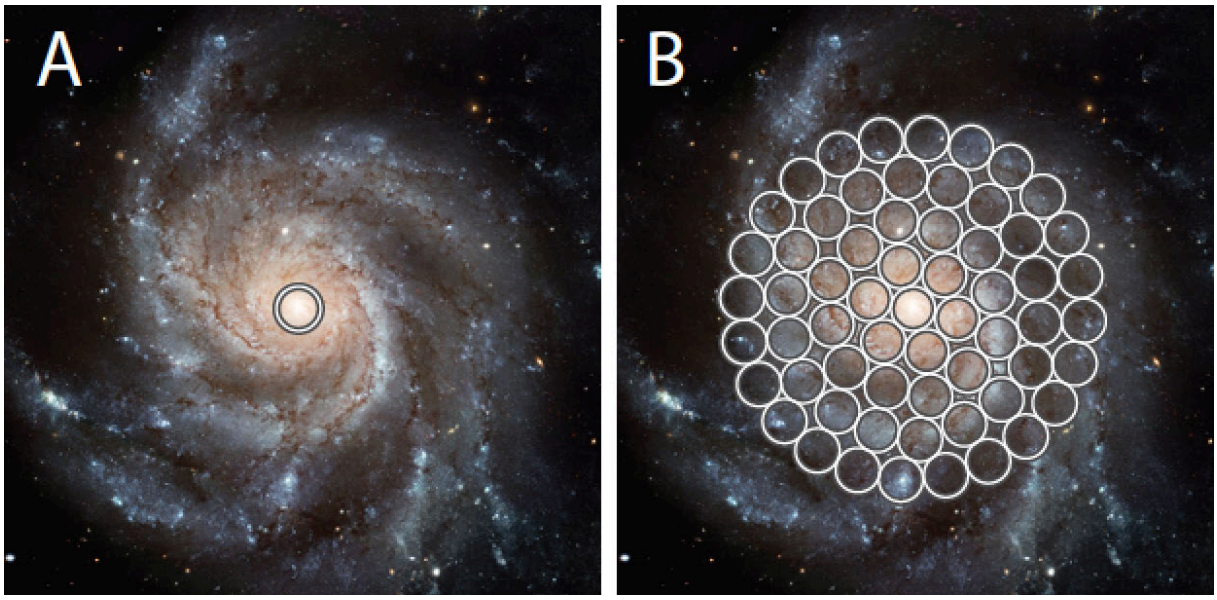

Figure 1.3: Left: depiction of SDSS I single-fibre spectroscopy view. Right: depiction of SAMI 61-hexabundle view. Images: Professor Joss Bland-Hawthorn, Sydney University (Bland-Hawthorn 2016)

high-resolution 3D datacubes produced by MUSE can be seen in Figure 1.4.

The Sydney-AAO Multi-object Integral field spectrograph (SAMI) Galaxy Survey, central to this thesis and outlined in further detail in Chapter 3, represents a pivotal advance in multiplexed IFS. Unlike single-object systems, SAMI uses 13 hexabundles, each composed of 61 tightly-packed fused fibres, to enable simultaneous spatially resolved spectroscopy of 12 galaxies per pointing (Bryant et al. 2012; Croom et al. 2012), increasing survey efficiency. By combining wide-field multiplexing with spatial resolution, SAMI enables statistical studies of thousands of galaxies across diverse environments, bridging the gap between large-scale surveys and detailed internal structure.

Mounted on the 3.9-metre Anglo-Australian Telescope (AAT), each SAMI hexabundle samples a 15 arcsecond diameter field, corresponding to physical scales of ~1 kiloparsec (kpc) at the survey's typical redshifts ($z < 0.095$ for primary targets, $z < 0.115$ for secondary (Croom et al. 2021)). This coverage spans an effective radius (R_e) of approximately 1 - 2 R_e for most galaxies, where R_e is defined as the radius enclosing half the galaxy's total light. This coverage enables the detection of both nuclear and extended star-forming regions. The resulting spectra are processed through the SAMI data reduction pipeline and reformatted into calibrated datacubes, as illustrated in Figure 1.4.

Spatially resolved spectroscopy enables the detailed internal mapping of galaxy properties by capturing emission lines from ionised gas in star forming regions (Sánchez et al. 2012; Zhou et al. 2017), and absorption lines from stellar atmospheres and interstellar material (Scott et al. 2018), allowing insights into stellar populations and intervening gas. These spectral features provide measurements of flux, velocity, and dispersion, enabling analysis of both stellar and gas kinematics, and ionisation conditions in different areas of galaxies.

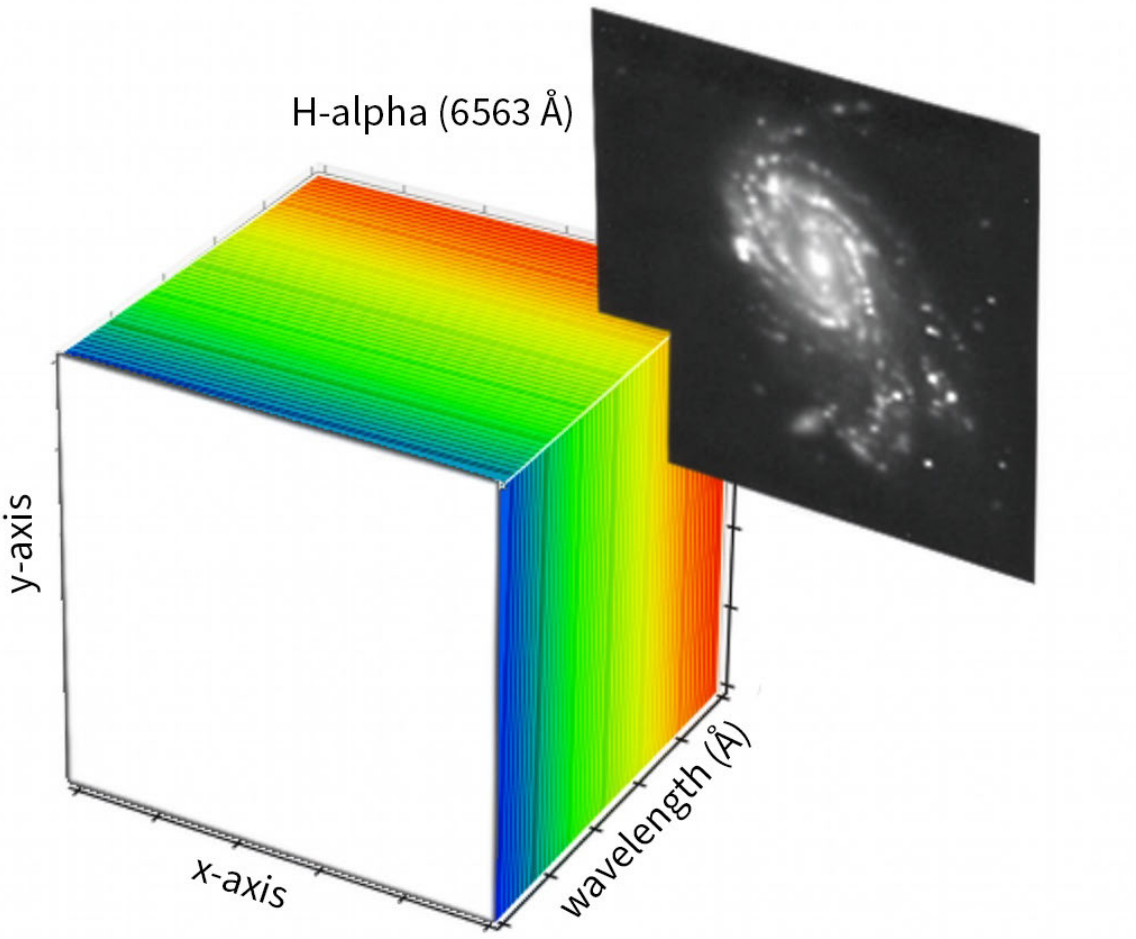

Figure 1.4: Schematic of an IFS datacube using Multi-Unit Spectroscopic Explorer (MUSE) data. We can describe this in two ways. Every pixel on the image shown at the front of the data cube contains a spectrum, or the cube contains images at every wavelength slice. The Hα slice of the datacube shows the detail IFS telescopes such as MUSE are able to achieve per wavelength step when compared to the image on the front of the datacube, at wavelength ~4800 Å. Image: Nicole Jenkins.

Standard value-added products include:

- **Velocity dispersion maps**, which trace the spread in stellar or gas velocities and reveal dynamic structure;
- **Extinction maps**, typically calculated from Balmer decrements (e.g. Hα/Hβ), which quantify dust attenuation;
- **Emission-line diagnostic maps**, used to classify ionisation sources such as SF or AGN via line ratios;
- **SFR maps**, often based on dust-corrected Hα flux and equivalent width measurements.

These products are available across multiple SAMI data releases (Green et al. 2018; Medling et al. 2018; Croom et al. 2021), and can be used in conjunction with environmental metrics such as fifth-nearest-neighbour surface density and cluster-specific indicators from the Galaxy And Mass Assembly (GAMA) catalogue (Driver et al. 2011; Robotham et al. 2011, 2014), allowing studies of how internal galaxy properties vary with environment.

Emission line diagnostics, particularly Hα flux and equivalent width, are used to trace recent SF. These measurements are corrected for dust attenuation using Balmer decrement ratios, and stellar continuum subtraction is performed to isolate nebular emission (Medling et al. 2018; Croom et al. 2021).

The SAMI Galaxy Survey provides a rich dataset for spatially resolved studies of galaxy evolution. Its combination of a sample size of over 3000 galaxies, fine spatial resolution enabled by hexabundle Integral Field Units (IFUs), and broad environmental diversity ranging from isolated field galaxies to dense cluster cores (Croom et al. 2021), makes it uniquely suited to investigating how mergers and interactions influence SF.

1.4 Thesis Scope

This thesis investigates how SF is spatially distributed and environmentally regulated in galaxies undergoing mergers and interactions. Using data from the SAMI Galaxy Survey, I construct a sample of galaxies spanning a range of environments to explore how interactions and local density influence SF patterns. The SAMI dataset, with its spatially resolved spectroscopy and broad environmental coverage, provides an ideal foundation for this analysis.

To contextualise this investigation, Chapter 2 presents a review of the current literature on SF, galaxy interactions, and the role of environment in galaxy evolution. Chapter 3 introduces the SAMI Galaxy Survey and its instrumentation, outlining the data products and catalogues that underpin this study.

This sample used in this thesis is defined through cross-matching SAMI targets with the GAMA survey, which provides robust photometric redshifts, stellar masses, and environmental classifications (Driver et al. 2011; Robotham et al. 2011, 2014). Galaxies are grouped into three categories based on projected separation within 100 kpc, as outlined in Chapter 4. These categories include close pairs and mergers (systems with exactly two members), groups (systems with more than two members), and

isolated galaxies (one member with no companions within 100 kpc). The isolated systems serve as a control sample, providing a baseline against which the effects of interactions and dense environments can be assessed.

This multi-environment framework enables a comparative analysis of SF across different interaction regimes. By examining spatially resolved SFRs within and across these categories, this thesis aims to disentangle the physical processes that trigger, suppress, or redistribute SF during galaxy mergers. The results of this analysis are presented in Chapter 5, which explores how SF varies with environment, merger stage, mass ratio, and morphological features such as bars and tidal structures. Finally, Chapter 6 synthesises these findings in the broader context of galaxy evolution, discussing their implications for models of SF regulation and outlining directions for future research.

CHAPTER 2: LITERATURE REVIEW

Understanding how SF is spatially distributed in merging galaxies requires both observational (Larson and Tinsley 1978; Kennicutt et al. 1987b; Ellison et al. 2013) and theoretical (Toomre and Toomre 1972; Mihos and Hernquist 1996; Teyssier et al. 2010) perspectives. Over the past five decades, advances in instrumentation, survey design, and simulation techniques have transformed our ability to probe the internal structure of galaxies and the physical mechanisms that regulate their evolution (Toomre and Toomre 1972; Bacon et al. 2001; Croom et al. 2012; Ellison et al. 2013; Bundy et al. 2015; Scott et al. 2018; Robin et al. 2024). This chapter reviews key developments in the study of galaxy interactions and SF, with a focus on how spatially resolved spectroscopy and simulations have shaped our current understanding.

2.1 Single-Fibre Surveys and Early Observations

Early observational work, most notably the Arp Atlas of Peculiar Galaxies (Figure 2.1, Arp 1966), provided a photographic catalogue of galaxies with disturbed morphologies and tidal structures. These peculiar systems, with their long tidal tails and bridges, offered some of the first evidence that galaxy interactions could dramatically reshape galaxy structure. Building on this, Toomre and Toomre (1972) used restricted three-body simulations to demonstrate that such tidal features could arise purely from gravitational interactions, suggesting that these structures could host young stellar populations.

Subsequent studies strengthened the picture of mergers as triggers of enhanced SF. Larson and Tinsley (1978) showed that interacting and merging systems exhibit anomalously blue colours, interpreting these as signatures of enhanced or recent SF, while N-body models were further expanded by White (1978), who simulated complete galaxy mergers down to the level of their stellar components and explored the internal structure evolution that follows. Complementary observational work, including the detailed optical and spectroscopic studies of interacting systems by Schweizer (1987), provided independent evidence for widespread SF in tidally disturbed galaxies. In the same year, Kennicutt et al. (1987b) statistically linked tidal encounters to elevated SF in galaxy pairs. These early simulation and observational studies established the foundational framework for understanding how galaxy interactions trigger star formation and morphological transformation.

While the observational and theoretical basis for merger-induced starbursts was established in the 1970s and 80s, it wasn't until the advent of space-based infrared astronomy that these predictions were directly confirmed. The launch of the Infrared Astronomical Satellite (IRAS) in 1983 marked a turning point in research, enabling the detection of dust-obscuring starbursts and dramatically expanding the observational dataset (Soifer et al. 1984; Sanders et al. 1986). However, IRAS lacked the

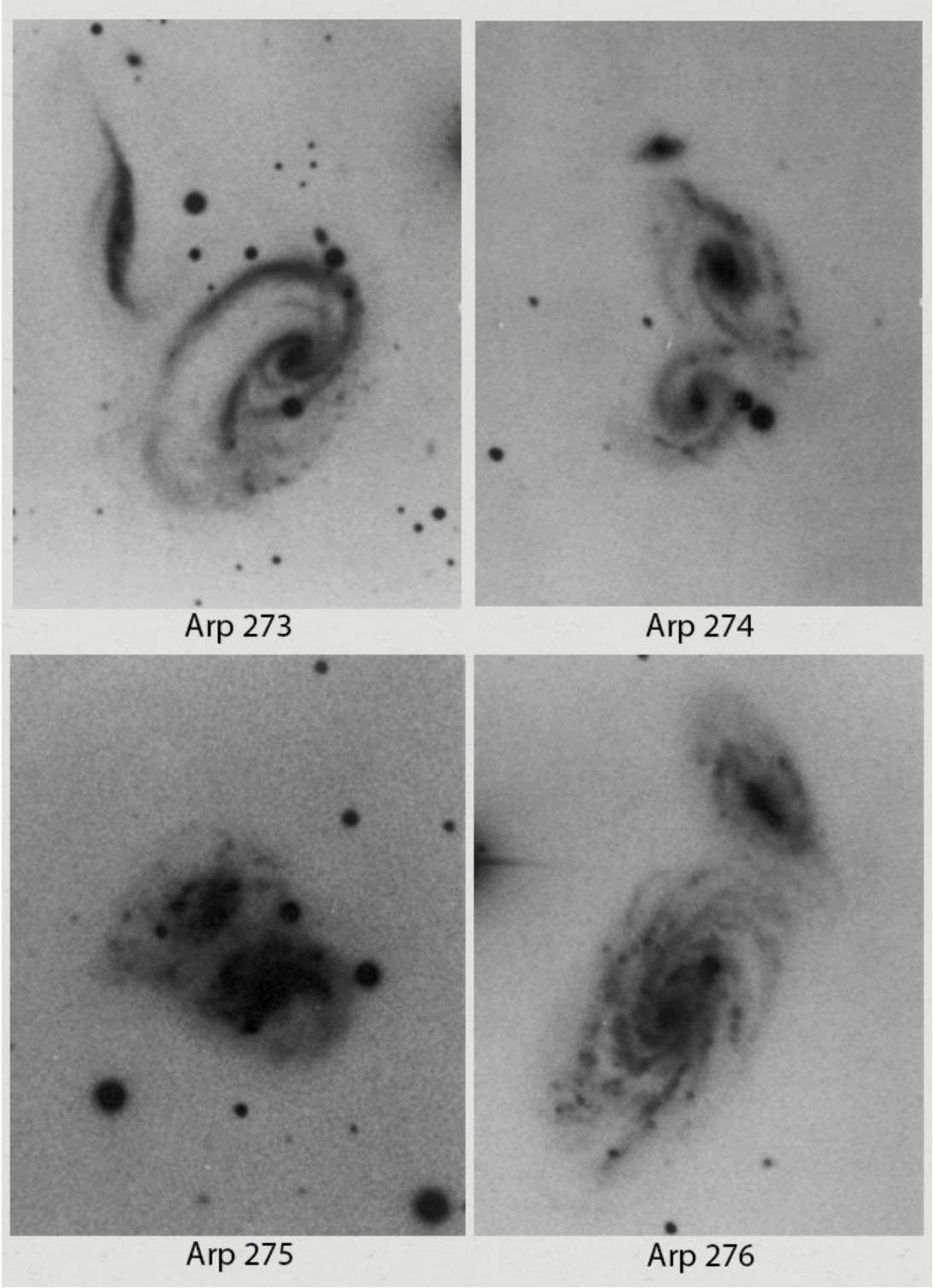

Figure 2.1: Photographic plates from the Arp Atlas of Peculiar Galaxies (Arp 1966), showcasing galaxies with disturbed morphologies and tidal structures. Arp 273 (larger: UGC 1810, smaller: UGC 1813) features long tidal tails stretching between the two galaxies and twisted spiral arms in the larger galaxy. Arp 274 (NGC 5679 Group) shows three closely spaced galaxies which exhibit irregular and clumpy star-forming regions. Arp 275 (NGC 2881) exhibits a distorted spiral galaxy with a visibly warped disk and lopsided spiral arms. Arp 276 (larger: NGC 935, smaller: IC 1801) shows a clean spiral structure in the larger galaxy, with minimal visible distortion and well-defined arms, but a clear smaller companion galaxy. *Image credits: (Arp 1966)*

spatial resolution to pinpoint where within galaxies this SF was occurring, providing only integrated measurements of global activity (Neugebauer et al. 1984; Soifer et al. 1987).

Large-scale spectroscopic surveys such as the 6df Galaxy Survey (Jones et al. 2009) and SDSS (York et al. 2000) expanded the statistical reach of galaxy studies. These surveys relied on single-fibre spectroscopy, typically sampling only the central regions of galaxies. As a result, they provided robust global diagnostics, but potentially missed SF in outer discs, tidal structures, and merging edges (Kewley et al. 2005; Iglesias-Páramo et al. 2013). Despite this limitation, SDSS has remained a cornerstone of extragalactic astronomy, with successive data releases such as the most recent DR19 (SDSS Collaboration et al. 2025), continuing to refine our understanding of galaxy interactions and SF across vast samples.

2.2 The Rise of Integral Field Spectroscopy

The limitations of single-fibre surveys led to the development of IFS, which enables spatially resolved measurements across the face of galaxies. Traditional single-aperture spectroscopy samples only a narrow central region, while long-slit observations capture one spatial dimension per exposure. Reconstructing full two-dimensional structures requires multiple pointings, often demanding substantial integration time, an approach that is both time-consuming and impractical for large samples. By contrast, IFS produces three-dimensional datacubes containing a full spectrum at every spatial pixel, or spaxel, allowing detailed mapping of physical properties like SF, gas kinematics, and ionisation structure across galaxies in unprecedented detail (Sánchez et al. 2012; Fogarty et al. 2014; Drory et al. 2015).

Early generations of IFS instruments, such as the Traitement Intégral des Galaxies par l'Étude de leurs Rayonnements (TIGER, Bacon et al. 1995), and the Spectroscopic Areal Unit for Research on Optical Nebulae (SAURON, Bacon et al. 2001; Bureau et al. 2002) demonstrated the transformative potential of spatially resolved spectroscopy for galaxy studies. These instruments revealed complex internal structures such as kinematic misalignments and spatially varying SF histories that could not be inferred from one-dimensional or centrally-weighted spectra. The advent of wide-field monolithic IFUs, most notably the Calar Alto Legacy Integral Field Area Survey (CALIFA, Sánchez et al. 2012), provided high-quality datacubes for hundreds of galaxies, further showcasing the value of spatially resolved diagnostics. However, these pioneering surveys were limited by their relatively modest sample sizes, restricting their ability to draw statistically robust conclusions about galaxy populations (Allen et al. 2015; Bundy et al. 2015).

A major technological breakthrough came with the development of hexabundles, tightly fused fibre bundles with high fill factors designed specifically for low-light astronomical applications (Bland-Hawthorn et al. 2011). By reducing fibre cladding thickness and optimising the packing geometry, hexabundles provide efficient spatial sampling while maintaining low cross-talk and high throughput. This innovation enabled multiplexed IFS on survey-scales for the first time, allowing multiple galaxies to be observed simultaneously and directly paving the way for instruments such as SAMI (Bland-Hawthorn et al. 2011; Croom et al. 2012; Bryant et al. 2015), discussed in more detail in Chapter 3.

The advent of large IFS surveys such as SAMI (Croom et al. 2012; Bryant et al. 2015) and Mapping Nearby Galaxies at Apache Point Observatory (MaNGA, Bundy et al. 2015), and the further devel-

opment of wide-field instruments like MUSE (Bacon et al. 2010) has since revolutionised the field. Combining large sample sizes with high spatial resolution, these surveys enable systematic studies of galaxy evolution across diverse environments, providing new insights into the spatial distribution of SF, the role of environment in shaping galaxy properties, and the interplay between stellar populations and gas dynamics (Medling et al. 2018; Erroz-Ferrer et al. 2019; Croom et al. 2021; Fraser-McKelvie et al. 2021; Li et al. 2021).

2.3 Star Formation in Mergers: Observational Trends

2.3.1 Nuclear Star Formation

Observational and simulated work over several decades have consistently shown that galaxy interactions can drive strong enhancements in nuclear SF, primarily through gas inflows and gravitational torques (Mihos and Hernquist 1996; Springel et al. 2005; Hopkins et al. 2013b; Barrows et al. 2017). Early simulations showed that tidal interactions destabilise gas in the discs of both galaxies, funnelling it into the central kpcs and potentially igniting nuclear starbursts (Hernquist 1989; Barnes and Hernquist 1991). Foundational models like these established the physical picture of gas losing angular momentum during interactions, resulting in rapid central concentration of cold gas.

Later generations of high-resolution hydrodynamic simulations incorporating stellar and AGN feedback confirmed and expanded this picture, showing that merger-driven inflows produce intense, short-lived bursts of SF predominantly in the central regions (Mihos and Hernquist 1996; Springel et al. 2005; Hopkins et al. 2013b). Work by Hopkins et al. (2013b) and Moreno et al. (2015) demonstrated that the majority of new stars form *in situ* within the nuclear region rather than migrating inward from the disc. Additional simulation studies also revealed that the efficiency of nuclear starbursts depends on orbital geometry, gas fraction, disc structure, and spin alignment between the merging galaxies (Moreno et al. 2015)

Observationally, a wealth of evidence supports enhanced nuclear star forming activity in close galaxy pairs and interacting systems. Spectroscopic surveys have shown elevated central SFRs at projected separations of less than 30 kpc (Ellison et al. 2008, 2013), often accompanied by increased central metallicities indicative of gas inflows and mixing (Kewley et al. 2006; Scudder et al. 2012). Spatially resolved IFS surveys such as CALIFA, MaNGA and SAMI have provided direct maps of centrally concentrated SF in interacting galaxies (Barrera-Ballesteros et al. 2015; Schaefer et al. 2017; Thorp et al. 2019; Petersson et al. 2023). Despite strong convictions of centrally-peaked starbursts in merging systems, both Thorp et al. (2019) and Petersson et al. (2023) also noted variations in the outer regions, suggesting a complex and non-uniform spatial response.

Subsequent research has reinforced the expectation that mergers can induce intense SF, primarily through gas inflows and the associated turbulence and compression (Mihos and Hernquist 1996; Bournaud 2011; Ellison et al. 2013; Gordon et al. 2025). However, starbursts are frequently accompanied by elevated AGN activity (Di Matteo et al. 2005; Ellison et al. 2013; Barrows et al. 2017; Baron et al. 2024), with evidence for a temporal offset between the peak of SF and the onset of AGN enhancement. Delays ranging from ~0.16 Gyr to nearly 1 Gyr have been reported (Di Matteo et al. 2005; Barrows et al. 2017), suggesting an evolutionary sequence in which gas inflows first trigger central star-

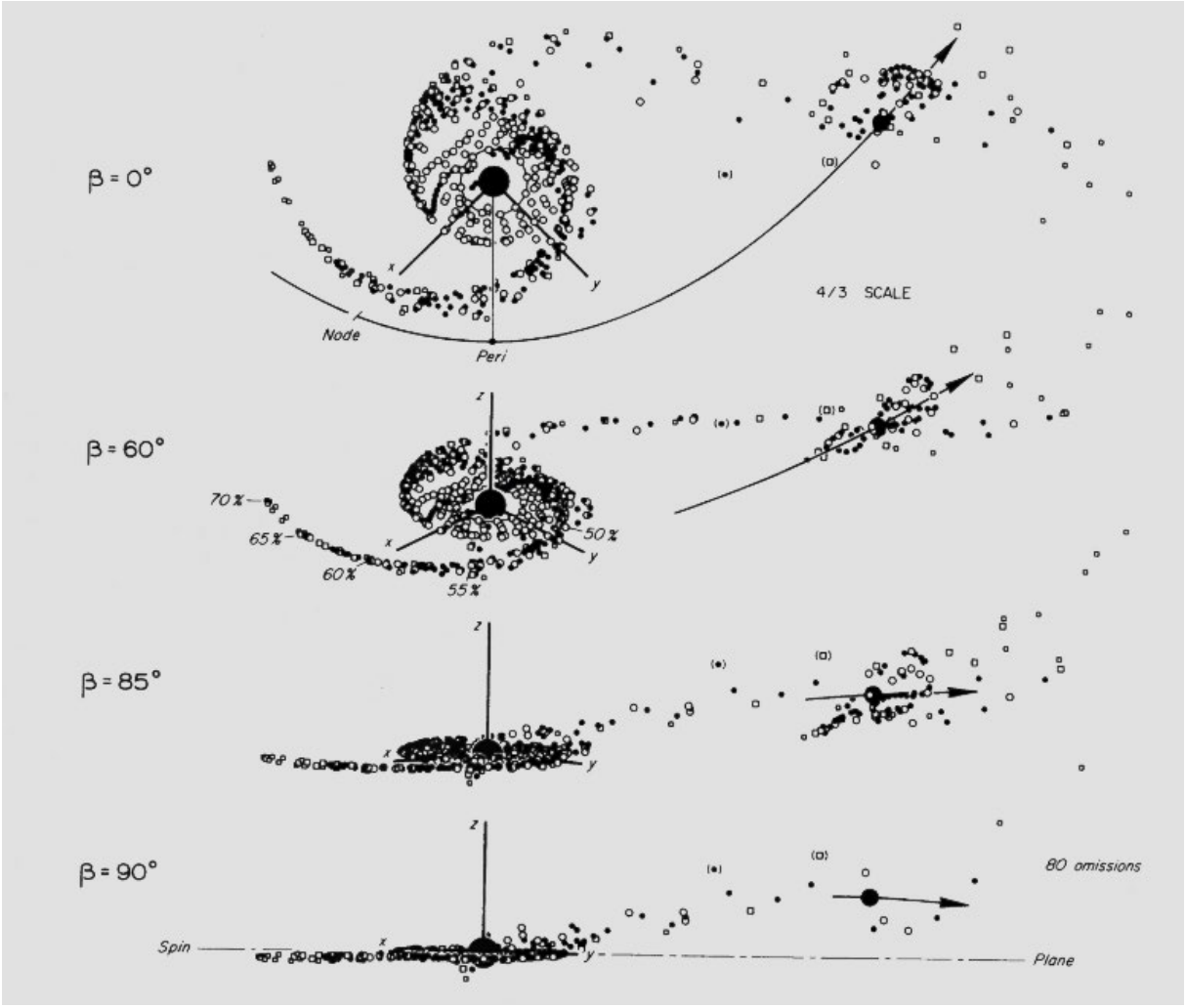

Figure 2.2: Simulated model of Arp 295 shown from various observational angles, β, with $i = 15°$ and $\omega = 45°$, and a mass ratio of 1:4. This simulation shows the enhanced galactic activity postulated by Toomre and Toomre (1972) to be SF in the tidally-connected tails of each galaxy. *Image: (Toomre and Toomre 1972)*

bursts, followed by black hole growth once sufficient gas reaches the nucleus. Feedback processes may then suppress rather than enhance SF in some systems (Medling et al. 2018; Ellison et al. 2022). These findings highlight the importance of considering both temporal and spatial separation in interpreting SF trends.

2.3.2 Peripheral Star Formation in Tidal Features

While nuclear starbursts are well documented, a growing body of evidence points to SF in the outer regions of merging galaxies. Toomre and Toomre (1972) first proposed that "oddly placed absorbing material and/or emitting regions" in tidal tails and bridges of Arp galaxies (Arp 1966) could indicate peripheral SF, as shown in the simulation example in Figure 2.2. This has since been supported by observations of blue tidal features and disc-wide SF in spiral mergers (Kennicutt et al. 1987a; Darg et al. 2010a). Darg et al. (2010a) also suggested that spiral morphologies are more conducive to extended SF than ellipticals.

Shock-induced SF in tidal features has been observed in young stellar clusters with ages and metal-

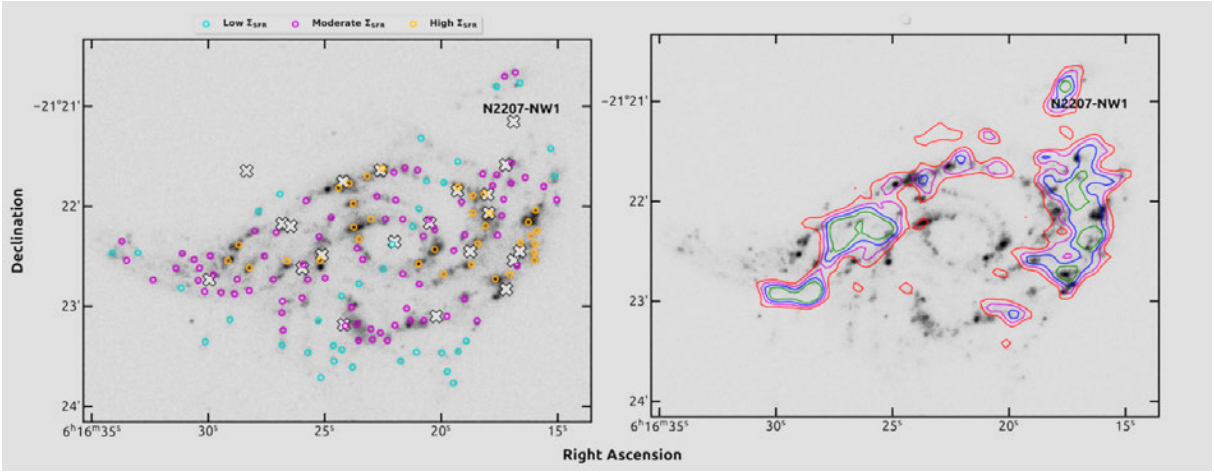

Figure 2.3: Left: $\sum_{SFR}$ spatial distribution plot shown in the merging galaxy pair NGC 2207 and IC 2163. This system showcases the high SFR in yellow compared to the large mass ratio difference between the two galaxies. Right: The column density contour plot of H_I overplotted on the FUV image of the merging galaxy pair. Images: (Robin et al. 2024)

licities consistent with in-situ formation triggered by tidal compression (Chien 2010). UV imaging from the UltraViolet Imaging Telescope (UVIT) has confirmed widespread star-forming regions in tidal arms and bridges (Robin et al. 2024). Statistical analysis of tidal features in galaxies have further demonstrated that morphological disturbances correlate strongly with starburst activity. In a recent study, Gordon et al. (2025) found that faint tidal features are ten times more likely to be in a starburst phase than mass-matched controls, with arm-like bridging features particularly associated with elevated SF. These findings underscore the importance of tidal morphology in the spatial distribution of merger-induced SF.

2.3.3 Distributed and System-Wide Star Formation

Beyond the nuclear-peripheral dichotomy, several studies suggest that SF in mergers can be widespread and system-dependent (Moreno et al. 2015; Schaefer et al. 2017; Thorp et al. 2019; Moreno et al. 2021; Petersson et al. 2023). Bournaud (2011) proposed two mechanisms: radial gas inflow to fuel nuclear starbursts, and turbulence-driven fragmentation to trigger extended SF. Observations show that global SF peaks near the first pericentric passage, declines during separation, and rises again during final coalescence (Ellison et al. 2013; Barrows et al. 2017; Thorp et al. 2019; Petersson et al. 2023; Gordon et al. 2025).

Morphology and mass ratio also play key roles. Gas-rich spiral-spiral mergers exhibit stronger starbursts than gas-poor early-type systems (Ellison et al. 2008; Petersson et al. 2023), and the presence of bars or bulges can modulate gas transport efficiency (Mihos and Hernquist 1996; Moreno et al. 2015). Robin et al. (2024) found that higher mass ratios correlate with lower SF enhancement, whereas Lambas et al. (2012) reported that major mergers are roughly twice as efficient at boosting SF as minor mergers. These apparently contrasting results likely reflect differences in sample selection and the definition of mass ratio. While Lambas et al. (2012) emphasised the classic major/minor split, Robin et al. (2024)'s analysis suggests that equal-mass encounters may not always yield the strongest enhancement, depending on gas content and structural properties.

Beyond these trends, merger type itself exerts a strong influence. Major mergers (mass ratios of 1:1 to 1:4), minor mergers (1:4 - 1:10), dwarf mergers (1:10 - 1:100), and satellite accretion (mass ratios > 1:100) each exhibit distinct patterns in SFR, spatial distribution, and the likelihood of quenching (Woods and Geller 2007; Darg et al. 2010a; Lambas et al. 2012; Das et al. 2023; Bottrell et al. 2024). Moreno et al. (2021) further demonstrated that SF enhancement is not uniform across merging systems, with secondary galaxies showing more nuclear concentration and primaries exhibiting broader radial distribution. Importantly, Pearson et al. (2019) found that mergers do not universally enhance SF relative to isolated galaxies, except in systems already above the star-forming main sequence.

2.4 Simulations and Theoretical Models

Theoretical work has been essential in interpreting observational evidence of merger-driven SF. By compressing billion-year evolutionary processes into manageable timescales, simulations offer a dynamic lens through which to study gas inflows, starburst triggering, and feedback regulation during galaxy interactions (McElroy et al. 2022; Bottrell et al. 2024).

Early N-body models showed that gravitational torques during interactions drive gas inflows and central starbursts (Toomre and Toomre 1972; Villumsen 1982; Barnes and Hernquist 1991). These foundational models established the physical picture of angular momentum loss and central gas concentration. Modern hydrodynamical simulations incorporate feedback, AGN physics, and detailed thermodynamics, enabling more realistic predictions of SF patterns (Hopkins et al. 2013b; Moreno et al. 2021; Feldmann et al. 2023; Bottrell et al. 2024).

Recent cosmological simulation suites such as Feedback in Realistic Environments (FIRE), Evolution and Assembly of GaLaxies and their Environments (EAGLE), and IllustrisTNG have extended these models to statistically robust samples across a range of environments and redshifts (Moreno et al. 2021; McElroy et al. 2022; Feldmann et al. 2023; Bottrell et al. 2024). Forward-modelling techniques, such as those used in TNG50 (Nelson et al. 2019), allow for the creation of synthetic observations that can be directly compared with survey data. A sample of this simulated data is presented in Figure 2.4, depicting a subset of galaxies from TNG50 selected for forward modelling. Each galaxy in the sample contains at least 10^4 stellar particles, enabling detailed analysis of merger histories and SF forecasts over compressed timescales (Bottrell et al. 2024).

These simulations help explain the diversity of observed outcomes in merging systems showing how orbital geometry, gas fraction, and feedback processes shape whether SF is concentrated in the nucleus or distributed across tidal features. They provide detailed temporal predictions of starbursts peaks and AGN delays offering a theoretical framework for interpreting survey data from instruments like SAMI (Moreno et al. 2021; Feldmann et al. 2023).

2.5 Open Questions

The spatial distribution of SF in merging galaxies remains an open and evolving question. While some systems exhibit intense nuclear starbursts, others show widespread or peripheral enhancement, and many display a combination of both. These outcomes appear to depend on a complex interplay of factors, including mass ratio, gas content, merger stage, and internal morphology.

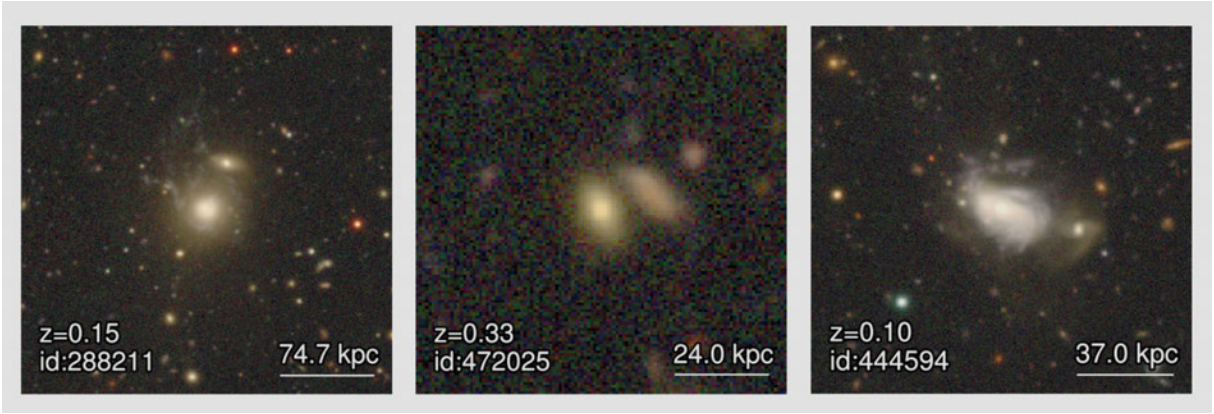

Figure 2.4: A sample of synthetic near-UV/optical/near-IR images created using dust radiative transfer post-processing with SKIRT as part of TNG50 forward modelling. These simulations investigate the link between SFR and galaxy mergers. Images: Connor Bottrell (Bottrell et al. 2024)

Rather than conforming to a singular spatial archetype, SF in mergers reflects a range of outcomes shaped by the physical conditions and dynamic histories of the systems involved. This thesis builds on these findings by using spatially resolved spectroscopy from the SAMI Galaxy Survey to investigate how SF is distributed across interacting, clustered, and isolated galaxies, with the goal of disentangling the physical processes that govern SF in dynamically complex environments.

CHAPTER 3: THE SAMI GALAXY SURVEY

This thesis uses data from the SAMI Galaxy Survey and supporting data from the GAMA survey. These datasets provide spatially resolved spectroscopy and robust multi-wavelength ancillary information respectively, enabling a comprehensive analysis of galaxy SF across diverse environments.

3.1 SAMI Instrument

The SAMI instrument combines the multiplexing efficiency of a multi-object spectrograph with the spatial resolution and mapping capabilities of an IFS. Designed as a survey-grade instrument, SAMI enables simultaneous, spatially-resolved observations of multiple galaxies, facilitating high-throughput studies of internal galaxy structure, kinematics, and ionisation conditions across large samples (Croom et al. 2012; Bryant et al. 2015).

3.1.1 Instrument Design

The scientific motivations behind SAMI shaped its architecture and survey strategy (Bland-Hawthorn et al. 2011; Croom et al. 2012; Bryant et al. 2015). The key science goals proposed by the SAMI team were designed to answer the following questions:

- What is the physical role of environment in galaxy evolution?
- What is the relationship between stellar mass growth and angular momentum development in galaxies?
- How does gas get into and out of galaxies, and how does this drive SF?

These goals necessitated a system capable of both high spatial resolution and a large survey volume, which was a combination not feasible with previous IFU instruments (Bacon et al. 2001; Allen et al. 2015; Bundy et al. 2015). The resulting solution was the first scalable, wide-field multiplexed IFS system built for systematic galaxy evolution studies.

3.1.2 Hexabundles and Fibre System

SAMI is equipped with 13 fused fibre bundles, known as hexabundles, outlined in Section 2.2 (Bland-Hawthorn et al. 2011) and shown in Figure 3.1. Each hexabundle comprises 61 optical fibres arranged

in a circular configuration with a 15-arcsecond diameter covering a 1-degree field of view on the sky, enabling spatially resolved spectroscopy across multiple regions of a galaxy. Twelve hexabundles are allocated to observe galaxies, with one reserved for calibration (Croom et al. 2012), a configuration that enables multiplexed spatially resolved spectroscopy.

The hexabundles transmit light to AAOmega, a dual-beam spectrograph capable of medium spectral resolution across a broad wavelength range (Smith et al. 2004; Sharp et al. 2006). In the standard SAMI setup, the system is configured with the 580V and 1000R gratings, providing a wavelength coverage of 3700 - 5700 Åin the blue arm (R ~ 1700) and 6300 - 7400 Åin the red arm (R ~ 4500) (Smith et al. 2004; Croom et al. 2012; Bryant et al. 2015). This wavelength range covers important features used to derive stellar populations, SFR, and gas kinematics, and emission line fluxes (e.g., Hα, Hβ, [OIII], [NII], [SII]).

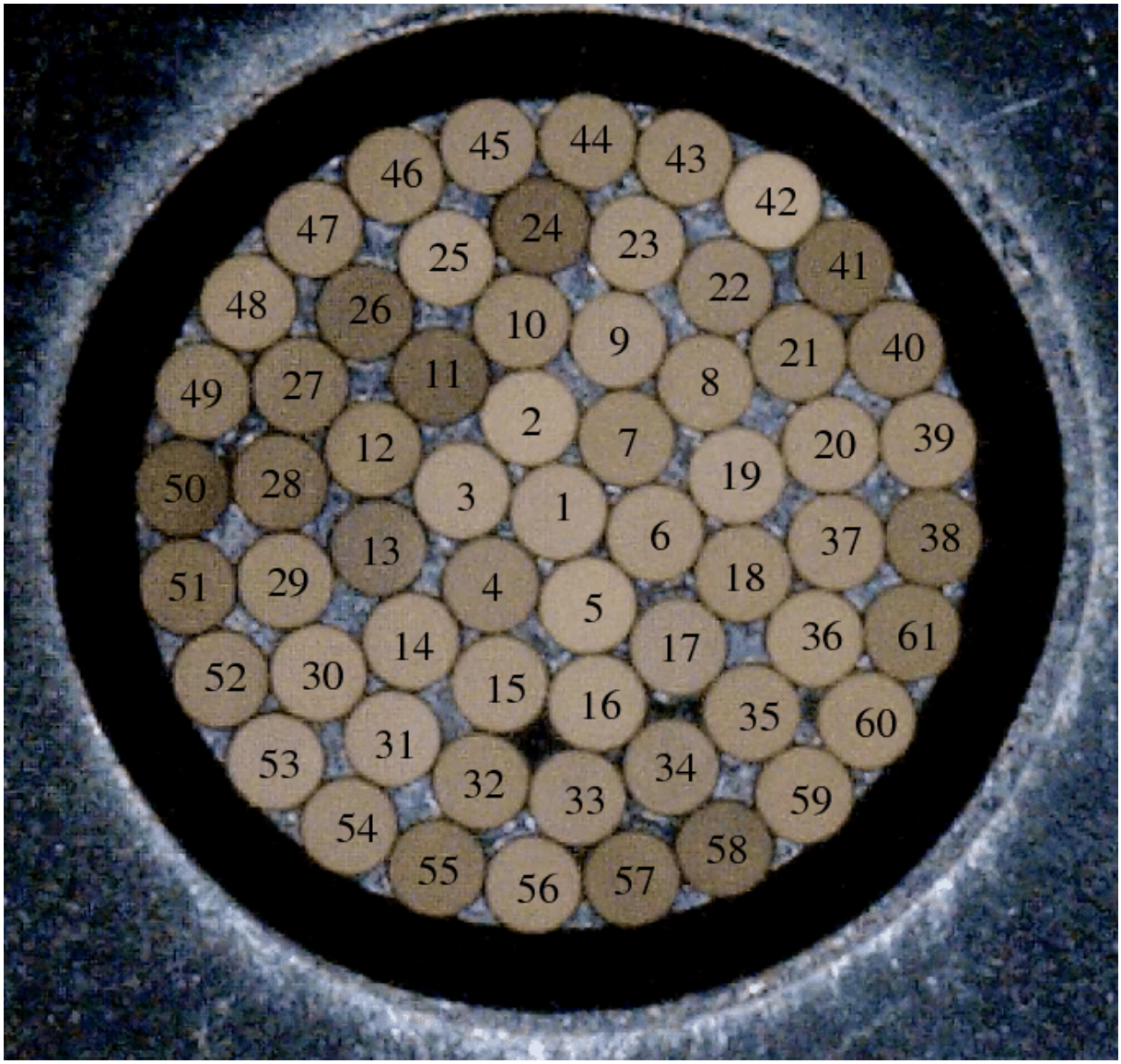

Figure 3.1: The front face of one of the 61-core hexabundles on the SAMI Instrument. The cores are 105 μm in diameter, combining to provide the 15" aperture that gives a 1° field of view on the sky. *Image: Joss Bland-Hawthorn (Bryant et al. 2012)*

3.1.3 Installation and Observing Environment

SAMI was installed on the 3.9-metre Anglo-Australian Telescope at Siding Spring Observatory in Coonabarabran, NSW, in July 2011, with the initial prototype progressing from first light to reduced spectra within nine months, publishing early results in (Fogarty et al. 2014). The AATs wide 1-degree field of view, combined with its excellent guiding and tracking stability, makes it well suited to multi-object spectroscopy.

3.1.4 Transition to Hector

The conclusion of the SAMI Galaxy Survey marked a pivotal moment in Australian IFS. SAMI, with its innovative hexabundle fibre technology (Bland-Hawthorn et al. 2011), successfully delivered spatially resolved spectroscopy for over 3,000 galaxies across diverse environments (Fogarty et al. 2014; Scott et al. 2018; Fraser-McKelvie et al. 2021). Building on this success, the Australian Astronomical Observatory (AAO) initiated development of *Hector*, the next-generation multiplexed IFS instrument for the AAT.

Hector represents a significant expansion in capability. While SAMI deployed 13 hexabundles with 61 fibres each, Hector introduces larger hexabundles, a new fibre positioning system, and upgraded spectrographs designed to increase efficiency and precision (Bryant et al. 2020; Zhelem et al. 2020; Mohanan et al. 2022; Bryant et al. 2024) These improvements enable Hector to target up to 15,000 galaxies, or five times the statistical sample achieved by SAMI, while also employing broader wavelength coverage with both the AAOmega legacy spectrograph ($R1700$ in the blue arm and $R4500$ in the red arm) and the new *Spector* spectrograph ($R5000 - 7000$) and enhanced spectral resolution (Bryant et al. 2020; Zhelem et al. 2020; Mohanan et al. 2022; Bryant et al. 2024).

The transition from SAMI to Hector reflects both continuity and innovation. SAMI demonstrated the scientific power of multiplexed IFS, producing landmark results on galaxy kinematics, SF, and environmental quenching (Schaefer et al. 2017; Scott et al. 2018; Tuntipong et al. 2024). Hector extends this legacy by scaling up the sample size, improving the field of view of the instrument, and increasing the spectral resolution.

3.2 The GAMA Survey

The GAMA survey provides the photometric and spectroscopic backbone for the SAMI target selection. GAMA is a highly complete ($\geq 98\%$) multi-wavelength spectroscopic survey designed to provide a uniform and statistically powerful foundation for studies of galaxy evolution (Driver et al. 2011). GAMA combines deep optical spectroscopy with extensive ancillary data spanning the ultraviolet to the radio, producing one of the most comprehensive extragalactic datasets available (Driver et al. 2011; Hopkins et al. 2013a).

GAMA covers three equatorial fields (G09, G12, G15) and two southern fields (G02, G23), totalling $\sim$286 deg^2, and provides spectroscopic redshifts for over 300,000 galaxies down to $r < 19.8$ mag (Driver et al. 2016). The survey's exceptionally high redshift completeness makes it ideal for environmental studies.

For this thesis, GAMA provides the global measurements and catalogue data needed to contextualise the spatially resolved SAMI observations. In particular, GAMA offers:

- Accurate redshifts and spectral measurements (Liske et al. 2015);
- Stellar masses, photometry, and structural parameters (Taylor et al. 2011; Kelvin et al. 2012);
- Group and environment catalogues (Robotham et al. 2011).

These data products ensure that the SAMI sample is embedded with robust statistical framework spanning galaxy mass, morphology, and environment. This embedding is particularly valuable because it allows individual SAMI galaxies to be interpreted in the context of a well-characterised parent population, ensuring that trends observed in the integral-field data can be linked to global properties with minimal bias. GAMA's high completeness and uniform selection make it especially well-suited as the parent catalogue for the SAMI Galaxy Survey (Bryant et al. 2015; Croom et al. 2021).

3.3 The SAMI Galaxy Survey

The SAMI Galaxy Survey commenced in March 2013 and concluded in May 2018, producing a final sample of 3068 galaxies across a wide range of environments (Bryant et al. 2015; Croom et al. 2021). Targets were selected from the GAMA survey (Driver et al. 2011) and complementary cluster catalogues, ensuring coverage of field, group, and cluster environments. The survey spans a redshift range of $0.004 < z < 0.095$ and a stellar mass range of $10^{8.5}$ - $10^{11.5}$ $M_{\odot}$, enabling statistically robust comparisons across diverse galaxy populations.

3.3.1 Multiplexed IFS and Survey Efficiency

One of the defining features of SAMI is its ability to observe 12 galaxies simultaneously, dramatically improving survey throughput. This multiplexed design enables large-scale resolved studies that were previously impractical due to the time requirements of single-object spectrographs. It also reduces susceptibility to aperture bias and to obscured spatial variations caused by collapsing spectra into global averages (York et al. 2000; Bland-Hawthorn et al. 2011; Driver et al. 2011).

3.3.2 Data Products and Public Releases

Three major SAMI data releases contain reduced data, derived maps, and value-added catalogues (Allen et al. 2015; Green et al. 2018; Croom et al. 2021). These releases represent one of the most comprehensive sets of integral field spectroscopy products available for nearby galaxies, enabling both targeted case studies and large-scale statistical analyses. The data products include:

- flux-calibrated datacubes (one red, one blue, corresponding to the two arms of the AAOmega spectrograph);
- emission-line flux maps (H-alpha (Hα), H-Beta (Hβ), [NII], [SII], etc.);
- stellar kinematics and velocity dispersion fields;

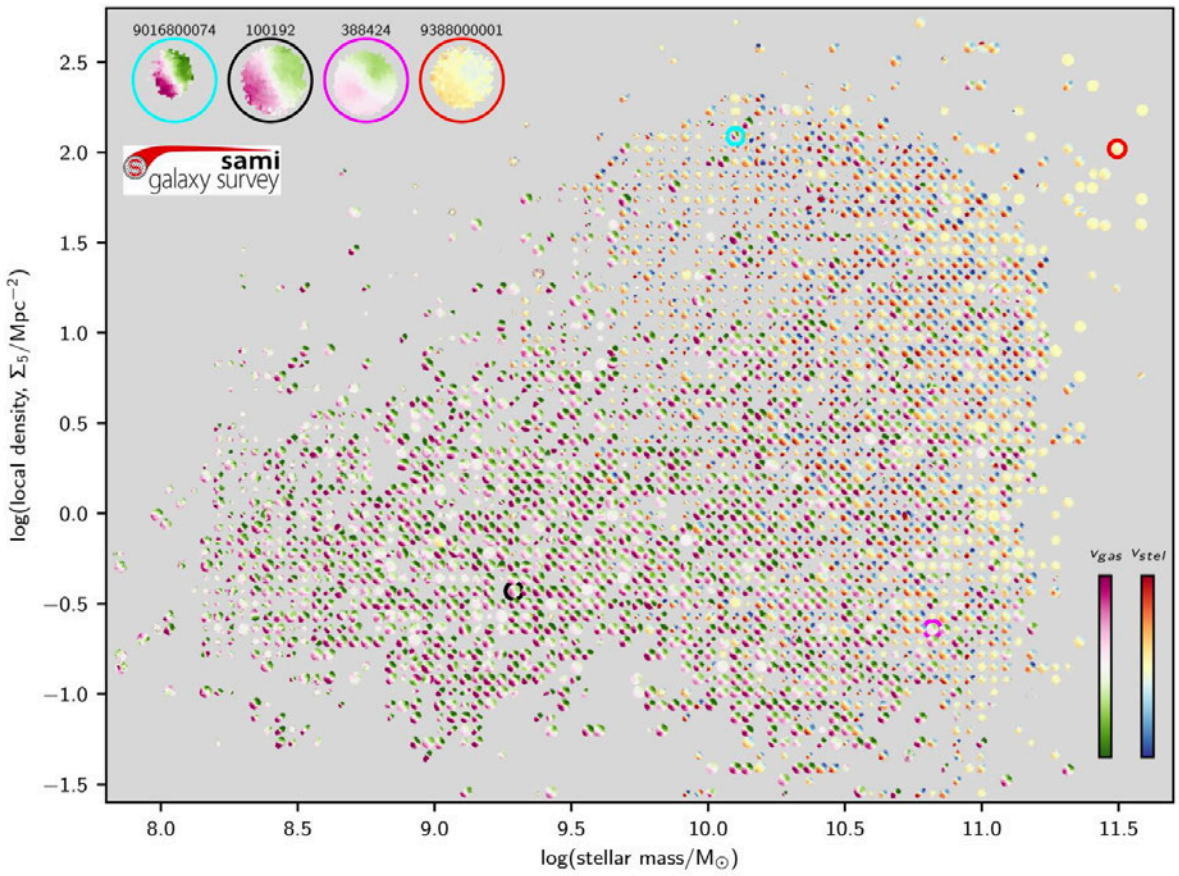

Figure 3.2: The full SAMI sample mapped in stellar mass and local density space, with colour indicating the ratio of gas to stellar velocity. This map helps contextualise the environments and dynamical states of the galaxies under study. *Image: SAMI DR3 (Croom et al. 2021)*

- ionised gas kinematics and diagnostic maps;
- aperture spectra and global measurements.

Each release has progressively expanded the scope and quality of the survey, with improvements in calibration, sky subtraction, and value-added catalogues (Allen et al. 2015; Green et al. 2018; Croom et al. 2021), such as the example shown in Figure 3.2. These products have formed the basis for studies of galaxy kinematics, chemical enrichment, and environmental effects, as outlined in Subsection 3.3.3. The public availability of SAMI data ensures reproducibility and facilitates cross-survey comparisons with other IFS programs such as CALIFA and MaNGA (Fraser-McKelvie et al. 2021).

3.3.3 Key Results from SAMI

The scientific impact of the SAMI Galaxy Survey is reflected in a series of landmark results that demonstrate the power of multiplexed IFS for understanding galaxy evolution. By providing spatially resolved spectroscopy across thousands of galaxies, SAMI has enabled analyses that move beyond global measurements to reveal the internal processes shaping galaxies.

One of the most significant outcomes has been the identification of environmental quenching signatures. Spatially resolved Hα maps reveal suppressed SF in satellite galaxies, with clear radial gradients

linked to local density and group environment (Schaefer et al. 2017). These results highlight how environment influences SF not only globally, but also within galaxy disks.

SAMI data has also helped establish robust scaling relations between galaxy structure and stellar populations. Scott et al. (2017) demonstrated that stellar age and metallicity vary systematically across the size-mass plane, providing new constraints on pathways from star-forming disks to quenched spheroids. Complementary work by Brough et al. (2017) showed that mass is the primary driver of the kinematic morphology-density relation in clusters, with the fraction of slow rotators increasing strongly with stellar mass. Together, these studies emphasise the interplay between mass, morphology, and environment in shaping galaxy evolution.

The survey's kinematic products have further demonstrated how internal dynamics regulate SF efficiency. Stellar velocity fields and dispersion maps revealed systematic trends between kinematic support and a galaxy's position on the star-forming main sequence (SFMS), which describes the tight correlation between stellar mass and SFR in star-forming galaxies, providing a benchmark against which elevated or suppressed activity can be measured (Ellison et al. 2011; Tacchella et al. 2015), and underscores the role of dynamical structure in regulating SF (Fraser-McKelvie et al. 2021).

SAMI has also enabled systematic studies of galactic winds. Ho et al. (2016) identified extraplanar ionised gas and outflows in galaxies with recent SF, linking the presence of winds to SF history and demonstrating their role in regulating galaxy growth. This work highlighted the ability of SAMI to detect feedback processes across a statistical sample.

Finally, SAMI has provided criteria for identifying Milky Way analogues within the local galaxy population. By combining spatially resolved SF and kinematic diagnostics, the survey has enabled comparative studies of our Galaxy's place in the broader population, offering a benchmark for models of disk galaxy evolution (Tuntipong et al. 2024).

Together, these results demonstrate the breadth of SAMI science. From environmental processes to internal kinematics, feedback mechanisms, and population analogues. They form a foundation for the expanded statistical depth of Hector, ensuring continuity in addressing key questions of galaxy evolution.

3.4 Data used in this thesis

The Third Data Release (DR3), used in this thesis, includes the full 3068-galaxy sample and is accessible through Australian Astronomical Optics' Data Central portal (DataCentral 2025). To establish environmental classifications, I cross-referenced the SAMI sample with the GAMA Pairs Catalogue (Robotham et al. 2014), obtaining counts for pair galaxies. Galaxies with exactly one partner were classified as *Pairs*, while galaxies with multiple companions were classified as *Groups*. Galaxies that did not match any entry in the GAMA Pairs Catalogue were classified as *Isolated*.

Additional global properties were then incorporated into each subset by matching SAMI identifiers to the corresponding entries in the relevant value-added catalogues. These included the GAMA Stellar Mass Catalogue (Taylor et al. 2011) and Input Catalogue (Driver et al. 2011), as well as the SAMI Morphology Catalogue (Tuntipong et al. 2024). A detailed description of this process is provided in Chapter 4.

CHAPTER 4: DATA ANALYSIS

The data analysis in this thesis was conducted in `Python`, using standard astronomical and statistical libraries including `numpy` (Harris et al. 2020), `astropy` (Astropy Collaboration et al. 2013, 2018), `pandas` (Wes McKinney 2010), `scipy` (Virtanen et al. 2020), and `matplotlib` (Hunter 2007). Unless otherwise stated, all code was developed by me for the purposes of this thesis.

4.1 Interacting and Isolated Galaxies

As outlined in Section 3.3, the initial SAMI DR3 contained 3068 galaxies observed by the SAMI instrument. To support later analysis, additional parameters were incorporated from several SAMI and GAMA catalogues. Stellar masses were obtained from the GAMA Stellar Mass Catalogue (Taylor et al. 2011), while R_e were drawn from the GAMA Environment Measures Catalogue (Robotham et al. 2011).

Morphological information was added from two sources. The SAMI Morphology Catalogue (Tuntipong et al. 2024) provided indicators of structural features and interaction phases, including:

- **Strong Bar:** The presence of a strong bar;
- **Weak Bar:** The presence of a weak bar;
- **LSB Companion:** The presence of a low surface-brightness companion;
- **Merger:** A galaxy having two systems that are very close or a disturbed single system;
- **Interaction:** A galaxy showing signs of an interaction, such as tidal tails or disturbance, but still considered a separate galaxy;
- **Shells/Asymmetry:** A galaxy consisting of shells or asymmetry, including merger remnants.

In addition, the GAMA Morphology Catalogue (Driver et al. 2022) provided a complementary classification scheme. The raw catalogue distinguishes between early-type systems **(E)**, bulge-dominated systems with compact or diffuse bulges **(cBD, dBD)**, late-type systems **(D)**, compact galaxies **(C)**, and hard to determine cases **(H, HE)** that are difficult to classify due to asymmetry or multiple cores, as well as fragments **(FRAG)** and stellar contaminants **(STAR)**. For statistical analysis, these subcases were merged into three broad categories:

- **E (Early-type Group):** Combination of galaxies classified as E, HE, and C

- **D (Late-type Group):** Combination of galaxies classified as D and H
- **BD (Bulge-Dominated Group):** Combination of galaxies classified as cBD and dBD

Compact systems were assumed by Driver et al. (2022) to be poorly resolved early-types, while HE systems were treated as multiple-cored early-types. H classifications with hard asymmetric systems were assumed to be disturbed late-types. FRAG and STAR entries were excluded. This merged scheme provides a consistent classification across the SAMI sample, yielding 1136 BD galaxies, 283 E galaxies, and 456 D galaxies, with the remaining 1193 galaxies lacking morphology codes and therefore labelled as **Unclassified.**

To investigate how galaxy interactions influence SF among mergers, the sample was then partitioned into environmental categories by cross-matching SAMI galaxy identifiers with the GAMA Pairs Catalogue (Robotham et al. 2014). These categories were defined as:

- **Pairs:** 106 unique galaxies with exactly one companion within 100 kpc.
- **Groups:** 522 unique galaxies with two or more companions within 100 kpc.
- **Isolated:** 2440 unique galaxies with no companions within 100 kpc.

The Pairs and Groups subsets form the test population for assessment, while the Isolated subset provides the control galaxies.

4.2 Quality Control

To ensure data reliability of SFR measurements, several quality control measures were applied to the SAMI FITS files across all three environmental samples.

4.2.1 Signal-to-Noise Filtering

A Signal-to-Noise ratio (SNR) cut was applied to the SFR FITS files at the spaxel level, excluding individual spaxels with SNR < 4. Below this threshold, emission-line fluxes become unstable, and derived quantities have large errors. Galaxies were then excluded from the sample if they did not contain a sufficient number of spaxels meeting the Signal-to-Noise (S/N) ≥ 4 criterion. This approach provides a balance between maximising sample size and retaining integrity in the measurements, consistent with recommended SAMI quality thresholds (Bryant et al. 2015; Green et al. 2018).

After S/N filtering, the working sample was reduced to 2371 galaxies, comprising:

- **Pairs:** 98 galaxies;
- **Groups:** 418 galaxies;
- **Isolated:** 1855 galaxies.

4.2.2 Pixel Filtering

In addition to the S/N threshold, galaxies whose SFR maps contained fewer than 50 spaxels were excluded. Systems with limited spatial coverage cannot provide reliable radial profiles or region-based statistics, as the derived quantities are dominated by noise rather than genuine structure.

Figure 4.1 compares two galaxies, the left with only 31 valid pixels and the right with over 700. The low-pixel case produces a patchy heatmap and lacks any determinable structure, while the radial profile is erratic, with a clear artificial spike. In contrast, the high-pixel galaxy on the right exhibits a coherent heatmap with a clear central feature and smooth radial decline, mirrored in its radial profile.

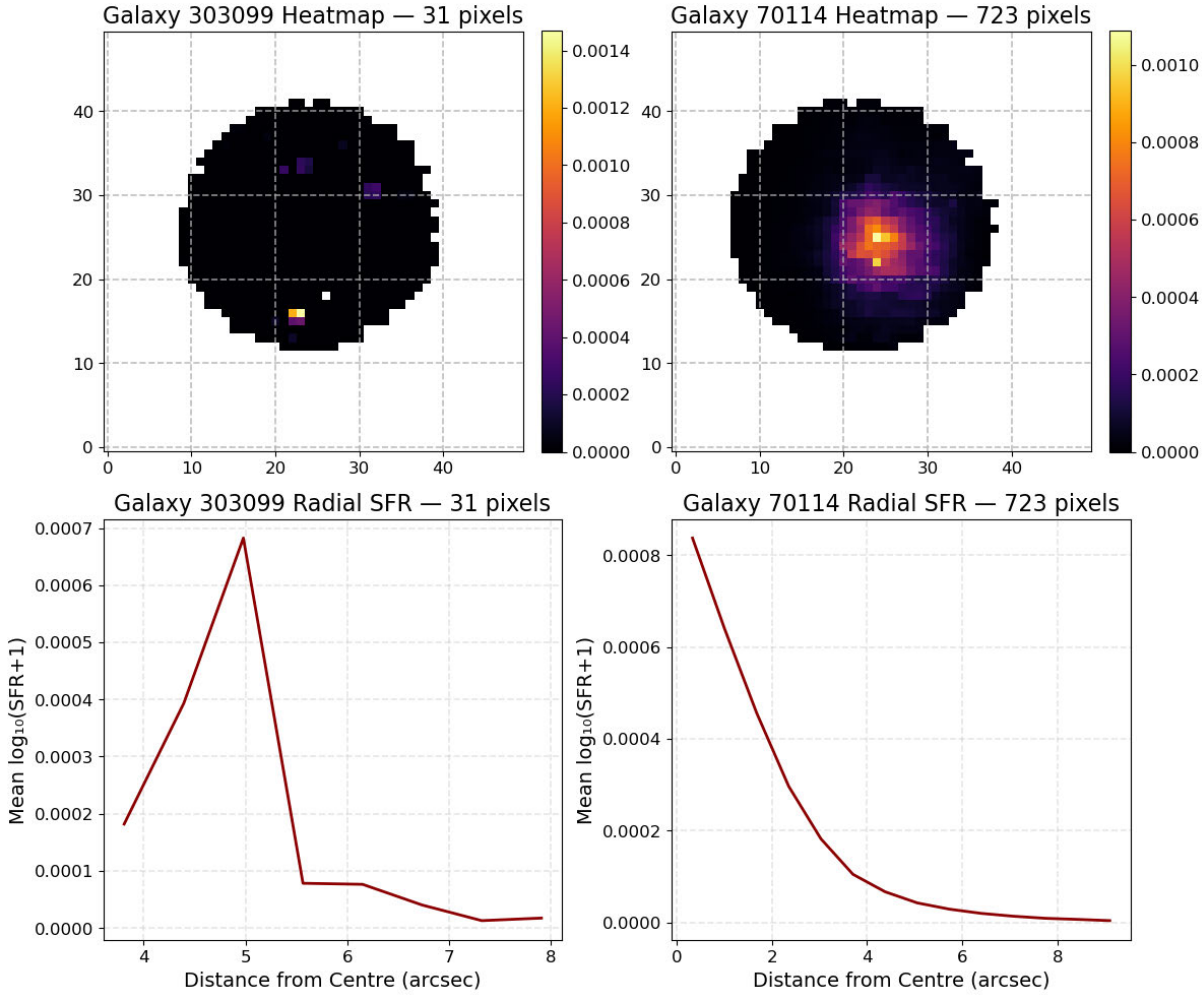

Figure 4.1: Comparison of two SAMI galaxies illustrating the impact of pixel count on radial SFR analysis. Left panels: Galaxy 303099 with only 31 valid pixels, producing a patchy heatmap and an erratic radial profile with an artificial central spike. Right panels: Galaxy 70114 with 723 valid pixels, showing a coherent heatmap with a clear central feature and a smooth radial decline. These examples demonstrate the necessity of pixel count thresholds for reliable spatial analysis.

After adopting a balanced cutoff of 50 pixels, the working sample was reduced to 1306 galaxies:

- **Pairs:** 80 galaxies.
- **Groups:** 197 galaxies.

- **Isolated:** 1029 galaxies

4.2.3 Group Verification

The final quality-control step was group verification, to ensure morphological consistency across the sample. Using the SAMI Morphology Catalogue (Tuntipong et al. 2024), which identified galaxies across the SAMI sample with features consistent with mergers or interactions, an additional 391 galaxies originally classified as **Isolated** were found to exhibit tidally-disturbed morphologies. Despite lacking nearby companions, these systems showed evidence of recent mergers or interactions, and were reclassified into a new **Interacting** category alongside the existing **Pairs** galaxies.

Figure 4.2 illustrates an example of reclassification. SAMI Galaxy 77967, initially classified as Isolated, was reclassified as Interacting after morphological assessment revealed features consistent with a recent merger.

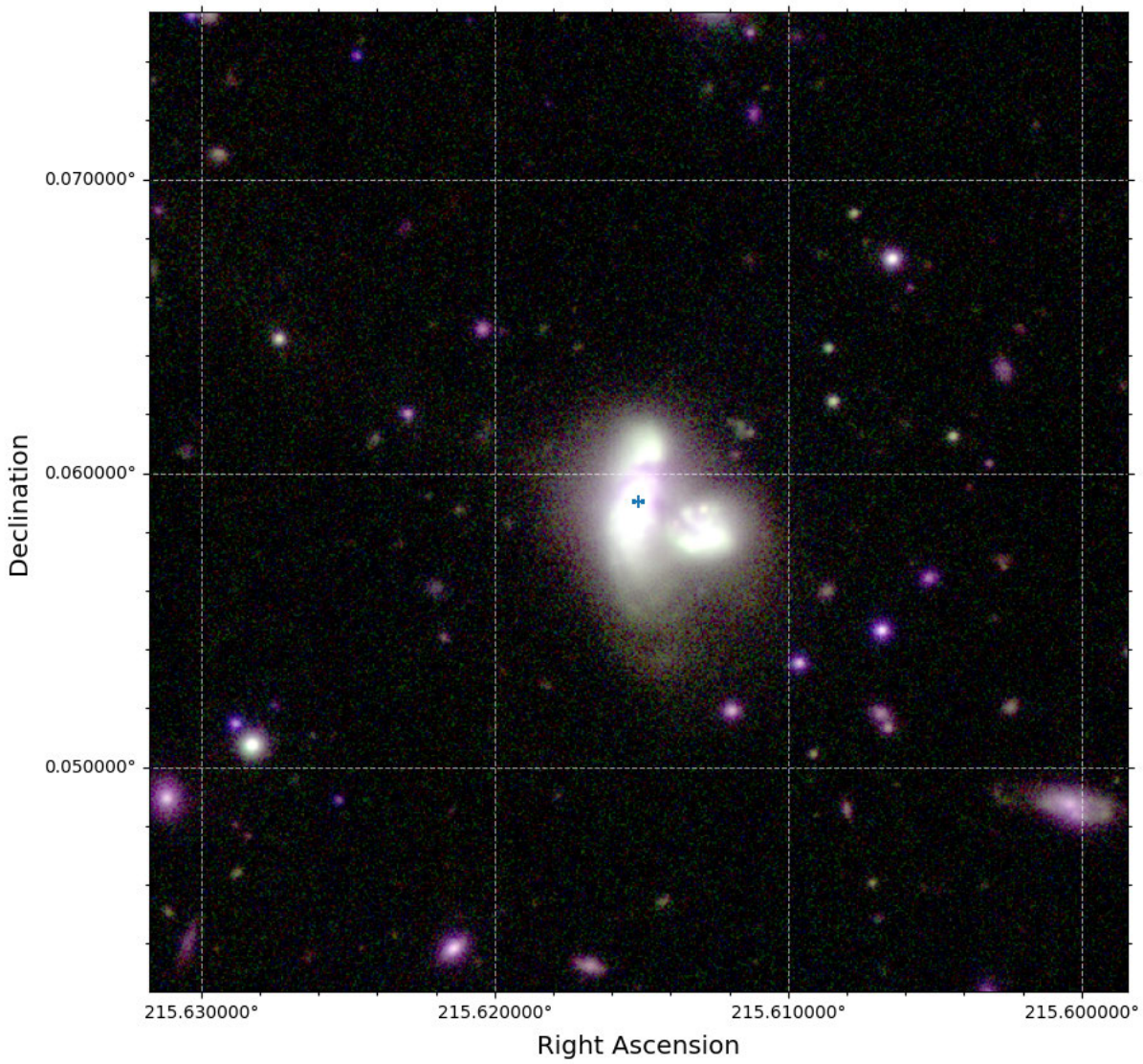

Figure 4.2: SAMI Galaxy 77967, originally classified as an Isolated galaxy with no nearby neighbours, this galaxy was reclassified as an Interacting galaxy after morphological assessment noted features consistent with a recent merger. *Image: de Jong et al. (2015).*

After group verification and reclassification, the working sample comprised:

- **Interacting:** 471 galaxies
- **Groups:** 197 galaxies
- **Isolated:** 638 galaxies

4.2.4 Working Sample

Initial analysis of the data found that SF and kinematic properties of the galaxies in the Pairs and Groups subsets were remarkably similar. Trends across both categories were consistent, and the statistical separation between them was minimal. As a result, I combined the Groups sample into the Interacting sample for the remainder of the analysis. This allowed for a cleaner comparison between the Interacting systems and Isolated controls, while preserving statistical power.

The final working sample consists of:

- **Interacting:** 668 galaxies
- **Isolated:** 638 galaxies

4.3 Pairs Mass Ratio

Galaxy interactions span a wide range of mass scales, from equal-mass collisions to the accretion of tiny satellites. To quantify this diversity within the Interacting sample, I calculated the stellar mass ratio for each pair. For the 144 galaxies in the Interacting sample with close partners, the stellar mass ratio was calculated as:

$$\text{Mass Ratio} = \frac{M_{\text{primary}}}{M_{\text{secondary}}} \tag{4.1}$$

The primary galaxy was defined as the more massive of the two. Based on this ratio, the Pairs were classified into four categories:

- Major Merger (1:1 - 1:4)
- Minor Merger (1:4 - 1:10)
- Dwarf Merger (1:10 - 1:100)
- Satellite Accretion (> 1:100)

Applying this scheme to the Interacting sample yields 72 major mergers, 39 minor mergers, 29 dwarf mergers, and 4 satellite accretion systems. This distribution shows that major mergers dominate the Interacting sample, while extreme ratios like satellite accretions are rare in this data. Additionally, no galaxies in the Interacting sample were flagged as having low surface brightness companions (LSB

Comp, Tuntipong et al. 2024). The dominance of major mergers reflects both their observational visibility and their dynamical impact, which makes them easier to identify in surveys. By contrast, the scarcity of extreme ratios such as satellite accretions highlights an observational bias. Their absence underscores the observational difficulty of detecting such faint systems, and suggests that satellite accretions may be under-represented in catalogues despite their expected frequency in hierarchical models (e.g. Bottrell et al. 2024).

4.4 The Data

To probe SF activity across the SAMI sample, several derived data products were generated. These products provide both spatial and radial perspectives on SF, enabling comparisons across environments and morphologies.

First, Hα flux, SFR, and gas velocity dispersion maps were created to visualise the internal structure of individual galaxies, as shown in Figure 4.3. These maps illustrate the distribution of ionised gas and highlight regions of enhanced SF, forming the basis for subsequent radial segmentation analyses.

Radial profiles were then computed by binning spaxels in concentric annuli centred on each galaxy. Distances were initially measured in arcseconds, as provided by the SAMI dataset. To enable comparison across galaxies of different sizes, profiles were normalised by R_e, from the GAMA Environment Measures Catalogue, producing fractional effective radius (r/R_e) profiles. This normalisation allows galaxies of varying physical scales to be compared on a common footing. An example of these can be seen in Figure 5.2 in Chapter 5.

Each galaxy's SFR distribution was further segmented into four regions:

- Central (0 - 0.5 R_e)
- Mid (0.5 - 1.0 R_e)
- Outer (1.0 - 2.0 R_e)
- Outer 2 (2.0 - 3.0 R_e)

For each region, the total, mean, and median SFR values were calculated.

Finally, I computed the Specific Star Formation Rate (sSFR) as a mass-normalised measure of activity:

$$\mathrm{sSFR} = \frac{\mathrm{SFR}}{\mathrm{M}_*} \tag{4.2}$$

M_* is the stellar mass of the galaxy, determined from the GAMA Stellar Mass Catalogue. This parameter provides a direct comparison of SF efficiency across galaxies of different masses.

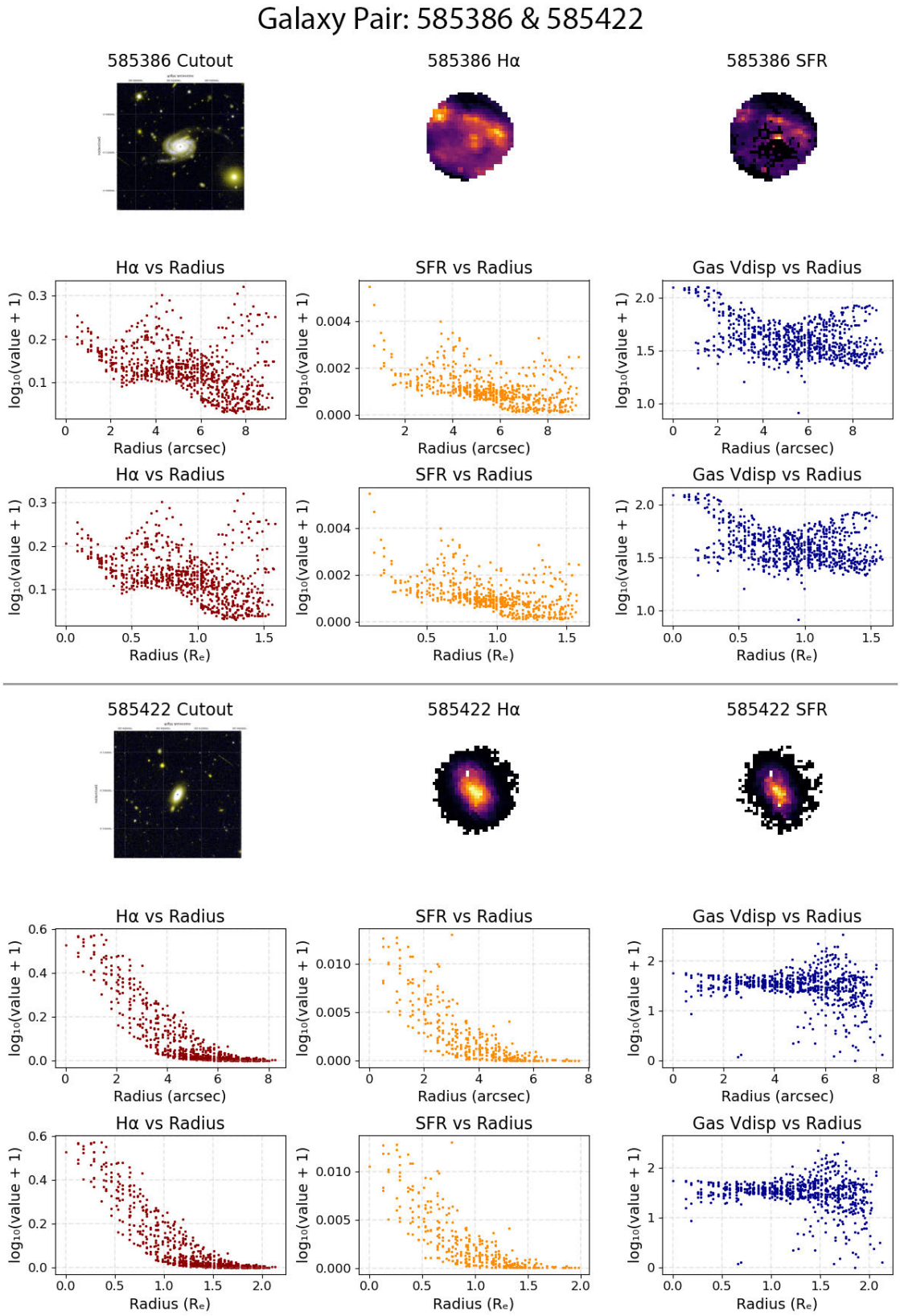

Figure 4.3: Multi-panel comparison of SAMI galaxy pair 585386 (top) and 585422 (bottom), showing KiDS imaging, Hα emission, SFR, and gas velocity dispersion (V_{disp}). Each row includes spatial maps and corresponding radial profiles, plotted in both arcseconds and units of R_e, highlighting structural and kinematic differences between the larger primary and its smaller companion. KiDS curouts were obtained via the DataCentral Image Cutout Service (de Jong et al. 2015; DataCentral 2025)

CHAPTER 5: RESULTS

Before examining the spatial distribution of SFR, I first compared the overall SF rates of interacting and isolated galaxies. Figure 5.1 illustrates the distribution of the total SFR per galaxy, expressed as $\log_{10}(\mathrm{SFR}/M_\odot\ \mathrm{yr}^{-1})$, henceforth all statistics quoted are in these units unless otherwise specified. As can be seen in the plot, merging galaxies exhibit systematically higher SFR values, with a mean of -0.975 ± 0.075 ($\sigma = 0.922$, $n = 601$), compared to -1.142 ± 0.075 ($\sigma = 0.869$, $n = 535$) for isolated galaxies, while the medians (-0.868 vs. -1.109) confirm this offset. Specific SFRs show a similar trend, with the mergers showing a mean of -10.417 ± 0.072 ($\sigma = 0.884$, $n = 601$) versus -10.534 ± 0.065 ($\sigma = 0.750$, $n = 535$) for isolated galaxies, with medians of -10.243 and -10.410 respectively.

These differences are statistically significant, with Kolmogorov-Smirnov (KS) tests yielding $D = 0.104$ ($p = 0.0038$) for SFR and $D = 0.135$ ($p = 5.5 \times 10^{-5}$) for sSFR, indicating that the distributions of mergers and isolated galaxies are unlikely to be drawn from the same parent population. Mann-Whitney U (MWU) tests corroborate this, with $U = 177{,}852$ ($p = 0.0020$) for SFR and $U = 181{,}598$ ($p = 1.6 \times 10^{-4}$) for sSFR. Together, these results demonstrate that mergers and isolated galaxies are statistically distinct populations, with mergers showing systematically elevated SF. The modest but statistically significant differences in both central tendency and overall distribution confirm that mergers drive enhanced SF, rather than representing random variation within the same parent population.

As this measure includes the full spatial extent of each galaxy, it reflects the overall global enhancement of mergers over isolated galaxies, but gives no clear indication of spatial SF distributions, which I explore later.

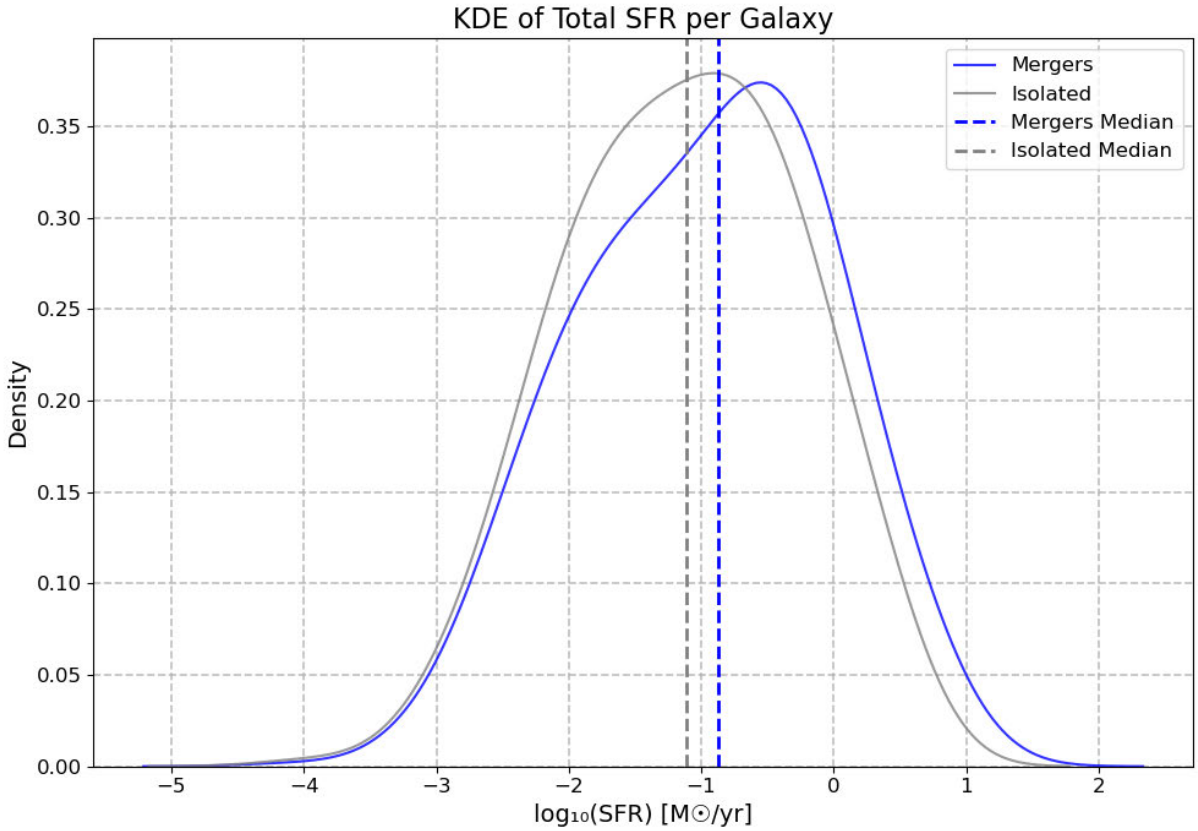

Figure 5.1: KDE of total SFR per galaxy for mergers (blue) and isolated (grey) galaxies. Vertical dashed lines indicate the median $\log_{10}$(SFR) values for each category. The merger population shows a modest shift toward higher SFRs, consistent with the statistical results discussed in Chapter 5

While global measures highlight overall enhancement, they obscure where within the galaxies this activity occurs. To address this, I constructed plots of SF as a function of radius. The SAMI data are provided in arcseconds, as shown in the radial plot in Figure 5.2(a). To compare galaxies of different sizes, I scaled the radial distance by each galaxy's R_e,and calculated the fractional radii (r/R_e). This size-independent approach allows direct comparison of star-forming profiles, and can be seen in Figure 5.2(b). Across $r \leq 3R_e$, Interacting galaxies show a higher mean $\log_{10}$(SFR) of -3.439 ± 0.073 ($\sigma = 0.882$, $n = 588$) compared to -3.598 ± 0.072 ($\sigma = 0.828$, $n = 532$) for isolated systems, with medians $\log_{10}$(SFR) $= -3.451$ and -3.631, respectively. The radial plots include 668 interacting and 638 isolated galaxies with valid effective radii, but only those with at least one positive SFR pixel within 3 R_e contribute to the global statistics. KS tests confirm that the two distributions differ ($D = 0.090$, $p = 0.020$), supported by MWU results ($U = 171{,}758$, $p = 0.0045$). The resulting profiles show elevated SFR across all fractional radii in interacting galaxies compared to the isolated systems, with enhancement most pronounced in the nuclear regions and declining steadily towards the outskirts. There is an elevated bump in the outskirts region of the Interacting galaxies, indicating a subset that have a higher occurrence of SF in the outer regions.

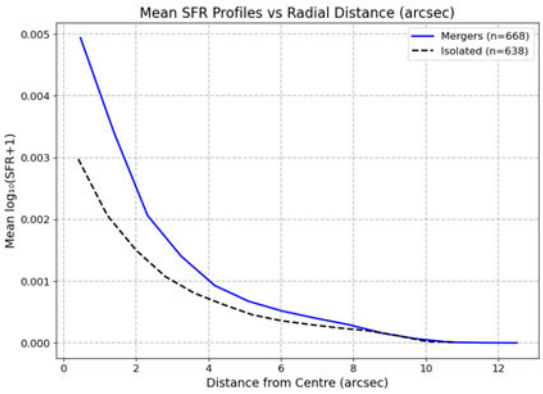

(a) Mean galaxy SFR profile vs radial distance (arcsec)

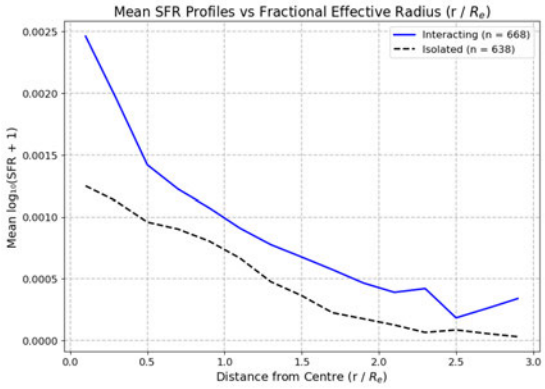

(b) Mean galaxy SFR profile vs fractional effective radius (r/R_e)

Figure 5.2: Mean SFR profiles vs radius for mergers and isolated galaxies, shown as a function of radial distance. Panel (a) plots log(SFR + 1) against physical radius in arcseconds, while panel (b) normalises distance by each galaxy's effective radius r/R_e. In both cases, mergers (solid blue) exhibit elevated central SFR compared to isolated galaxies (dashed black), consistent with merger-driven central enhancement.

To further investigate the factors that influence the spatial distribution of SF during galaxy mergers, once the SFR for each galaxy was normalised by its fractional R_e, I divided it into four fractional spatial regions:

- **Inner:** 0 - 0.5 R_e
- **Mid:** 0.5 - 1.0 R_e
- **Outer:** 1.0 - 2.0 R_e
- **Outer 2:** 2.0 - 3.0 R_e

Fractional effective radii normalisation ensures that central and outer regions are compared consistently. This removes the effect of distance to the galaxy, as galaxies further away appear smaller, and the effect of galaxy size. This segmentation allows direct comparison of star-forming activity across galaxies of varying sizes, highlighting both central and outer trends through radial distributions. By segmenting the galaxies in this way, further analysis can show whether mergers preferentially enhance nuclear SF or suppress activity in the outskirts.

In the following sections, I examine how stellar mass (Section 5.1), pair separation (Section 5.2), merger ratios (Section 5.3), morphology (Section 5.4), and combined mechanisms (Section 5.5) impact the radial distribution of SF, building on the global and radial trends established here.

5.1 Stellar Mass

When compared to isolated mass-matched galaxies, as shown in Figure 5.3, interacting systems follow the same overall trend of increasing SFR and declining sSFR with stellar mass. Higher-mass galaxies consistently exhibit elevated SFR, in line with the SFMS. In the SAMI sample, the innermost region (0 - 0.5 r/R_e) shows the steepest rise in SFR with increasing mass, reflecting the natural concentration

of stellar and gas reservoirs in galactic centres, and suggesting that central SF is more efficient in both isolated and merging systems. By contrast, the outer 2 region (2.0 - 3.0 R_e) shows significantly lower SFRs, indicating that star-forming activity in galaxy outskirts is comparatively suppressed.

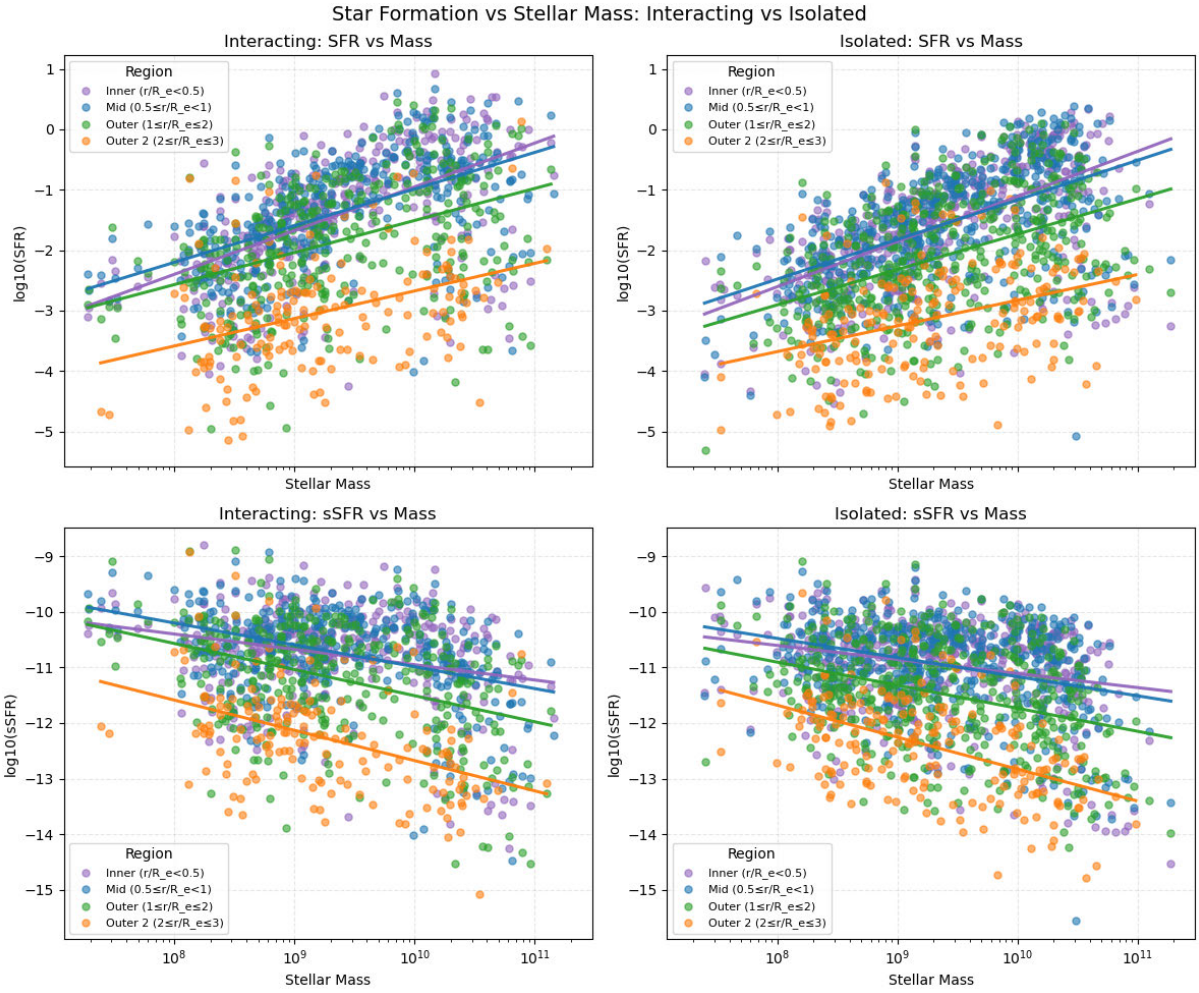

Figure 5.3: SFR and sSFR as a function of stellar mass for Isolated and Interacting galaxies. Each panel is colour-coded by radial region within galaxies: Inner ($r/R_e < 0.5$), Mid ($0.5 < r/R_e < 1.0$), Outer ($1.0 < r/R_e < 2.0$), and Outer 2 ($2.0 < r/R_e < 3.0$). Interacting galaxies show elevated SFR and sSFR across all regions, particularly in central zones, indicating merger-driven enhancement that scales with stellar mass.

The sSFR provides a complementary perspective: while SFR increases with mass, sSFR declines, reflecting the reduced relative efficiency of SF in more massive systems. This anti-correlation is particularly evident in the central regions, where the ratio of new SF to existing stellar mass declines steeply, highlighting the dominance of mass growth over ongoing SF.

To contextualise these trends, Figure 5.4 shows the distribution of SF across four annular regions for both mergers and isolated galaxies. In both environments, SF declines systematically with radius. The inner and mid regions exhibit very similar distributions with median $\log_{10}(\mathrm{SFR}) = -1.36$ and -1.39 for mergers and $\log_{10}(\mathrm{SFR}) = -1.49$ and -1.56 for isolated galaxies, respectively. The outer region shows a more pronounced drop, with medians of $\log_{10}(\mathrm{SFR}) = -1.94$ for mergers and $\log_{10}(\mathrm{SFR}) = -2.18$ for isolated, while the outermost annulus is the most diffuse, with medians of $\log_{10}(\mathrm{SFR}) = -3.04$ and -3.11. These results confirm that SF is centrally concentrated in both samples, but mergers

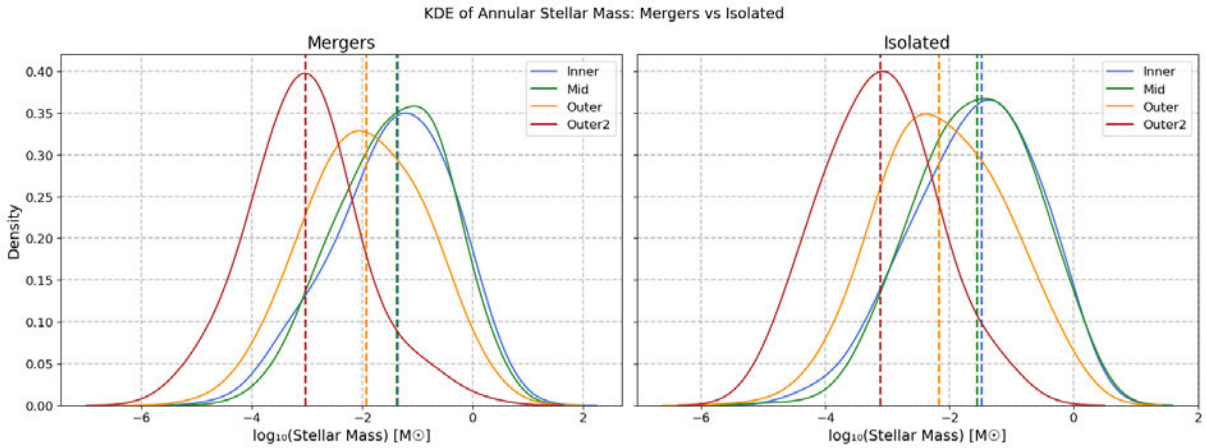

Figure 5.4: KDE of $\log_{10}$ stellar mass distributions across four annular regions for mergers (left) and isolated galaxies (right). Vertical dashed lines indicate median values.

consistently exhibit slightly higher activity at all radii compared to isolated systems.

The regression fits in Table 5.1 confirm the expected rise in SFR and sSFR with stellar mass across all regions. Complementary KS and MWU tests show that, with the exception of the inner vs mid comparison, where distributions are statistically indistinguishable ($p > 0.6$), all other radial regions differ significantly ($p < 0.001$). These results reinforce that interacting galaxies exhibit systematically elevated SF activity relative to isolated controls, particularly in the central and outermost zones.

Table 5.1: Regression fits of $\log_{10}$(SFR) and $\log_{10}$(sSFR) versus stellar mass across radial regions for interacting and isolated galaxies. Columns list: **Sample:** Interacting or Isolated subsample, **Metric:** logSFR or logSSFR, **Region:** r/R_e radial zone, **Slope:** per $\log_{10}$(M), **Intercept:** fit constant, **R:** correlation coefficient, p**-value:** significance of the fit, N**:** number of galaxies in the subsample.

Sample	Metric	Region (r/R_e)	Slope	Intercept	R	p-value	N
Interacting	logSFR	Inner (<0.5)	0.7245	-8.197	0.573	7.35×10^{-34}	372
Interacting	logSFR	Mid (0.5–1.0)	0.6071	-7.059	0.543	7.5×10^{-31}	384
Interacting	logSFR	Outer (1.0–2.0)	0.5308	-6.816	0.428	9.23×10^{-17}	344
Interacting	logSFR	Outer 2 (2.0–3.0)	0.4561	-7.236	0.372	1.1×10^{-6}	162
Isolated	logSFR	Inner (<0.5)	0.7474	-8.584	0.592	4.46×10^{-49}	505
Isolated	logSFR	Mid (0.5–1.0)	0.6560	-7.728	0.549	1.68×10^{-41}	511
Isolated	logSFR	Outer (1.0–2.0)	0.5858	-7.592	0.459	4.65×10^{-25}	454
Isolated	logSFR	Outer 2 (2.0–3.0)	0.4258	-7.087	0.364	2.35×10^{-7}	191
Interacting	logSSFR	Inner (<0.5)	-0.2755	-8.197	-0.257	5.06×10^{-7}	372
Interacting	logSSFR	Mid (0.5–1.0)	-0.3929	-7.059	-0.386	4.14×10^{-15}	384
Interacting	logSSFR	Outer (1.0–2.0)	-0.4692	-6.816	-0.386	1.1×10^{-13}	344
Interacting	logSSFR	Outer 2 (2.0–3.0)	-0.5439	-7.236	-0.431	1.03×10^{-8}	162
Isolated	logSSFR	Inner (<0.5)	-0.2526	-8.584	-0.241	4.18×10^{-8}	505
Isolated	logSSFR	Mid (0.5–1.0)	-0.3440	-7.728	-0.325	4.58×10^{-14}	511
Isolated	logSSFR	Outer (1.0–2.0)	-0.4142	-7.592	-0.343	5.27×10^{-14}	454
Isolated	logSSFR	Outer 2 (2.0–3.0)	-0.5742	-7.087	-0.466	1.14×10^{-11}	191

5.2 Pair Separation

Having established the role of stellar mass in shaping the radial distribution of SF, I next quantified the effect of pair separation. In this analysis, separation is defined as the projected distance between galaxy centres at the time of observation. Smaller separations correspond to stronger tidal interactions as gravitational forces scale with distance, but do not uniquely determine merger stage, as close pairs may represent either first passage or near coalescence. Within the constraints of the SAMI dataset and the scope of this study, separation is treated as a proxy for interaction strength. The following results examine how SFR and sSFR vary across radial regions as a function of pair separation, supported by statistical comparisons between separation bins.

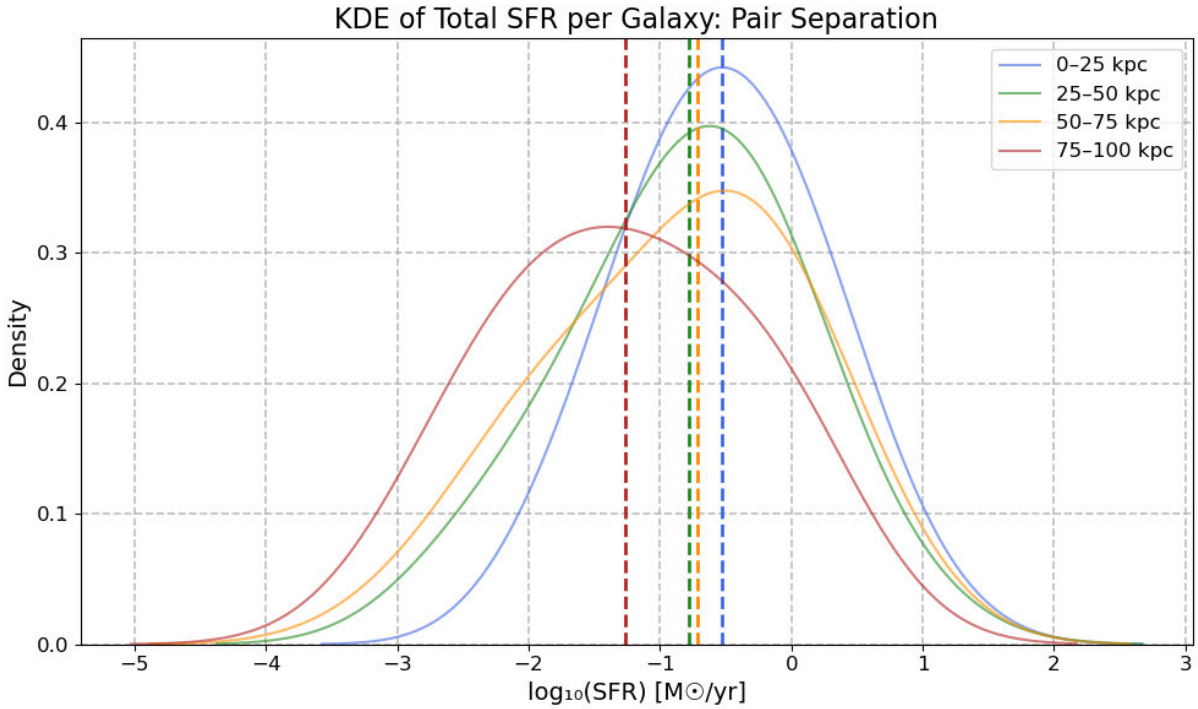

Figure 5.5: Distribution of total SFR per galaxy as a function of projected pair separation. The distribution highlights enhanced SFR at small separations (< 25 kpc) and a larger variability at larger separations (75 - 100 kpc).

The highest median in SFR occurred in the <25 kpc separation bin, which has a median of -0.524 (Figure 5.5). The median values decline with increasing separation, with $\log_{10}(\mathrm{SFR}) = -0.784$ at 25 - 50 kpc, -0.716 at 50 - 75 kpc, and -1.261 at 75 - 100 kpc. The largest separation, 75 - 100 kpc bin, also shows the broadest spread in SFR density, indicating that some galaxies at larger separations are undergoing starbursts. Some systems are still in pre-interaction phases with low activity, while others are mid-interaction and undergoing elevated SF, producing the observed diversity in this bin. Median sSFR values follow a similar trend, decreasing from $\log_{10}(\mathrm{sSFR}) = -9.844$ in the closest bin, stepping down to -10.220, -10.248, and -10.264 in successive bins. Statistical comparisons of the bins using KS and MWU tests reveal that the strongest difference is found between the sample of Pairs that are closest together (<25 kpc) and furthest apart (75 - 100 kpc): SFR ($p \approx 0.0004$ and $p \approx 0.00006$, and sSFR $p \approx 0.0045$ and $p \approx 0.0004$). Significant differences are also evident between the closest and

second-furthest bins, highlighting that proximity is a key modulator of sSFR.

Table 5.2: Regression fits of $\log_{10}$(SFR) and $\log_{10}$(sSFR) versus projected pair separation across radial regions for interacting galaxies. Columns list: **Metric:** logSFR or logSSFR being fitted; **Region (r/R_e):** radial zone of the galaxy; **Slope:** change in SFR/sSFR per unit pair separation; **Intercept:** baseline offset of the regression line; R**:** correlation strength; p**-value:** statistical significance of the fit; N**:** number of galaxies in the subsample.

Metric	Region (r/R_e)	Slope	Intercept	R	p-value	N
logSFR	Inner (<0.5)	-0.0103	-0.832	-0.295	1.9×10^{-4}	155
logSFR	Mid (0.5–1.0)	-0.0079	-0.900	-0.248	1.5×10^{-3}	160
logSFR	Outer (1.0–2.0)	-0.0062	-1.556	-0.169	4.2×10^{-2}	145
logSFR	Outer 2 (2.0–3.0)	-0.0081	-2.529	-0.286	3.3×10^{-2}	56
logSSFR	Inner (<0.5)	-0.0085	-10.24	-0.302	1.3×10^{-4}	155
logSSFR	Mid (0.5–1.0)	-0.0063	-10.34	-0.220	5.2×10^{-3}	160
logSSFR	Outer (1.0–2.0)	-0.0032	-11.06	-0.087	0.297	145
logSSFR	Outer 2 (2.0–3.0)	0.0001	-12.14	0.003	0.981	56

Figure 5.6 shows that SF declines with increasing pair separation across radial regions. In the central 0 - 0.5 r/R$_e$, both SFR and sSFR exhibit significant anti-correlations (SFR $R = -0.30$, $p < 0.001$; sSFR $R = -0.30$, $p =< 0.001$), confirming that central activity is most sensitive to separation of the galaxies. The mid annulus (0.5 - 1.0 r/R$_e$) also shows significant but weaker declines (SFR $R = -0.25$, $p \approx 0.002$; sSFR $R = -0.22$, $p \approx 0.005$). In the outer region (1.0 - 2.0 r/R$_e$), correlations are faint (SFR $R = -0.17$, $p \approx 0.04$; sSFR not significant). The outermost annulus (2.0 - 3.0 r/R$_e$) shows a modest decline in SFR ($R = -0.29$, $p \approx 0.03$) but no measurable trend in sSFR. Sample sizes range from 155 galaxies in the centre to 56 in the outskirts. These results confirm that the strongest separation-dependent modulation of SF occurs in the central regions, with progressively weaker correlations outward. Full regression statistics, including slopes, intercepts, R, p, and N, are provided in Table 5.2.

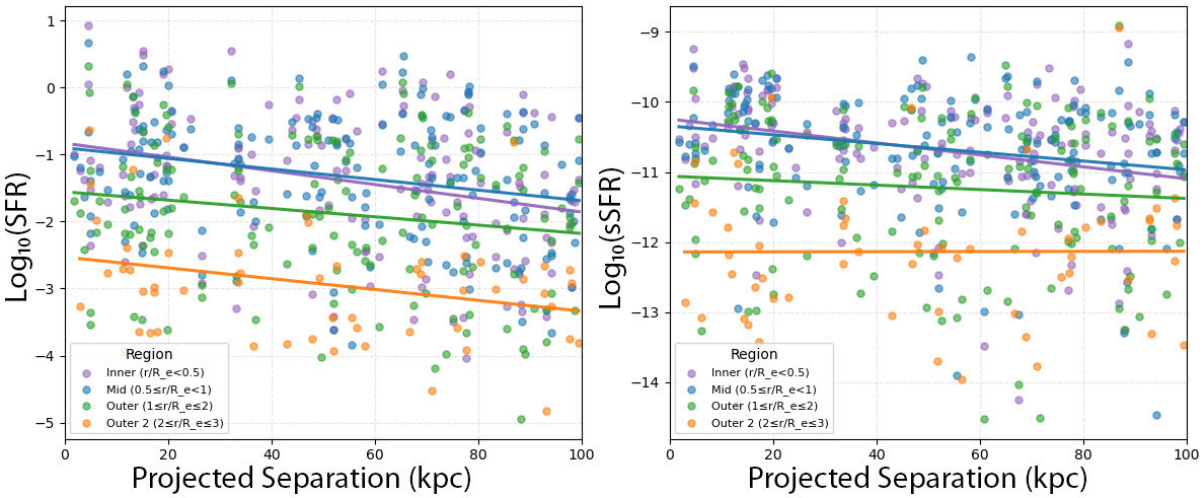

Figure 5.6: SFR and sSFR as a function of projected separation for interacting galaxy pairs. Each panel shows radial regions colour-coded by fractional effective radius: Inner ($r/R_e < 0.5$, purple), Mid ($0.5 < r/R_e < 1.0$, blue), Outer ($1.0 < r/R_e < 2.0$, green), and Outer 2 ($2.0 < r/R_e < 3.0$, orange). Both SFR and sSFR show declining trends with increasing separation, particularly in central regions, consistent with proximity-driven enhancement.

In summary, the pair separation analysis demonstrates that proximity is a strong modulator of SF, with the most significant declines in SFR and sSFR observed in the central regions and progressively weaker correlations outward (Table 5.2). Further discussion of these results can be found in Chapter 6.2.

5.3 Mass Ratio

To explore the influence of the comparative mass of the two interacting galaxies on SF, I calculated the mass ratio using the GAMA stellar mass catalogue (Taylor et al. 2011). As outlined in Chapter 4, I classified the galaxies into four categories based on mass ratio: **major merger** (1:1 - 1:4), **minor merger** (1:4 - 1:10), **dwarf merger** (1:10 - 1:100), and **satellite accretion** (> 1:100). Satellite accretion events were excluded from this analysis after quality control as only one system remained in the sample.

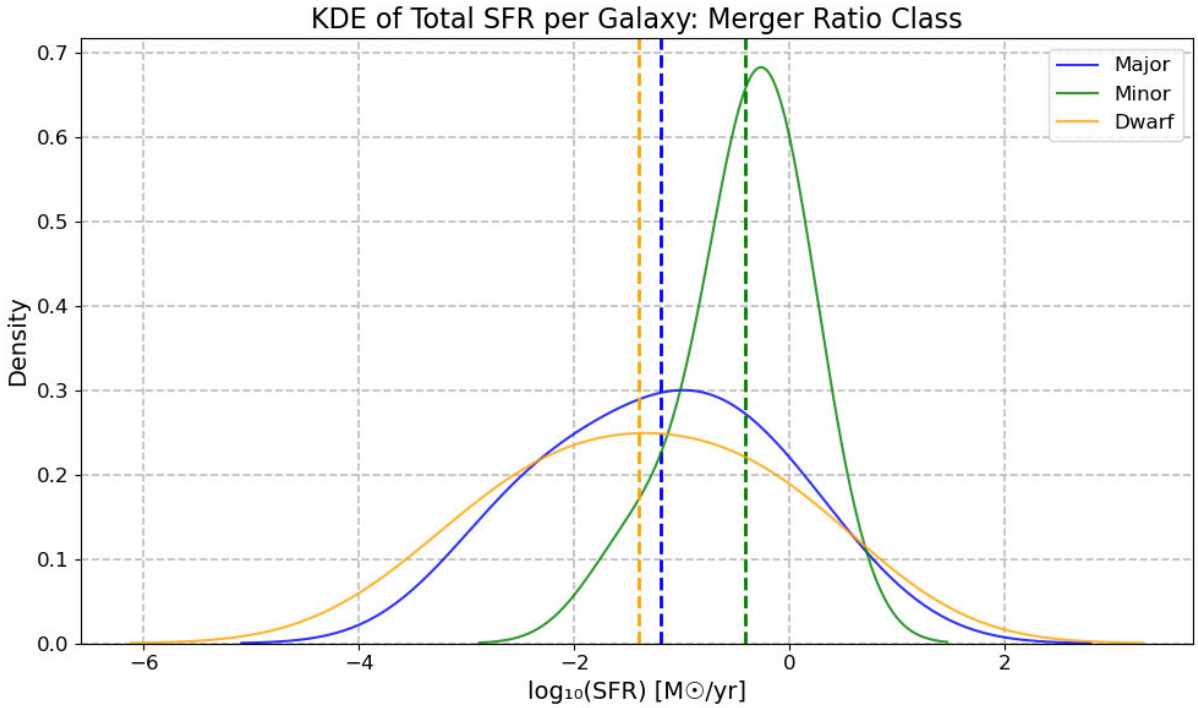

Figure 5.7: Kernel Density Plot (KDE) of total SFR per galaxy, grouped by merger ratio class: major (blue), minor (green), and dwarf (orange). Vertical dashed lines indicate the median $\log_{10}(\mathrm{SFR}\ [M_\odot\ \mathrm{yr}^{-1}])$ for each class. Minor mergers show a clear shift toward higher SFR values compared to major and dwarf systems, consistent with the statistical comparisons presented in Table 5.3.

Figure 5.7 shows that minor mergers have a median $\log_{10}(\mathrm{SFR}\ [\mathrm{M}_\odot\ \mathrm{yr}^{-1}])$ of -0.41, significantly higher than that of major and dwarf galaxies (-1.19 and -1.40 respectively). Elevated activity is also seen in sSFR, with statistical tests (Table 5.3) confirming that minor mergers are distinct from both other classes ($p < 0.01$). By contrast, major and dwarf mergers are not significantly different from each other in global SF.

Major and dwarf mergers have a broader distribution and larger standard deviation ($\sigma = 0.999$ and $\sigma = 1.144$ respectively) compared to minor mergers ($\sigma = 0.489$), indicating a greater variability in SFRs. Minor mergers appear both more elevated and more uniform in their behaviour.

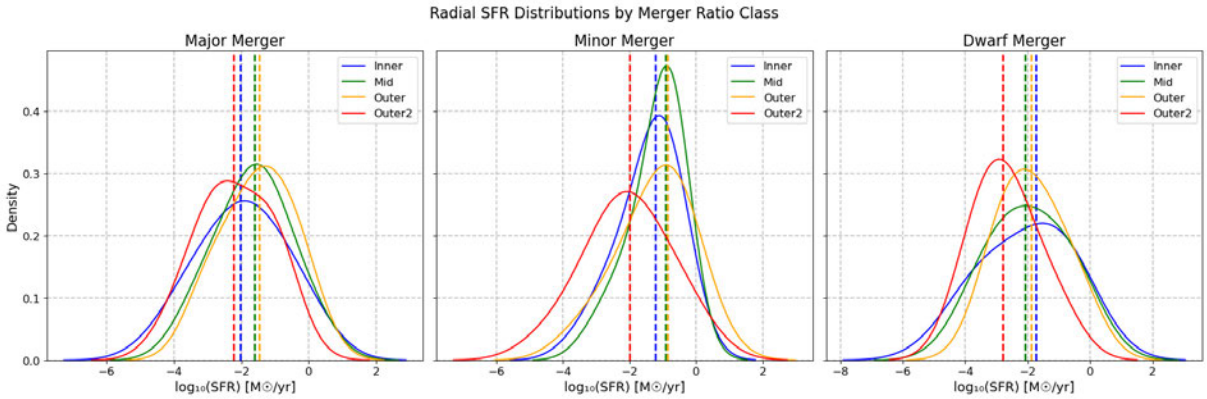

Figure 5.8: KDE estimates of radial SFR distributions for galaxies undergoing major, minor, and dwarf mergers. Each panel shows the $\log_{10}$(SFR) distributions across four radial zones: Inner (blue), Mid (green), Outer (orange), and Outer 2 (red). Major mergers peak in the mid and outer regions, minor mergers show elevated SFR across all annuli, and dwarf mergers concentrate activity in the nucleus. These trends reflect the influence of tidal redistribution and central suppression mechanisms across different merger scenarios.

Building on these global results, Figure 5.8 shows that median SFR values vary systematically with radius. Major mergers peak in the mid (-1.61) and outer (-1.47) regions, while minor mergers remain consistently higher across all annuli (-1.23, -0.93, -0.85, and -2.00). Dwarf mergers differ, with the highest median in the inner region (-1.75) and progressively lower values outward. Elevated SFR in the outer annuli likely reflects gas redistribution during tidal interactions, particularly in minor mergers where extended disks and tidal features sustain activity beyond the nucleus (Bottrell et al. 2024). Central suppression mechanisms such as rapid gas consumption or feedback may further enhance this contrast.

Taken together, Tables 5.3 and 5.4 quantify these trends. Minor mergers consistently show higher medians and smaller spreads in both $\log_{10}$(SFR) and $\log_10$(sSFR), while major and dwarf mergers exhibit lower medians and broader variability. These results highlight the distinctive role of minor mergers in driving enhanced and sustained SF compared to other merger classes.

Table 5.3: KS and MWU test results comparing $\log_{10}$(SFR) and $\log_{10}$(sSFR) distributions across merger ratio classes.

Metric	Class 1	Class 2	n_1	n_2	KS p-value	MWU p-value
logSFR	Major	Minor	34	13	0.0036	0.0069
logSFR	Major	Dwarf	34	19	0.9239	0.6495
logSFR	Major	Satellite	34	1	0.9714	0.9714
logSFR	Minor	Dwarf	13	19	0.0170	0.0420
logSFR	Minor	Satellite	13	1	0.4286	0.4286
logSFR	Dwarf	Satellite	19	1	0.9000	0.9000
logSSFR	Major	Minor	34	13	0.2181	0.1869
logSSFR	Major	Dwarf	34	19	0.0795	0.0462
logSSFR	Major	Satellite	34	1	0.0571	0.0571
logSSFR	Minor	Dwarf	13	19	0.0111	0.0021
logSSFR	Minor	Satellite	13	1	0.1429	0.1429
logSSFR	Dwarf	Satellite	19	1	0.1000	0.1000

Table 5.4: Summary statistics of $\log_{10}$(SFR) and $\log_{10}$(sSFR) by merger ratio class.

Class	N	Median logSFR	Mean logSFR	Std dev logSFR	Median logSSFR	Mean logSSFR	Std dev logSSFR
Major	34	-1.19	-1.19	0.999	-10.24	-10.43	0.821
Minor	13	-0.41	-0.41	0.489	-10.12	-10.05	0.537
Dwarf	19	-1.40	-1.36	1.144	-10.73	-11.01	1.064
Satellite	1	-1.05	-1.05	–	-9.19	-9.19	–

5.4 Morphology

To assess how morphology influences SF, I combined classifications from the GAMA (Kelvin et al. 2012) and SAMI Morphology Catalogues (Tuntipong et al. 2024). The GAMA catalogue grouped galaxies into several categories, collated into four primary classes. The SAMI catalogue focused on morphological classifications of merging systems and structural features such as bars or boxy-peanut bulges. I initially used the SAMI classification system to ensure galaxies marked in the Isolated group were not exhibiting signs of recent or ongoing merging. Both catalogues are described in more detail in Chapter 4.

5.4.1 *GAMA Categories*

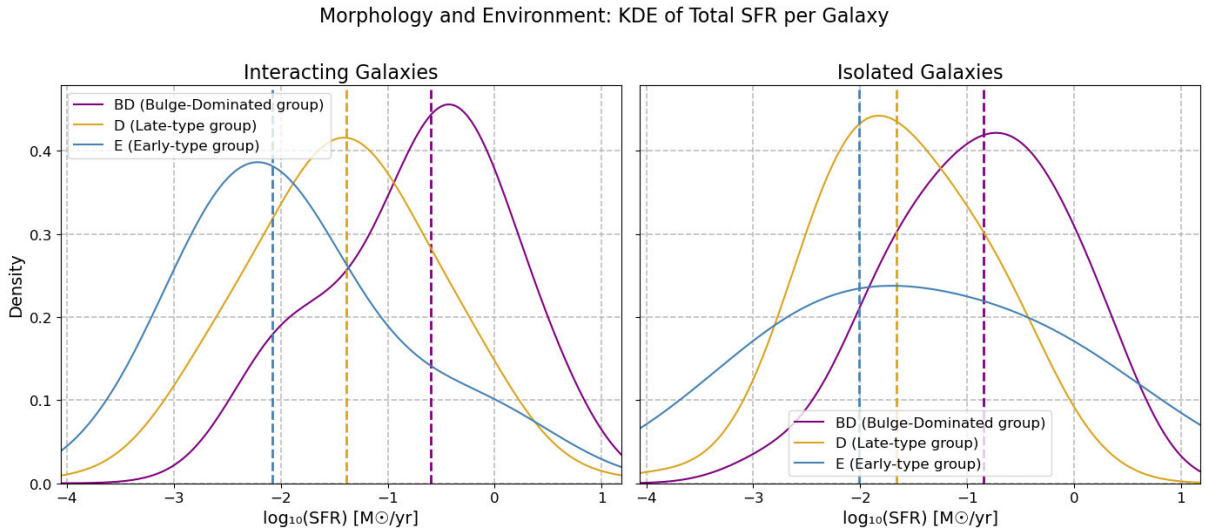

Figure 5.9: KDE of total SFR per galaxy, grouped by GAMA morphology class: Bulge-dominated (BD, purple), Late-type (D, yellow), and Early-type (E, blue) for interacting (left) and isolated (right) galaxies. Vertical dashed lines indicate the median of each distribution. Early-type galaxies show the lowest SFRs in both environments, consisted with quiescent spheroidal systems. Bulge-dominated galaxies exhibit broader distributions and higher medians, reflecting higher levels of ongoing SF.

Figure 5.9 compares the distribution of total SFR across the three GAMA morphology groups in interacting and isolated environments. Early-type galaxies exhibit the lowest SFRs, with distributions skewed toward quiescence and medians below $\log_{10}(\mathrm{SFR}) = -2$, consistent with spheroidal systems that have largely ceased SF. Late-type galaxies show intermediate SFR activity, with broader distributions and medians around -1.4, suggesting ongoing but reduced SF. Bulge-dominated galaxies display the highest median SFRs in both environments, peaking near $\log_{10}(\mathrm{SFR}) = -0.6$. In the interacting sample, their distribution is sharply peaked and slightly skewed, indicating a concentrated population of star-forming systems. This likely reflects the fact that many BD galaxies in the GAMA scheme are not purely spheroidal systems, but include barred spirals and disk galaxies with prominent bulges (Kelvin et al. 2012).

The comparison reveals that morphology strongly influences SF, but environment modulates the intensity. Interacting galaxies show more sharply defined distributions, particularly for BD systems, implying that interactions may reinforce structural triggers for SF. Isolated galaxies retain the same morphological hierarchy (BD > D > E), but with more diffuse distributions and lower overall SFRs. Bulge-dominated systems are consistently more active, even in isolation, while early-types remain quenched regardless of environment. Interactions appear to amplify existing structural tendencies rather than override them.

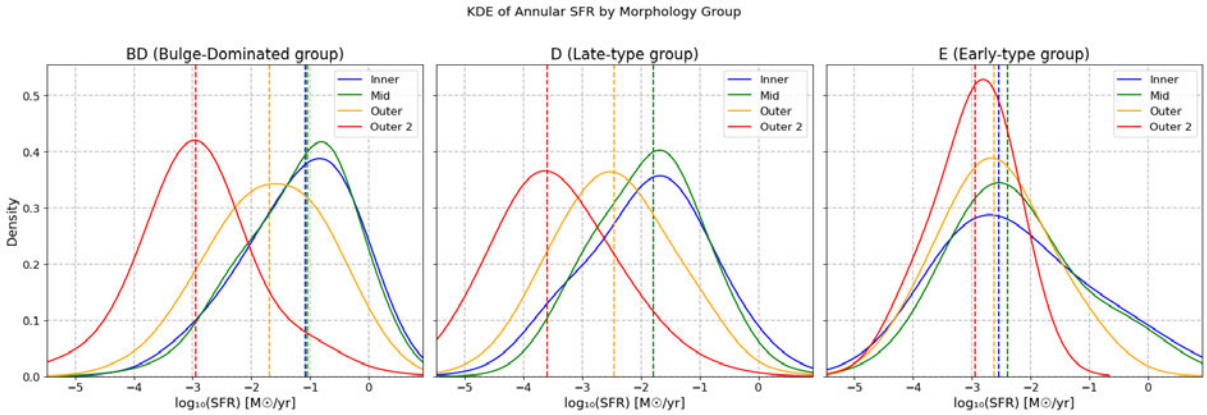

Figure 5.10: KDE of annular SFR distributions across four radial zones: Inner (blue), Mid (green), Outer (orange), and Outer 2 (red); for each GAMA morphology group: Bulge-dominated (BD), Late-type (D), and Early-type (E). Vertical dashed lines indicate median of each region's distribution. This figure includes only galaxies in the **merging** sample. The plots reveal how SF varies spatially within galaxies of different morphologies, highlighting distinct radial behaviours across structural types.

While global profiles provide an overarching picture of SF in merging systems compared to isolated systems, the purpose of this research was to consider the spatial distribution of SF in merging systems. Figure 5.10 presents annular SFR distributions across the four radial zones for each morphological group.

In bulge-dominated systems, SF is broadly distributed across all annuli, with elevated medians in the inner and mid regions ($\log_{10}(\mathrm{SFR}) \approx -1.08$ and -1.05 respectively). The outermost annulus shows a lower median SFR (-2.95), though still higher than those of late-type galaxies (-3.60). Across the inner three regions, BD galaxies consistently exceed both D and E groups in terms of SF. Late-type galaxies show nearly identical medians in the inner and mid regions (-1.79), producing a balanced profile across all zones. Their activity is less concentrated than BD galaxies, but more evenly distributed into the outskirts. Early-type galaxies display the most suppressed SF, with narrow distributions peaked at low median values (Inner: -2.54, Mid: -2.40, Outer: -2.62, and Outer 2: -2.94). The outer 2 region shows the highest SFR density, consistent with residual or stochastic SF in the outskirts of quenched systems. This radial pattern is consistent with the well-established phenomenon of *inside-out quenching*, in which SF is first suppressed in central regions before fading in the outskirts (Tacchella et al. 2015; Lin et al. 2019; Ellison et al. 2022). Such quenching is thought to result from rapid gas consumption, feedback from AGN or stellar winds, and the stabilisation of central disks, leaving only low-level or stochastic activity detectable at large radii.

Overall, though some bins are sparsely populated, these regional profiles further reinforce the conclusion that morphology governs not only the total SFR, but also its spatial distribution. Bulge-dominated galaxies maintain elevated SFRs across all zones, while late-types show more disk-dominated activity, and early-types remain largely passive. The presence or absence of structural features such as bars may further modulate these trends, as explored in the following section.

5.4.2 *Barred and unbarred galaxies*

Bars are elongated stellar structures that redistribute angular momentum and channel gas toward central regions of galaxies. They are common in disk galaxies, and can both trigger central SF and contribute to quenching, depending on gas availability and feedback processes (Saintonge et al. 2012; Fraser-McKelvie et al. 2021; Tuntipong et al. 2024).

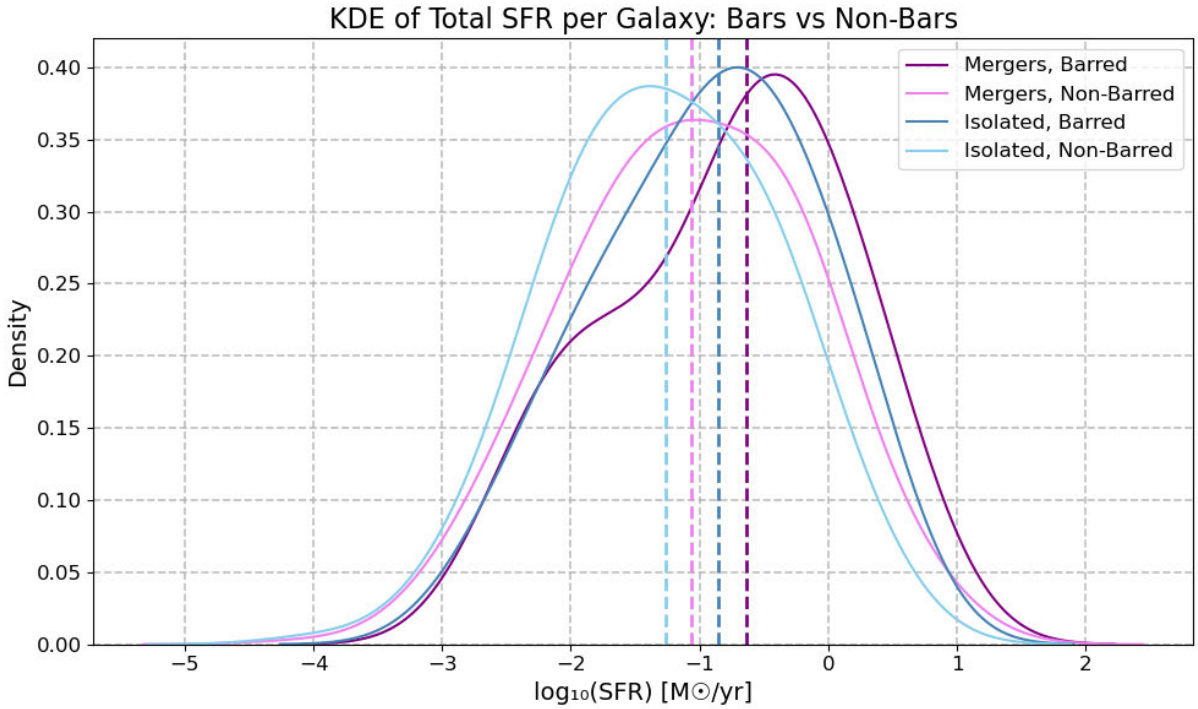

Figure 5.11: KDE of total SFR per galaxy for barred (purple) and unbarred (grey) systems, shown separately for merging (left) and isolated (right) samples. Vertical dashed lines mark the median of each distribution. Barred galaxies exhibit elevated SFRs in both environments, with the strongest enhancement seen in mergers.

Figure 5.11 compares the total SFRs of barred and non-barred galaxies across the merging and isolated systems. In both samples, barred systems exhibit elevated SFRs relative to their non-barred counterparts. The barred distribution for mergers peaks near $\log_{10}(\mathrm{SFR}) \approx -0.6$, while non-barred mergers show a broader, flatter profile with a median closer to -1.1. In isolated galaxies, the difference is more subtle. Isolated barred systems show a more modest enhancement in SFR compared to non-barred isolated galaxies, with medians near -0.9 and -1.3, respectively.

These results suggest that bars enhance gas inflow and trigger SF during interactions, amplifying the merger-driven activity. The slightly narrower and more symmetric curves of the isolated galaxies indicates less variation in SFRs among the isolated galaxies, implying that while bars can stimulate SF in isolation, their impact is less pronounced than in merging systems. Overall, the presence of a bar correlates with higher SFRs in both environments, but the effect is stronger in mergers. This supports the hypothesis that bars act as internal drivers of SF, and their influence is amplified when coupled with external perturbations (Saintonge et al. 2012; Fraser-McKelvie et al. 2021). The consistent offset between barred and non-barred distributions across environments highlights the structural role of bars in regulating galaxy evolution.

Breaking the barred and non-barred mergers down into annular SFR regions, Figure 5.12 shows that barred mergers exhibit elevated SF across the central regions, with the inner and mid zones showing particularly strong peaks compared to the outer regions. The inner region has a median $\log_{10}(\mathrm{SFR}) \approx -1.39$ compared to -1.32 for non-barred mergers, while the mid region shows a median of $\log_{10}(\mathrm{SFR}) \approx -1.44$ in barred and -1.33 in non-barred mergers. These values highlight the concentrated central activity in both cases, but with barred systems slightly more suppressed in the mid annulus, consistent with bar-driven inflows focusing gas towards the galaxy centre.

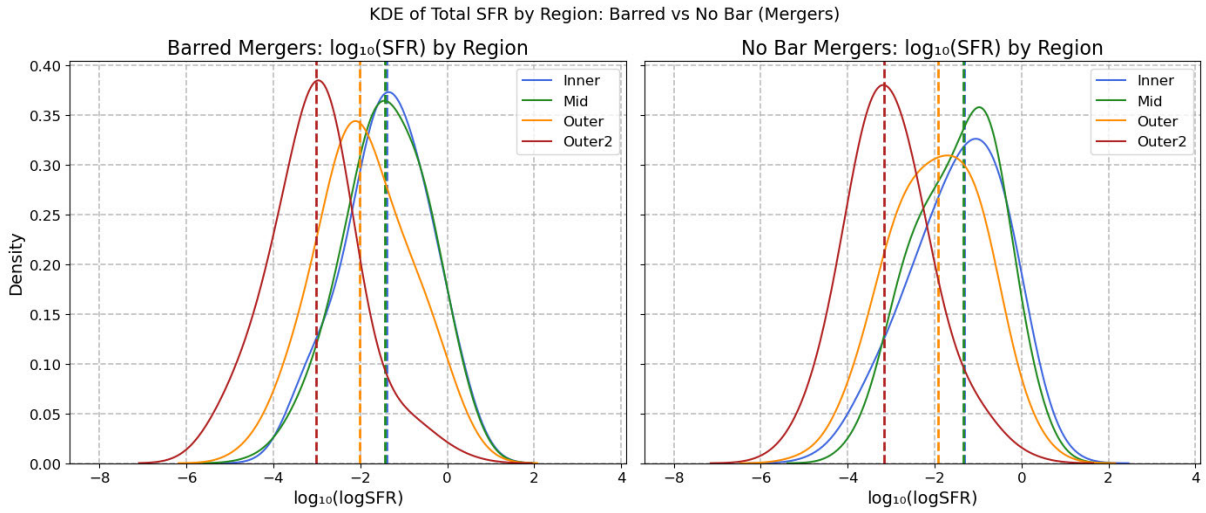

Figure 5.12: KDE of annular SFR distributions across four radial zones: Inner (blue), Mid (green), Outer (orange) and Outer 2 (red); for barred (solid) and non-barred (dashed) merging galaxies. Vertical dashed lines indicate median values. Barred mergers show enhanced central activity, consistent with bar-driven inflows.

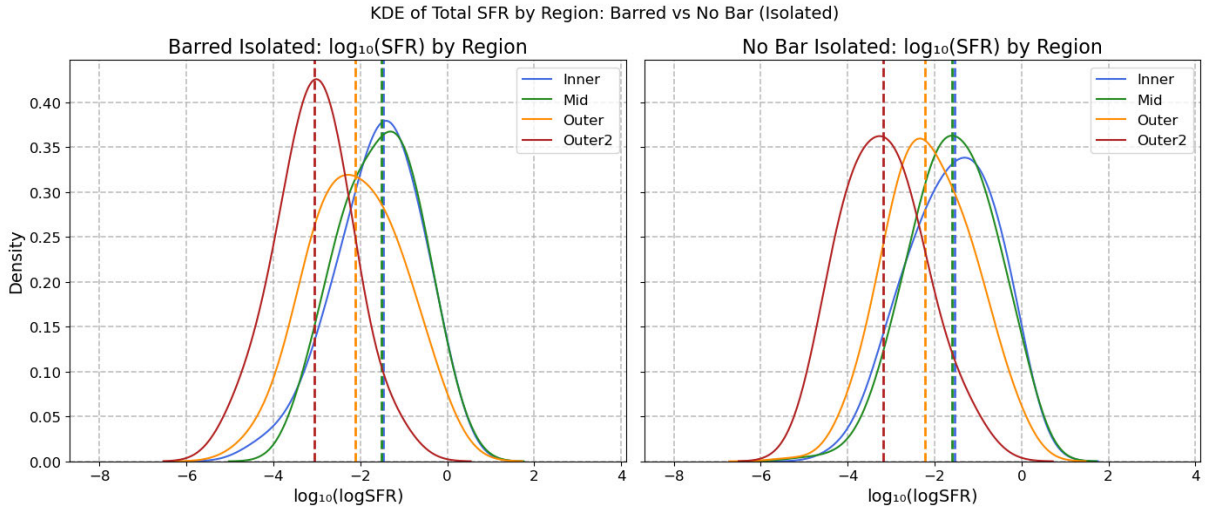

Figure 5.13: KDE of annular SFR distributions across four radial zones for barred (solid) and unbarred (dashed) isolated galaxies. Vertical dashed lines indicate median values. Bars modestly enhance central SF in isolation, but their impact is less pronounced than in mergers.

In the outer disk, barred mergers have a median of $\log_{10}(\mathrm{SFR}) \approx -2.02$ compared to -1.92 for non-barred systems, and the outer 2 annulus the medians converge at $\log_{10}(\mathrm{SFR}) \approx -3.01$ and -3.16

respectively. This pattern indicates that while bars help channel gas inward, they may reduce SF efficiency in the outskirts relative to non-barred mergers.

Although non-barred mergers show slightly higher median SFRs in most individual annuli, the global distribution reveals the opposite trend: barred mergers have a higher overall median ($\log_{10}(\mathrm{SFR}) \approx -0.6$ vs $\log_{10}(\mathrm{SFR}) \approx -0.9$). This apparent discrepancy arises because the global median reflects the integrated distribution across all regions, where central inflows in barred systems produce a sharper peak and reduce the prevalence of low-SFR galaxies. Thus, bars amplify the total star-forming response to mergers even if their annular medians appear lower in isolation.

5.5 Multi-Factor Effects

Literature suggests that SF in merging galaxies is not controlled by a single phenomenon, but instead arises from the interplay of multiple factors, including pair separation (Ellison et al. 2008; Scudder et al. 2012), mass ratio (Lambas et al. 2012), morphological structure (Saintonge et al. 2012; Fraser-McKelvie et al. 2021), gas inflows and feedback (Mihos and Hernquist 1996; Springel et al. 2005; Hopkins et al. 2013a), and environmental context (Schaefer et al. 2017; Oh et al. 2019).

While disentangling all potential factors and scenarios is outside the scope of this thesis, examining the combined influence of several key factors provides a minimal but useful framework for understanding how different mechanisms interact to shape SFR in mergers.

5.5.1 Interaction Morphology

Merging galaxies were classified based on the visually observed presence of interaction features, such as mergers (two systems that are very close to one another, almost a single system), interactions (galaxies that show signs of disturbance but are still individual galaxies), or shells/asymmetries (galaxies classified with shells or asymmetries, including merger remnants), using the SAMI Morphology Catalogue (Tuntipong et al. 2024). If a galaxy showed evidence of one or more interaction features, it was marked as "Any Interaction". Galaxies with no noted features were marked as "None". Individual plots were generated to highlight the regional differences of each merger category as separation between the pairs increased, as outlined in Figure 5.14.

Systems classified as showing no visual features exhibited a steady decline in SF across all regions as pair separation increased. This decline is most uniform in the inner three regions, while SF in the outermost annulus decreased at a far slower rate. In contrast, the sSFR displayed a marked increase in the outermost region. This reflects the low stellar mass in the outskirts, as discussed in **Section 5.2**, even modest SF produces a high specific rate when normalised by mass.

The mid region (0.5 - 1.0 r/R_e) hosts the highest overall SFR and sSFR in this sub-group. This contrasts with the mergers vs separation plot in Figure 5.6, where the innermost region dominated. The difference arises because galaxies without visible interaction features lack the tidal torques and gas inflows mergers generate, which are known to funnel material into the central kpc and ignite nuclear starbursts (e.g. Ellison et al. 2011; Sparre et al. 2022). In the absence of such inflows, star-forming gas remains distributed across the disk, with the mid-region acting as the most efficient site of SF.

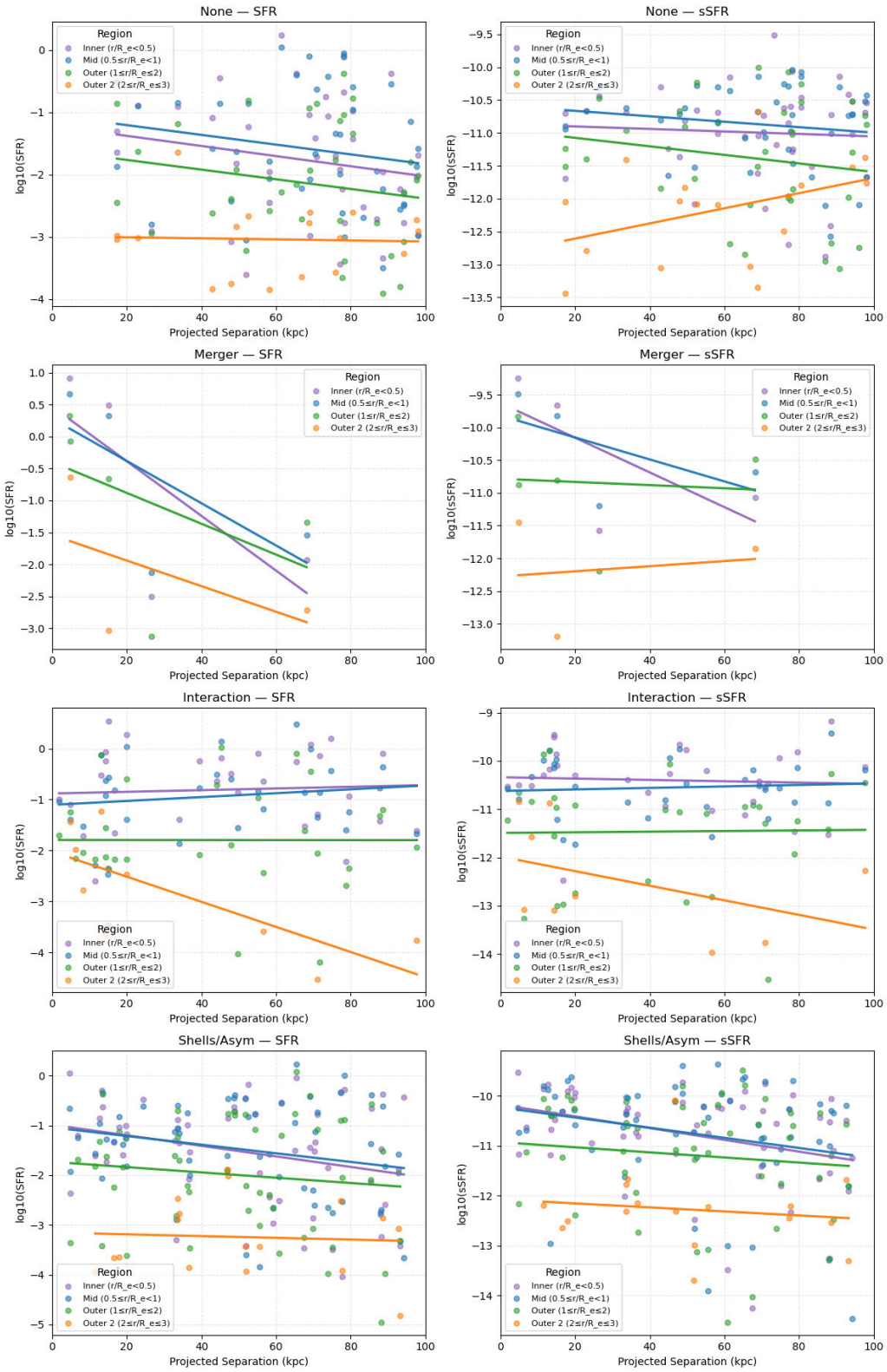

Figure 5.14: Scatter plots showing the relationship between projected pair separation and SF activity across four radial zones: Inner (purple), Mid (blue), Outer (green), and Outer 2 (orange); for galaxies classified by interaction morphology. Left column: $\log_{10}(\mathrm{SFR})$; right column: $\log_{10}(\mathrm{sSFR})$. Each row corresponds to a different interaction class: None, Merger, Interaction, and Shells/Asymmetries. Systems with no visible features show a steady decline in SFR with separation, while Mergers exhibit strong central suppression at larger distances. Interacting galaxies display rising central and mid-disk activity at close separations, with outer disk bursts preceding nuclear inflows. Shells and asymmetries show uniform decline across all regions, consistent with fading post-merger activity.

Galaxies classified as undergoing a merger show a pronounced decline in SF with increasing pair separation, but the rate of change is strongly region-dependent. The innermost zone exhibits the steepest drop, with both SFR and sSFR falling rapidly as distance grows. This behaviour reflects the physical role of mergers in driving gas inflows. At small separations, tidal torques funnel material into the central regions, producing elevated SF. As the galaxies move further apart, those inflows weaken, leaving the central reservoir depleted and causing a relative decline in activity. The parallel drop in sSFR highlights that central stellar mass is large, so once inflows subside, even modest reductions inSFR translate into a significant fall in specific SFRs. In contrast, the outer regions decline more gradually, consistent with residual SF persisting in the disk even as the merger-driven central burst fades. As with galaxies lacking visible interaction features, the merger class shows an increase in sSFR in the very outer regions. This reflects the combination of a slower decline in absolute SFR and the low stellar mass of the outer disk, which together amplify the specific rate when normalised by mass.

Interacting class galaxies show a distinctive pattern of both SFR and sSFR across regions as pair separation increases. In terms of SFR, both the inner and mid regions exhibit rising trends, suggesting that interactions after the first pass are more likely to stimulate SF in the central and mid-disk zones. The outer region remains relatively stable, while the outer 2 annulus shows a sharp incline as the pair draws closer together, indicating a burst of SF activity in the outermost disk as the galaxies move closer together. This pattern indicates that during the initial approach of interacting pairs, the outer disk experiences a transient burst of SF. As the systems move past one another and begin to separate, tidal forces redistribute gas inward, fuelling central activity while outer disk formation subsides. This sequence differs from the merger class, where inflows dominate the nuclear region from the outset.

The sSFR trend reveals a more nuanced picture. The innermost region shows a slight decline in sSFR, despite rising SFR. This reflects the fact that sSFR is normalised by the total stellar mass of the galaxy. The central regions contribute disproportionately to the overall mass budget, meaning increases in nuclear SF translate into smaller relative changes in sSFR compared to the outskirts. In contrast, the mid region shows a clear increase in sSFR, and the outer region again remains relatively unchanged, suggesting more efficient SF relative to mass in these zones. The outer 2 region again increases sharply at smaller separations, mirroring the SFR trend and highlighting that interactions compress gas inward while sustaining activity in the outskirts. As galaxies approach, modest SF in the low-mass outer disk translates into a spike in both SFR and sSFR, whereas the inner nuclear region shows a decline in sSFR because its larger stellar mass dilutes the specific rate.

Galaxies classified as exhibiting shells or asymmetries show SF behaviour that closely parallels the global mergers vs separation trend seen in Figure 5.6. Across all regions, both SFR and sSFR decline steadily as separation increases. The innermost region experiences the sharpest drop, though only marginally greater than the mid and outer zones. The outer annulus decreases more slowly, likely reflecting the persistence of structural features that help retain or redistribute gas in the outskirts. Notably, this is the only subgroup in which sSFR mirrors SFR almost exactly, suggesting that the relative efficiency of SF scales directly with the absolute rate in these systems. This alignment implies that shells and asymmetries do not significantly alter the balance between stellar mass and SF, but instead act as signatures of fading interaction-driven activity across the disk.

CHAPTER 6: DISCUSSION AND CONCLUSIONS

The comparison of global SFRs between interacting and isolated galaxies demonstrates a clear enhancement in mergers. Both total SFR and sSFR distributions are shifted upwards in interacting systems, with statistical tests confirming that these populations are unlikely to be drawn from the same parent distribution. This establishes mergers as a key driver of elevated SF activity, consistent with the broader literature on merger-induced starbursts (Villumsen 1982; Darg et al. 2010a; Moreno et al. 2015; Oh et al. 2019; Mesa et al. 2021).

The physical mechanisms underlying this enhancement are well understood. Gravitational torques during interactions funnel gas into the central regions, compressing it and triggering nuclear starbursts (Barnes and Hernquist 1991; Mihos and Hernquist 1996; Springel et al. 2005; Hopkins et al. 2013b; Kewley et al. 2006). At the same time, tidal forces redistribute gas across the disk, producing extended star-forming regions that contribute to elevated global SFRs (Schmidt et al. 2013; Moreno et al. 2015; Thorp et al. 2019; Moreno et al. 2021; Sparre et al. 2022). The radial analysis (Chapter 5) reinforces this picture: interacting galaxies show enhanced SF at all fractional radii, with the strongest activity in the nucleus, but also a bump in the outskirts. This suggests that while central inflows dominate the enhancement, a subset of systems experience significant SF in tidal arms or outer disks, where disturbed gas reservoirs remain available for collapse.

Together, these results highlight two complementary mechanisms; central inflows and compression, which drive nuclear starbursts, and tidal redistribution of gas, which sustains SF in outer regions. The balance between these processes likely depends on stellar mass, pair separation, mass ratio, and morphology, factors explored in the subsequent sections.

6.1 Stellar Mass

The results align with broad evidence for centrally concentrated stellar mass and inside-out growth in disk galaxies, where mass and old stellar populations are weighted towards the inner regions and profiles steepen at large radii (White and Rees 1978; Kennicutt 1998; Pérez et al. 2013; Tacchella et al. 2015). The near-identical inner and mid distributions between mergers and isolated systems suggest that typical interactions do not dramatically reshape stellar mass profiles within $\lesssim 3\ R_e$, consistent with the expectation that stellar mass is comparatively stable on merger timescales. Instead, mergers appear to produce modest enhancements in stellar mass across all annuli, reflecting accretion of companion material and the cumulative effect of triggered SF. This interpretation is consistent with

Medling et al. (2018), who, using SAMI data, demonstrated that central stellar mass surface density is a key predictor of quenching. Galaxies with elevated central densities show suppressed nuclear SF, while those on the SFMS retain centrally concentrated activity. Together, these findings reinforce the view that stellar mass regulates sSFR, with mergers acting as a catalyst that boosts activity across the disk without erasing the underlying inside-out growth signature.

The regression fits reinforce this interpretation. Both interacting and isolated galaxies show positive correlations between stellar mass and SFR, with the steepest slopes in the inner regions. This reflects the natural concentration of gas and stellar mass in galactic centres, where gravitational potential wells are deepest and sSFR is highest (Chien 2010; Bournaud 2011; Ellison et al. 2013; McElroy et al. 2022; Das et al. 2023). The declining slopes with the radius highlight the reduced capacity of outer disks to sustain SF, consistent with the lower gas densities and longer dynamical timescales at larger radii (Moreno et al. 2015; Thorp et al. 2019; Moreno et al. 2021; Sparre et al. 2022). The anti-correlation between stellar mass and sSFR further indicates that while massive galaxies form more stars in absolute terms, their relative efficiency declines, pointing to the increasing dominance of mass growth over ongoing SF in the high-mass regime.

Taken together, these results suggest that mergers amplify existing mass-dependent trends rather than fundamentally altering them. Central regions remain the primary sites of SF, but mergers provide a modest boost across the disk by redistributing gas and triggering additional SF. The similarity of stellar mass profiles between mergers and isolated systems underscores that the enhancement is primarily in SF activity, not in the underlying stellar mass distribution. This distinction is important: mergers elevate SFRs without erasing the inside-out growth signature, implying that the physical mechanisms at play are short-term gas inflows and tidal perturbations rather than wholesale restructuring of stellar mass.

6.2 Pair Separation

Pair separation provides a complementary lens through which to interpret the radial SF trends observed in this thesis. Defined as the projected distance between companions, separation captures the strength of tidal interactions, even though it does not uniquely define merger stage. Despite this limitation, the results demonstrate that proximity is a strong modulator of SF, with the most significant enhancements occurring at the smallest separations.

Galaxies in the closest pairs show the highest SFRs and efficiencies, while systems at wider separations exhibit progressively lower activity. The strongest declines are observed in nuclear regions, confirming that central SF is most sensitive to tidal proximity. Mid-disk regions also show measurable declines, though weaker, while the outer annuli display only faint or absent correlations. This radial gradient highlights that separation-dependent modulation is strongest in the centre and diminishes outward.

Physically, this pattern is consistent with gravitational torques funnelling gas inward as galaxies approach, compressing clouds and triggering nuclear starbursts (Barnes and Hernquist 1991; Hopkins et al. 2013b). Simulation studies further support this view, with Moreno et al. (2015) demonstrating that close pairs experience the strongest enhancements, particularly in their central regions, with or-

bital geometry further shaping the distribution of activity. At the same time, tidal forces redistribute gas into extended disks, sustaining modest SF efficiency in the outskirts even as absolute rates decline (Moreno et al. 2015, 2021; Sparre et al. 2022).

Additional processes modulate these trends. Shocks and turbulence generated during close interactions can destabilise star-forming regions, while ram-pressure stripping removes gas from the outer disk, suppressing efficiency. Observational studies confirm these mechanisms, with cluster mergers and pair samples showing turbulence, stripping and quenching (Schaefer et al. 2017; Oh et al. 2019; Thorp et al. 2019; Mesa et al. 2021). Simulation work likewise demonstrates that shocks, inflows, and turbulence destabilise star-forming regions and redistribute gas (Barnes and Hernquist 1991; Springel et al. 2005; Teyssier et al. 2010; Hopkins et al. 2013b; Moreno et al. 2015, 2021; Sparre et al. 2022).

This framework aligns with inside-out quenching models, where central suppression is linked to compaction and morphological transformation (Tacchella et al. 2015; Lin et al. 2019; Ellison et al. 2022). Mergers act as a catalyst in this process, driving gas inflows and promoting bulge growth, interactions accelerate central quenching while simultaneously redistributing gas into extended regions. In this way, proximity directly regulates the balance between central enhancement and peripheral quenching. Close pairs show strong nuclear starbursts, while wider pairs sustain modest efficiency in the outskirts.

The weak or absent sSFR correlations in the outer regions reflect the relative scaling with stellar mass. Although absolute SF declines with increasing separation, reduced stellar mass in the outskirts means efficiency per unit mass can remain steady. This interpretation is consistent with the SAMI evidence that nuclear SF is most sensitive to separation, while outer regions show weaker or absent correlations (Schaefer et al. 2017; Medling et al. 2018).

Taken together, these results demonstrate that proximity plays a key role in modulating SF. As galaxies approach, gravitational forces distort stellar and gas distributions, driving inflows of cold gas toward the centre and triggering nuclear starbursts. At the same time, shocks, turbulence, and stripping suppress activity in the outskirts, producing a dynamic interplay between central enhancement and peripheral quenching.

6.3 Mass Ratio

Having established how interaction strength, as traced by projected separation, influences SF activity, I next examined the role of mass ratio between merging galaxies. This complementary measure distinguishes whether interactions are balanced by major mergers, asymmetric minor mergers, or more extreme dwarf mergers and satellite accretions, and provides further insight into how the relative mass of companions shapes SF outcomes.

The results show that minor mergers drive the strongest global SF enhancements, with significantly elevated median SFR and sSFR compared to both major and dwarf systems. Statistical tests confirm that minor mergers form a distinct population, while major and dwarf mergers are not significantly different from one another. This pattern is consistent with previous work demonstrating that minor interactions can be particularly effective in triggering starbursts (Woods and Geller 2007; Lambas et al. 2012; Robotham et al. 2014; Bottrell et al. 2024). Physically, asymmetric encounters are thought

to destabilise gas disks more effectively than equal-mass mergers, funnelling material into star forming regions without fully disrupting the host structure. The lower gravitational balance allows tidal forces to redistribute gas while leaving the primary disk intact, sustaining widespread SF rather than concentrating activity solely in the nucleus.

Major mergers, by contrast, show broader distributions of SF, reflecting a mix of bursting and quenching outcomes. Simulations demonstrate that while equal-mass encounters can drive strong inflows, they can also rapidly consume or heat central gas, leading to suppression once feedback becomes dominant (Barnes and Hernquist 1991; Springel et al. 2005; Hopkins et al. 2013b). This explains the wider spread of SFR values observed in major mergers, with some systems undergoing intense nuclear starbursts and others already transitioning to quenching.

Dwarf mergers exhibit comparatively weak activity, with SF concentrated in the inner regions and declining rapidly at larger radii. This outcome reflects their limited gas reservoirs and shallow potential wells, which make them more susceptible to stripping and feedback. Simulations confirm that low-mass companions are easily disrupted, contributing stars but little sustained gas inflow to the primary galaxy (Villumsen 1982; Teyssier et al. 2010).

Radial profiles further reinforce these differences. Minor mergers sustain enhanced SF across both central and outer annuli, consistent with tidal redistribution of gas into extended disks and bridges (Schmidt et al. 2013; Moreno et al. 2021; Sparre et al. 2022). The persistence of outer SF is consistent with longer dynamical timescales at larger radii, allowing bursts to remain detectable in the statistical distributions even after central inflows decline. Major and dwarf mergers show comparatively weaker activity, with major showing stronger central peaks but weaker outskirts, while dwarf mergers are dominated by nuclear activity with little extended SF.

These results suggest that mass ratio is a key regulator of merger-driven SF. Minor mergers act as efficient catalysts, boosting activity across the disk, while major and dwarf mergers contribute only modestly due to their limited gas supply.

6.4 Morphology

Morphology is a fundamental regulator of SF, shaping both the total activity and its spatial distribution. To assess how morphology influences SF in this sample, I combined the SAMI (Tuntipong et al. 2024) and GAMA (Kelvin et al. 2012) Morphology Catalogues. The GAMA catalogue provides robust structural classifications derived from imaging and Sérsic profile fitting (Kelvin et al. 2012; Liske et al. 2015; Driver et al. 2016), grouping galaxies into several categories that were collated into four primary types, as outlined in Chapter 4. The SAMI catalogue extends this framework with spatially resolved classifications of merging systems, bars, and boxy-peanut bulges (Medling et al. 2018; Scott et al. 2018; Fraser-McKelvie et al. 2021), enabling direct links between morphology and kinematic signatures. I initially used the SAMI classification system to ensure galaxies marked in the Isolated group were not exhibiting signs of recent or ongoing merging, consistent with previous SAMI analyses of merger identification and bar structure (Schaefer et al. 2017; Zhou et al. 2017; Tuntipong et al. 2024).

6.4.1 GAMA Categories

Across the three GAMA morphology groups, early-type galaxies exhibit the lowest SFRs, supporting the literature that links spheroidal morphology to suppressed SF. This pattern is explained by inside-out quenching, where suppressing begins in the nucleus and extends outward as galaxies age (Tacchella et al. 2015) (also Ellison 2018 and Lin 2019). Residual activity in the outskirts is consistent with stochastic accretion or environmental processes such as stripping and turbulence (Schaefer et al. 2017; Oh et al. 2019), reinforcing the view that these galaxies are largely passive with only minor rejuvenation events.

Late-type galaxies show ongoing but reduced SF, reflecting the role of extended gas reservoirs in sustaining disk-wide activity. Their more balanced radial profiles are consistent with studies of spiral galaxies where SF is distributed across the disk rather than concentrated in the centre (Saintonge et al. 2012; Schmidt et al. 2013; Fraser-McKelvie et al. 2021; Sparre et al. 2022). Interactions perturb these disks, but without strong central mass concentrations, inflows remain modest and SF continues to be spread across larger radii (Schmidt et al. 2013; Sparre et al. 2022).

Bulge-dominated galaxies stand out as the most active, with elevated SF across multiple regions. This agrees with evidence that central mass concentration regulates efficiency and that bulges can sustain nuclear activity even as galaxies evolve (Tacchella et al. 2015; Medling et al. 2018). Interactions appear to amplify these structural tendencies, funnelling gas inward and reinforcing bulge-driven SF (Moreno et al. 2015, 2021). The deeper potential wells and shorter dynamical times in bulge-dominated systems make them particularly responsive to tidal torques, explaining their strong central activity.

6.4.2 Barred and Unbarred Galaxies

Bars provide an additional structural influence. The results show that barred galaxies are more active than their non-barred counterparts, particularly in mergers. This supports the view that bars act as internal drivers of inflow, channelling gas toward the centre and enhancing nuclear activity, consistent with SAMI and MaNGA studies linking bar structures to central SF (Medling et al. 2018; Scott et al. 2018; Fraser-McKelvie et al. 2021). At the same time, bars can suppress outer-disk SF by redistributing or depleting gas reservoirs, a trend observed in kinematic analyses of barred systems (Schaefer et al. 2017; Zhou et al. 2017; Tuntipong et al. 2024).

Regionally, barred mergers show enhanced central activity, consistent with bar-driven inflows focusing gas toward the nucleus (Medling et al. 2018; Scott et al. 2018). The mid-disk often appears relatively suppressed compared to non-barred systems, reflecting the redistribution of gas inward at the expense of intermediate radii (Schaefer et al. 2017; Zhou et al. 2017). In the outskirts, barred mergers show lower efficiency than non-barred systems, consistent with the depletion or stabilisation of outer reservoirs (Fraser-McKelvie et al. 2021; Tuntipong et al. 2024). Despite these regional variations, the global SF response is stronger in barred mergers, because concentrated central activity reduces the prevalence of low-SFR galaxies and elevates the overall distribution.

In isolated galaxies, bars produce only modest enhancements. Without external perturbations, bar inflows operate at a steady pace, raising central activity slightly but leaving outer reservoirs largely

intact. This weaker offset is consistent with studies showing that external tides strengthen bar-driven inflows and amplify their impact on SF (Ellison et al. 2011; Fraser-McKelvie et al. 2021).

These results demonstrate that morphology sets the baseline for SF, while interactions and internal structures such as bars modulate the distribution and efficiency. Bulges sustain central activity, disks support extended SF, and spheroids remain quenched. Bars act as inflow channels whose impact is magnified in mergers, redistributing gas inward and altering the balance between central and outer activity. These findings reinforce the view that structural features regulate SF outcomes, with physical explanations provided by both observational and simulation studies.

6.5 Multi-Factor Effects

Merger-driven SF is inherently multi-factorial. Pair separation modulates the strength of tidal inflows (Ellison et al. 2008; Scudder et al. 2012), mass ratio shapes whether activity is widespread or nuclear (Lambas et al. 2012), and morphology regulates both the baseline and response to external perturbations (Saintonge et al. 2012; Fraser-McKelvie et al. 2021). Gas inflows and feedback further determine whether bursts are sustained or quenched (Mihos and Hernquist 1996; Springel et al. 2005; Hopkins et al. 2013a), while environmental processes such as stripping and turbulence add additional complexity (Schaefer et al. 2017; Oh et al. 2019). The interplay of these mechanisms is more complex than the scope of this thesis, but the results presented here provide a foundation for disentangling their combined influence.

In summary, this thesis has demonstrated that galaxy interactions consistently elevate SF, with the strongest enhancements in nuclear regions, but measurable effects across extended disks. By disentangling the individual roles of stellar mass, pair separation, mass ratio, and morphology, I have shown that mergers amplify existing structural trends rather than erase them, producing a nuanced balance between central inflows and tidal redistribution. These results provide spatially resolved evidence that interactions are a key driver of galaxy growth and transformation, while also highlighting the importance of internal structures such as bulges and bars in modulating outcomes. Together, these findings reinforce the view that mergers are not uniform events, but complex processes whose impact depends on multiple, interlinked factors.

6.6 Future Work

Building on this foundation, future work will extend the radial analysis to larger and more diverse samples, particularly through the Hector survey, which offers broader wavelength coverage and higher spectral resolution. This will enable more precise measurements of kinematics and SF across environments, testing whether the trends identified here hold universally. Further refinement of merger stage classifications, integration of morphological substructures such as bars and bulges, and incorporation of multi-wavelength tracers will help disentangle the timing and drivers of starburst and quenching phases. These directions will advance toward a comprehensive picture of how galaxies assemble, transform, and quench through cosmic time.

REFERENCES

References cited throughout this thesis

J. T. Allen, S. M. Croom, I. S. Konstantopoulos, J. J. Bryant, R. Sharp, G. N. Cecil, L. M. R. Fogarty, C. Foster, A. W. Green, I.-T. Ho, M. S. Owers, A. L. Schaefer, N. Scott, A. E. Bauer, I. Baldry, L. A. Barnes, J. Bland-Hawthorn, J. V. Bloom, S. Brough, M. Colless, L. Cortese, W. J. Couch, M. J. Drinkwater, S. P. Driver, M. Goodwin, M. L. P. Gunawardhana, E. J. Hampton, A. M. Hopkins, L. J. Kewley, J. S. Lawrence, S. G. Leon-Saval, J. Liske, Á. R. López-Sánchez, N. P. F. Lorente, R. McElroy, A. M. Medling, J. Mould, P. Norberg, Q. A. Parker, C. Power, M. B. Pracy, S. N. Richards, A. S. G. Robotham, S. M. Sweet, E. N. Taylor, A. D. Thomas, C. Tonini, and C. J. Walcher. The SAMI Galaxy Survey: Early Data Release. , 446(2):1567–1583, January 2015. doi: 10.1093/mnras/stu2057.

Halton Arp. Atlas of Peculiar Galaxies. , 14:1, November 1966. doi: 10.1086/190147.

Astropy Collaboration, T. P. Robitaille, E. J. Tollerud, P. Greenfield, and et al. Astropy: A community python package for astronomy. *Astronomy Astrophysics*, 558:A33, 2013. doi: 10.1051/0004-6361/201322068.

Astropy Collaboration, A. M. Price-Whelan, B. M. Sipőcz, H. M. Günther, and et al. The astropy project: Building an open-science project and status of the v2.0 core package. *The Astronomical Journal*, 156(3):123, 2018. doi: 10.3847/1538-3881/aabc4f.

R. Bacon, G. Adam, A. Baranne, G. Courtes, D. Dubet, J. P. Dubois, E. Emsellem, P. Ferruit, Y. Georgelin, G. Monnet, E. Pecontal, A. Rousset, and F. Say. 3D Spectrography at High Spatial Resolution. I. Concept and Realization of the Integral Field Spectrograph TIGER. , 113:347, October 1995.

R. Bacon, Y. Copin, G. Monnet, Bryan W. Miller, J. R. Allington-Smith, M. Bureau, C. M. Carollo, Roger L. Davies, Eric Emsellem, Harald Kuntschner, Reynier F. Peletier, E. K. Verolme, and P. Tim de Zeeuw. The SAURON project - I. The panoramic integral-field spectrograph. , 326(1):23–35, September 2001. doi: 10.1046/j.1365-8711.2001.04612.x.

R. Bacon, M. Accardo, L. Adjali, H. Anwand, S. Bauer, I. Biswas, J. Blaizot, D. Boudon, S. Brau-Nogue, J. Brinchmann, P. Caillier, L. Capoani, C. M. Carollo, T. Contini, P. Couderc, E. Daguisé, S. Deiries, B. Delabre, S. Dreizler, J. Dubois, M. Dupieux, C. Dupuy, E. Emsellem, T. Fechner, A. Fleischmann, M. François, G. Gallou, T. Gharsa, A. Glindemann, D. Gojak, B. Guiderdoni, G. Hansali, T. Hahn, A. Jarno, A. Kelz, C. Koehler, J. Kosmalski, F. Laurent, M. Le Floch, S. J. Lilly, J.-L. Lizon, M. Loupias, A. Manescau, C. Monstein, H. Nicklas, J.-C. Olaya, L. Pares, L. Pasquini, A. Pécontal-Rousset, R. Pelló, C. Petit, E. Popow, R. Reiss, A. Remillieux, E. Renault, M. Roth, G. Rupprecht, D. Serre, J. Schaye, G. Soucail, M. Steinmetz, O. Streicher, R. Stuik, H. Valentin, J. Vernet, P. Weilbacher, L. Wisotzki, and N. Yerle. The MUSE second-generation VLT instrument. In Ian S. McLean, Suzanne K. Ramsay, and Hideki Takami, editors, *Ground-based and Airborne Instrumentation for Astronomy III*, volume 7735 of *Society of Photo-Optical Instrumentation Engineers (SPIE) Conference Series*, page 773508, July 2010. doi: 10.1117/12.856027.

Joshua E. Barnes and Lars E. Hernquist. Fueling Starburst Galaxies with Gas-rich Mergers. , 370: L65, April 1991. doi: 10.1086/185978.

Dalya Baron, Hagai Netzer, Dieter Lutz, Ric I. Davies, and J. Xavier Prochaska. Not So Windy After All: MUSE Disentangles AGN-driven Winds from Merger-induced Flows in Galaxies along the Starburst Sequence. , 968(1):23, June 2024. doi: 10.3847/1538-4357/ad39e9.

Jorge K. Barrera-Ballesteros, Sebastian Sanchez, Begoña Garcia-Lorenzo, and Jesus Falcon-Barroso. Central star formation and chemical enrichment in CALIFA interacting galaxies. In *IAU General Assembly*, volume 29, page 2245583, August 2015.

R. Scott Barrows, Julia M. Comerford, Nadia L. Zakamska, and Michael C. Cooper. Observational Constraints on Correlated Star Formation and Active Galactic Nuclei in Late-stage Galaxy Mergers. , 850(1):27, November 2017. doi: 10.3847/1538-4357/aa93de.

Joss Bland-Hawthorn. Game-changer for astronomical instrumentation, 2016. URL https://www.sydney.edu.au/news-opinion/news/2016/07/19/game-changer-for-astronomical-instrumentation.html.

Joss Bland-Hawthorn, Julia Bryant, Gordon Robertson, Peter Gillingham, John O'Byrne, Gerald Cecil, Roger Haynes, Scott Croom, Simon Ellis, Martin Maack, Peter Skovgaard, and Danny Noordegraaf. Hexabundles: imaging fiber arrays for low-light astronomical applications. *Optics Express*, 19(3):2649, January 2011. doi: 10.1364/OE.19.002649.

Connor Bottrell, Hassen M. Yesuf, Gergö Popping, Kiyoaki Christopher Omori, Shenli Tang, Xuheng Ding, Annalisa Pillepich, Dylan Nelson, Lukas Eisert, Hua Gao, Andy D. Goulding, Boris S. Kalita, Wentao Luo, Jenny E. Greene, Jingjing Shi, and John D. Silverman. IllustrisTNG in the HSC-SSP: image data release and the major role of mini mergers as drivers of asymmetry and star formation. , 527(3):6506–6539, January 2024. doi: 10.1093/mnras/stad2971.

F. Bournaud. Star formation in galaxy interactions and mergers. In Corinne Charbonnel and Thierry Montmerle, editors, *EAS Publications Series*, volume 51 of *EAS Publications Series*, pages 107–131, November 2011. doi: 10.1051/eas/1151008.

Sarah Brough, Jesse van de Sande, Matt S. Owers, Francesco d'Eugenio, Rob Sharp, Luca Cortese, Nicholas Scott, Scott M. Croom, Rob Bassett, Kenji Bekki, Joss Bland-Hawthorn, Julia J. Bryant, Roger Davies, Michael J. Drinkwater, Simon P. Driver, Caroline Foster, Gregory Goldstein, Á. R. López-Sánchez, Anne M. Medling, Sarah M. Sweet, Dan S. Taranu, Chiara Tonini, Sukyoung K. Yi, Michael Goodwin, J. S. Lawrence, and Samuel N. Richards. The SAMI Galaxy Survey: Mass as the Driver of the Kinematic Morphology-Density Relation in Clusters. , 844(1):59, July 2017. doi: 10.3847/1538-4357/aa7a11.

J. J. Bryant, M. S. Owers, A. S. G. Robotham, S. M. Croom, S. P. Driver, M. J. Drinkwater, N. P. F. Lorente, L. Cortese, N. Scott, M. Colless, A. Schaefer, E. N. Taylor, I. S. Konstantopoulos, J. T. Allen, I. Baldry, L. Barnes, A. E. Bauer, J. Bland-Hawthorn, J. V. Bloom, A. M. Brooks, S. Brough, G. Cecil, W. Couch, D. Croton, R. Davies, S. Ellis, L. M. R. Fogarty, C. Foster, K. Glazebrook, M. Goodwin, A. Green, M. L. Gunawardhana, E. Hampton, I.-T. Ho, A. M. Hopkins, L. Kewley, J. S. Lawrence, S. G. Leon-Saval, S. Leslie, R. McElroy, G. Lewis, J. Liske, Á. R. López-Sánchez, S. Mahajan, A. M. Medling, N. Metcalfe, M. Meyer, J. Mould, D. Obreschkow, S. O'Toole, M. Pracy, S. N. Richards, T. Shanks, R. Sharp, S. M. Sweet, A. D. Thomas, C. Tonini, and C. J. Walcher. The SAMI Galaxy Survey: instrument specification and target selection. , 447(3):2857–2879, March 2015. doi: 10.1093/mnras/stu2635.

Julia J. Bryant, Joss Bland-Hawthorn, Jon Lawrence, Scott Croom, Lisa M. Fogarty, Michael Goodwin, Samuel Richards, Tony Farrell, Stan Miziarski, Ron Heald, Heath Jones, Steve Lee, Matthew Colless, Michael Birchall, Andrew M. Hopkins, Sarah Brough, and Amanda E. Bauer. SAMI: a new multi-object IFS for the Anglo-Australian Telescope. In Ian S. McLean, Suzanne K. Ramsay, and Hideki Takami, editors, *Ground-based and Airborne Instrumentation for Astronomy IV*, volume 8446 of *Society of Photo-Optical Instrumentation Engineers (SPIE) Conference Series*, page 84460X, September 2012. doi: 10.1117/12.925115.

Julia J. Bryant, Joss Bland-Hawthorn, Jon Lawrence, Barnaby Norris, Seong-Sik Min, Rebecca Brown, Adeline Wang, Gurashish Singh Bhatia, Will Saunders, Robert Content, Ross Zhelem, Sudharshan Venkatesan, Mahesh Mohanan, Peter Gillingham, Robert Patterson, David Robertson, Naveen Pai, Helen McGregor, Jessica Zheng, Sam Vaughan, Caroline Foster, Sergio Leon-Saval, and Scott Croom. Hector: a new multi-object integral field spectrograph instrument for the Anglo-Australian Telescope. In Christopher J. Evans, Julia J. Bryant, and Kentaro Motohara, editors, *Ground-based and Airborne Instrumentation for Astronomy VIII*, volume 11447 of *Society of Photo-Optical Instrumentation Engineers (SPIE) Conference Series*, page 1144715, December 2020. doi: 10.1117/12.2560309.

Julia J. Bryant, Sree Oh, Madusha Gunawardhana, Gabriella Quattropani, Gurashish Singh Bhatia, Joss Bland-Hawthorn, David Broderick, Rebecca Brown, Robert Content, Scott Croom, Fred Crous, Tony Farrell, Peter Gillingham, Ellen Houston, Jon Lawrence, Helen McGregor, Seong-Sik Minh, Mahesh Mohanan, Barnaby Norris, Matthew Owers, Naveen Pai, David Robertson, Will Saunders, Sam Vaughan, Sudharshan Venkatesan, Adeline Wang, Ross Zhelem, and Jessica Zheng. Hector: performance of the new integral field spectrograph instrument for the Anglo-Australian Telescope. In Julia J. Bryant, Kentaro Motohara, and Joël. R. D. Vernet, editors, *Ground-based and Airborne Instrumentation for Astronomy X*, volume 13096 of *Society of Photo-Optical Instrumentation Engineers (SPIE) Conference Series*, page 130960D, July 2024. doi: 10.1117/12.3016340.

Kevin Bundy, Matthew A. Bershady, David R. Law, Renbin Yan, Niv Drory, Nicholas MacDonald, David A. Wake, Brian Cherinka, José R. Sánchez-Gallego, Anne-Marie Weijmans, Daniel Thomas, Christy Tremonti, Karen Masters, Lodovico Coccato, Aleksandar M. Diamond-Stanic, Alfonso Aragón-Salamanca, Vladimir Avila-Reese, Carles Badenes, Jésus Falcón-Barroso, Francesco Belfiore, Dmitry Bizyaev, Guillermo A. Blanc, Joss Bland-Hawthorn, Michael R. Blanton, Joel R. Brownstein, Nell Byler, Michele Cappellari, Charlie Conroy, Aaron A. Dutton, Eric Emsellem, James Etherington, Peter M. Frinchaboy, Hai Fu, James E. Gunn, Paul Harding, Evelyn J. Johnston, Guinevere Kauffmann, Karen Kinemuchi, Mark A. Klaene, Johan H. Knapen, Alexie Leauthaud, Cheng Li, Lihwai Lin, Roberto Maiolino, Viktor Malanushenko, Elena Malanushenko, Shude Mao, Claudia Maraston, Richard M. McDermid, Michael R. Merrifield, Robert C. Nichol, Daniel Oravetz, Kaike Pan, John K. Parejko, Sebastian F. Sanchez, David Schlegel, Audrey Simmons, Oliver Steele, Matthias Steinmetz, Karun Thanjavur, Benjamin A. Thompson, Jeremy L. Tinker, Remco C. E. van den Bosch, Kyle B. Westfall, David Wilkinson, Shelley Wright, Ting Xiao, and Kai Zhang. Overview of the SDSS-IV MaNGA Survey: Mapping nearby Galaxies at Apache Point Observatory. , 798(1): 7, January 2015. doi: 10.1088/0004-637X/798/1/7.

M. Bureau, M. Cappellari, Y. Copin, E. K. Verolme, P. T. de Zeeuw, R. Bacon, E. Emsellem, R. L. Davies, H. Kuntschner, R. McDermid, B. W. Miller, and R. F. Peletier. SAURON: An Innovative Look at Early-Type Galaxies. In G. S. Da Costa, E. M. Sadler, and Helmut Jerjen, editors, *The Dynamics, Structure & History of Galaxies: A Workshop in Honour of Professor Ken Freeman*, volume 273 of *Astronomical Society of the Pacific Conference Series*, page 53, January 2002. doi: 10.48550/arXiv.astro-ph/0109409.

L. Chien. Star Formation History in Merging Galaxies. In B. Smith, J. Higdon, S. Higdon, and N. Bastian, editors, *Galaxy Wars: Stellar Populations and Star Formation in Interacting Galaxies*, volume 423 of *Astronomical Society of the Pacific Conference Series*, page 197, June 2010.

Scott M. Croom, Jon S. Lawrence, Joss Bland-Hawthorn, Julia J. Bryant, Lisa Fogarty, Samuel Richards, Michael Goodwin, Tony Farrell, Stan Miziarski, Ron Heald, D. Heath Jones, Steve Lee, Matthew Colless, Sarah Brough, Andrew M. Hopkins, Amanda E. Bauer, Michael N. Birchall, Simon Ellis, Anthony Horton, Sergio Leon-Saval, Geraint Lewis, Á. R. López-Sánchez, Seong-Sik Min, Christopher Trinh, and Holly Trowland. The Sydney-AAO Multi-object Integral field spectrograph. , 421(1):872–893, March 2012. doi: 10.1111/j.1365-2966.2011.20365.x.

Scott M. Croom, Matt S. Owers, Nicholas Scott, Henry Poetrodjojo, Brent Groves, Jesse van de Sande, Tania M. Barone, Luca Cortese, Francesco D'Eugenio, Joss Bland-Hawthorn, Julia Bryant, Sree Oh, Sarah Brough, James Agostino, Sarah Casura, Barbara Catinella, Matthew Colless, Gerald Cecil, Roger L. Davies, Michael J. Drinkwater, Simon P. Driver, Ignacio Ferreras, Caroline Foster, Amelia Fraser-McKelvie, Jon Lawrence, Sarah K. Leslie, Jochen Liske, Ángel R. López-Sánchez, Nuria P. F. Lorente, Rebecca McElroy, Anne M. Medling, Danail Obreschkow, Samuel N. Richards, Rob Sharp, Sarah M. Sweet, Dan S. Taranu, Edward N. Taylor, Edoardo Tescari, Adam D. Thomas, James Tocknell, and Sam P. Vaughan. The SAMI Galaxy Survey: the third and final data release. , 505(1):991–1016, July 2021. doi: 10.1093/mnras/stab229.

D. W. Darg, S. Kaviraj, C. J. Lintott, K. Schawinski, M. Sarzi, S. Bamford, J. Silk, D. Andreescu, P. Murray, R. C. Nichol, M. J. Raddick, A. Slosar, A. S. Szalay, D. Thomas, and J. Vandenberg. Galaxy Zoo: the properties of merging galaxies in the nearby Universe - local environments, colours, masses, star formation rates and AGN activity. , 401(3):1552–1563, January 2010a. doi: 10.1111/j.1365-2966.2009.15786.x.

D. W. Darg, S. Kaviraj, C. J. Lintott, K. Schawinski, M. Sarzi, S. Bamford, J. Silk, R. Proctor, D. Andreescu, P. Murray, R. C. Nichol, M. J. Raddick, A. Slosar, A. S. Szalay, D. Thomas, and J. Vandenberg. Galaxy Zoo: the fraction of merging galaxies in the SDSS and their morphologies. , 401(2): 1043–1056, January 2010b. doi: 10.1111/j.1365-2966.2009.15686.x.

Apashanka Das, Biswajit Pandey, and Suman Sarkar. Do Minor Interactions Trigger Star Formation in Galaxy Pairs? *Research in Astronomy and Astrophysics*, 23(9):095026, September 2023. doi: 10.1088/1674-4527/aceccb.

Astralis DataCentral. Datacentral image cutout service. https://datacentral.org.au/services/cutout/, 2025.

Jelte T. A. de Jong, Gijs A. Verdoes Kleijn, Danny R. Boxhoorn, Hugo Buddelmeijer, Massimo Capaccioli, Fedor Getman, Aniello Grado, Ewout Helmich, Zhuoyi Huang, Nancy Irisarri, Konrad Kuijken, Francesco La Barbera, John P. McFarland, Nicola R. Napolitano, Mario Radovich, Gert Sikkema, Edwin A. Valentijn, Kor G. Begeman, Massimo Brescia, Stefano Cavuoti, Ami Choi, Oliver-Mark Cordes, Giovanni Covone, Massimo Dall'Ora, Hendrik Hildebrandt, Giuseppe Longo, Reiko Nakajima, Maurizio Paolillo, Emanuella Puddu, Agatino Rifatto, Crescenzo Tortora, Edo van Uitert, Axel Buddendiek, Joachim Harnois-Déraps, Thomas Erben, Martin B. Eriksen, Catherine Heymans, Henk Hoekstra, Benjamin Joachimi, Thomas D. Kitching, Dominik Klaes, Léon V. E. Koopmans, Fabian Köhlinger, Nivya Roy, Cristóbal Sifón, Peter Schneider, Will J. Sutherland, Massimo Viola, and Willem-Jan Vriend. The first and second data releases of the Kilo-Degree Survey. , 582:A62, October 2015. doi: 10.1051/0004-6361/201526601.

Tiziana Di Matteo, Volker Springel, and Lars Hernquist. Energy input from quasars regulates the growth and activity of black holes and their host galaxies. , 433(7026):604–607, February 2005. doi: 10.1038/nature03335.

S. P. Driver, D. T. Hill, L. S. Kelvin, A. S. G. Robotham, J. Liske, P. Norberg, I. K. Baldry, S. P. Bamford, A. M. Hopkins, J. Loveday, J. A. Peacock, E. Andrae, J. Bland-Hawthorn, S. Brough, M. J. I. Brown, E. Cameron, J. H. Y. Ching, M. Colless, C. J. Conselice, S. M. Croom, N. J. G. Cross, R. de Propris, S. Dye, M. J. Drinkwater, S. Ellis, Alister W. Graham, M. W. Grootes, M. Gunawardhana, D. H. Jones, E. van Kampen, C. Maraston, R. C. Nichol, H. R. Parkinson, S. Phillipps, K. Pimbblet, C. C. Popescu, M. Prescott, I. G. Roseboom, E. M. Sadler, A. E. Sansom, R. G. Sharp, D. J. B. Smith, E. Taylor, D. Thomas, R. J. Tuffs, D. Wijesinghe, L. Dunne, C. S. Frenk, M. J. Jarvis, B. F. Madore, M. J. Meyer, M. Seibert, L. Staveley-Smith, W. J. Sutherland, and S. J. Warren. Galaxy and Mass Assembly (GAMA): survey diagnostics and core data release. , 413(2):971–995, May 2011. doi: 10.1111/j.1365-2966.2010.18188.x.

Simon P. Driver, Angus H. Wright, Stephen K. Andrews, Luke J. Davies, Prajwal R. Kafle, Rebecca Lange, Amanda J. Moffett, Elizabeth Mannering, Aaron S. G. Robotham, Kevin Vinsen, Mehmet Alpaslan, Ellen Andrae, Ivan K. Baldry, Amanda E. Bauer, Steven P. Bamford, Joss Bland-Hawthorn, Nathan Bourne, Sarah Brough, Michael J. I. Brown, Michelle E. Cluver, Scott Croom, Matthew Colless, Christopher J. Conselice, Elisabete da Cunha, Roberto De Propris, Michael Drinkwater, Loretta Dunne, Steve Eales, Alastair Edge, Carlos Frenk, Alister W. Graham, Meiert Grootes, Benne W. Holwerda, Andrew M. Hopkins, Edo Ibar, Eelco van Kampen, Lee S. Kelvin, Tom Jarrett, D. Heath Jones, Maritza A. Lara-Lopez, Jochen Liske, Angel R. Lopez-Sanchez, Jon Loveday, Steve J. Maddox, Barry Madore, Smriti Mahajan, Martin Meyer, Peder Norberg, Samantha J. Penny, Steven Phillipps, Cristina Popescu, Richard J. Tuffs, John A. Peacock, Kevin A. Pimbblet, Matthew Prescott, Kate Rowlands, Anne E. Sansom, Mark Seibert, Matthew W. L. Smith, Will J. Sutherland, Edward N. Taylor, Elisabetta Valiante, J. Antonio Vazquez-Mata, Lingyu Wang, Stephen M. Wilkins, and Richard Williams. Galaxy And Mass Assembly (GAMA): Panchromatic Data Release (far-UV-far-IR) and the low-z energy budget. , 455(4):3911–3942, February 2016. doi: 10.1093/mnras/stv2505.

Simon P. Driver, Sabine Bellstedt, Aaron S. G. Robotham, Ivan K. Baldry, Luke J. Davies, Jochen Liske, Danail Obreschkow, Edward N. Taylor, Angus H. Wright, Mehmet Alpaslan, Steven P. Bamford, Amanda E. Bauer, Joss Bland-Hawthorn, Maciej Bilicki, Matías Bravo, Sarah Brough, Sarah Casura, Michelle E. Cluver, Matthew Colless, Christopher J. Conselice, Scott M. Croom, Jelte de Jong, Franceso D'Eugenio, Roberto De Propris, Burak Dogruel, Michael J. Drinkwater, Andrej Dvornik, Daniel J. Farrow, Carlos S. Frenk, Benjamin Giblin, Alister W. Graham, Meiert W. Grootes, Madusha L. P. Gunawardhana, Abdolhosein Hashemizadeh, Boris Häußler, Catherine Heymans, Hendrik Hildebrandt, Benne W. Holwerda, Andrew M. Hopkins, Tom H. Jarrett, D. Heath Jones, Lee S. Kelvin, Soheil Koushan, Konrad Kuijken, Maritza A. Lara-López, Rebecca Lange, Ángel R. López-Sánchez, Jon Loveday, Smriti Mahajan, Martin Meyer, Amanda J. Moffett, Nicola R. Napolitano, Peder Norberg, Matt S. Owers, Mario Radovich, Mojtaba Raouf, John A. Peacock, Steven Phillipps, Kevin A. Pimbblet, Cristina Popescu, Khaled Said, Anne E. Sansom, Mark Seibert, Will J. Sutherland, Jessica E. Thorne, Richard J. Tuffs, Ryan Turner, Arjen van der Wel, Eelco van Kampen, and Steve M. Wilkins. Galaxy And Mass Assembly (GAMA): Data Release 4 and the $z < 0.1$ total and $z < 0.08$ morphological galaxy stellar mass functions. , 513(1):439–467, June 2022. doi: 10.1093/mnras/stac472.

N. Drory, N. MacDonald, M. A. Bershady, K. Bundy, J. Gunn, D. R. Law, M. Smith, R. Stoll, C. A. Tremonti, D. A. Wake, R. Yan, A. M. Weijmans, N. Byler, B. Cherinka, F. Cope, A. Eigenbrot, P. Harding, D. Holder, J. Huehnerhoff, K. Jaehnig, T. C. Jansen, M. Klaene, A. M. Paat, J. Percival, and C. Sayres. The MaNGA Integral Field Unit Fiber Feed System for the Sloan 2.5 m Telescope. , 149(2):77, February 2015. doi: 10.1088/0004-6256/149/2/77.

Sara L. Ellison, David R. Patton, Luc Simard, and Alan W. McConnachie. Galaxy Pairs in the Sloan Digital Sky Survey. I. Star Formation, Active Galactic Nucleus Fraction, and the Mass-Metallicity Relation. , 135(5):1877–1899, May 2008. doi: 10.1088/0004-6256/135/5/1877.

Sara L. Ellison, David R. Patton, Preethi Nair, Luc Simard, J. Trevor Mendel, Alan W. McConnachie, and Jillian M. Scudder. Gas Flows in Galaxies: the Relative Importance of Mergers and Bars. In Claude Carignan, Françoise Combes, and Ken C. Freeman, editors, *Tracing the Ancestry of Galaxies*, volume 277 of *IAU Symposium*, pages 178–181, December 2011. doi: 10.1017/S1743921311022721.

Sara L. Ellison, J. Trevor Mendel, David R. Patton, and Jillian M. Scudder. Galaxy pairs in the Sloan Digital Sky Survey - VIII. The observational properties of post-merger galaxies. , 435(4):3627–3638, November 2013. doi: 10.1093/mnras/stt1562.

Sara L. Ellison, Scott Wilkinson, Joanna Woo, Ho-Hin Leung, Vivienne Wild, Robert W. Bickley, David R. Patton, Salvatore Quai, and Stephen Gwyn. Galaxy mergers can rapidly shut down star formation. , 517(1):L92–L96, November 2022. doi: 10.1093/mnrasl/slac109.

Santiago Erroz-Ferrer, C. Marcella Carollo, Mark den Brok, Masato Onodera, Jarle Brinchmann, Raffaella A. Marino, Ana Monreal-Ibero, Joop Schaye, Joanna Woo, Anna Cibinel, Victor P. Debattista, Hanae Inami, Michael Maseda, Johan Richard, Sandro Tacchella, and Lutz Wisotzki. The MUSE Atlas of Disks (MAD): resolving star formation rates and gas metallicities on <100 pc scales†. , 484(4):5009–5027, April 2019. doi: 10.1093/mnras/stz194.

ESA/Hubble and NASA. Merger tree illustration, 2018.

Robert Feldmann, Eliot Quataert, Claude-André Faucher-Giguère, Philip F. Hopkins, Onur Çatmabacak, Dušan Kereš, Luigi Bassini, Mauro Bernardini, James S. Bullock, Elia Cenci, Jindra Gensior, Lichen Liang, Jorge Moreno, and Andrew Wetzel. FIREbox: simulating galaxies at high dynamic range in a cosmological volume. , 522(3):3831–3860, July 2023. doi: 10.1093/mnras/stad1205.

Lisa M. R. Fogarty, Nicholas Scott, Matt S. Owers, S. Brough, Scott M. Croom, Michael B. Pracy, R. C. W. Houghton, Joss Bland-Hawthorn, Matthew Colless, Roger L. Davies, D. Heath Jones, J. T. Allen, Julia J. Bryant, Michael Goodwin, Andrew W. Green, Iraklis S. Konstantopoulos, J. S. Lawrence, Samuel Richards, Luca Cortese, and Rob Sharp. The SAMI Pilot Survey: the kinematic morphology–density relation in Abell 85, Abell 168 and Abell 2399. , 433(1):485–503, 2014. ISSN 1365-2966 0035-8711. doi: 10.1093/mnras/stu1165.

A. Fraser-McKelvie, L. Cortese, J. van de Sande, J. J. Bryant, B. Catinella, M. Colless, S. M. Croom, B. Groves, A. M. Medling, N. Scott, S. M. Sweet, J. Bland-Hawthorn, M. Goodwin, J. Lawrence, N. Lorente, M. S. Owers, and S. N. Richards. A SAMI and MaNGA view on the stellar kinematics of galaxies on the star-forming main sequence. , 503(4):4992–5005, May 2021. doi: 10.1093/mnras/stab573.

Alexander J. Gordon, Annette M. N. Ferguson, Robert G. Mann, and Vivienne Wild. Linking enhanced star formation and quenching to faint tidal features in galaxies. *arXiv e-prints*, art. arXiv:2507.21050, July 2025. doi: 10.48550/arXiv.2507.21050.

Andrew W. Green, Scott M. Croom, Nicholas Scott, Luca Cortese, Anne M. Medling, Francesco D'Eugenio, Julia J. Bryant, Joss Bland-Hawthorn, J. T. Allen, Rob Sharp, I.-Ting Ho, Brent Groves, Michael J. Drinkwater, Elizabeth Mannering, Lloyd Harischandra, Jesse van de Sande, Adam D. Thomas, Simon O'Toole, Richard M. McDermid, Minh Vuong, Katrina Sealey, Amanda E. Bauer, S. Brough, Barbara Catinella, Gerald Cecil, Matthew Colless, Warrick J. Couch, Simon P. Driver,

Christoph Federrath, Caroline Foster, Michael Goodwin, Elise J. Hampton, A. M. Hopkins, D. Heath Jones, Iraklis S. Konstantopoulos, J. S. Lawrence, Sergio G. Leon-Saval, Jochen Liske, Ángel R. López-Sánchez, Nuria P. F. Lorente, Jeremy Mould, Danail Obreschkow, Matt S. Owers, Samuel N. Richards, Aaron S. G. Robotham, Adam L. Schaefer, Sarah M. Sweet, Dan S. Taranu, Edoardo Tescari, Chiara Tonini, and T. Zafar. The SAMI Galaxy Survey: Data Release One with emission-line physics value-added products. , 475(1):716–734, March 2018. doi: 10.1093/mnras/stx3135.

Charles R. Harris, K. Jarrod Millman, Stéfan J. van der Walt, Ralf Gommers, Pauli Virtanen, David Cournapeau, Eric Wieser, Julian Taylor, Sebastian Berg, Nathaniel J. Smith, Robert Kern, Matti Picus, Stephan Hoyer, Marten H. van Kerkwijk, Matthew Brett, Allan Haldane, Jaime Fernández del Río, Mark Wiebe, Pearu Peterson, Pierre Gérard-Marchant, Kevin Sheppard, Tyler Reddy, Warren Weckesser, Hameer Abbasi, Christoph Gohlke, and Travis E. Oliphant. Array programming with NumPy. *Nature*, 585(7825):357–362, September 2020. doi: 10.1038/s41586-020-2649-2. URL https://doi.org/10.1038/s41586-020-2649-2.

Lars Hernquist. Tidal triggering of starbursts and nuclear activity in galaxies. , 340(6236):687–691, August 1989. doi: 10.1038/340687a0.

I.-Ting Ho, Anne M. Medling, Joss Bland-Hawthorn, Brent Groves, Lisa J. Kewley, Chiaki Kobayashi, Michael A. Dopita, Sarah K. Leslie, Rob Sharp, James T. Allen, Nathan Bourne, Julia J. Bryant, Luca Cortese, Scott M. Croom, Loretta Dunne, L. M. R. Fogarty, Michael Goodwin, Andy W. Green, Iraklis S. Konstantopoulos, Jon S. Lawrence, Nuria P. F. Lorente, Matt S. Owers, Samuel Richards, Sarah M. Sweet, Edoardo Tescari, and Elisabetta Valiante. The SAMI Galaxy Survey: extraplanar gas, galactic winds and their association with star formation history. , 457(2): 1257–1278, April 2016. doi: 10.1093/mnras/stw017.

A. M. Hopkins, S. P. Driver, S. Brough, M. S. Owers, A. E. Bauer, M. L. P. Gunawardhana, M. E. Cluver, M. Colless, C. Foster, M. A. Lara-López, I. Roseboom, R. Sharp, O. Steele, D. Thomas, I. K. Baldry, M. J. I. Brown, J. Liske, P. Norberg, A. S. G. Robotham, S. Bamford, J. Bland-Hawthorn, M. J. Drinkwater, J. Loveday, M. Meyer, J. A. Peacock, R. Tuffs, N. Agius, M. Alpaslan, E. Andrae, E. Cameron, S. Cole, J. H. Y. Ching, L. Christodoulou, C. Conselice, S. Croom, N. J. G. Cross, R. De Propris, J. Delhaize, L. Dunne, S. Eales, S. Ellis, C. S. Frenk, Alister W. Graham, M. W. Grootes, B. Häußler, C. Heymans, D. Hill, B. Hoyle, M. Hudson, M. Jarvis, J. Johansson, D. H. Jones, E. van Kampen, L. Kelvin, K. Kuijken, Á. López-Sánchez, S. Maddox, B. Madore, C. Maraston, T. McNaught-Roberts, R. C. Nichol, S. Oliver, H. Parkinson, S. Penny, S. Phillipps, K. A. Pimbblet, T. Ponman, C. C. Popescu, M. Prescott, R. Proctor, E. M. Sadler, A. E. Sansom, M. Seibert, L. Staveley-Smith, W. Sutherland, E. Taylor, L. Van Waerbeke, J. A. Vázquez-Mata, S. Warren, D. B. Wijesinghe, V. Wild, and S. Wilkins. Galaxy And Mass Assembly (GAMA): spectroscopic analysis. , 430(3):2047–2066, April 2013a. doi: 10.1093/mnras/stt030.

Philip F. Hopkins, Thomas J. Cox, Lars Hernquist, Desika Narayanan, Christopher C. Hayward, and Norman Murray. Star formation in galaxy mergers with realistic models of stellar feedback and the interstellar medium. , 430(3):1901–1927, April 2013b. doi: 10.1093/mnras/stt017.

J. D. Hunter. Matplotlib: A 2d graphics environment. *Computing in Science & Engineering*, 9(3): 90–95, 2007. doi: 10.1109/MCSE.2007.55.

J. Iglesias-Páramo, J. M. Vílchez, L. Galbany, S. F. Sánchez, F. F. Rosales-Ortega, D. Mast, R. García-Benito, B. Husemann, J. A. L. Aguerri, J. Alves, S. Bekeraité, J. Bland-Hawthorn, C. Catalán-Torrecilla, A. L. de Amorim, A. de Lorenzo-Cáceres, S. Ellis, J. Falcón-Barroso, H. Flores, E. Florido, A. Gallazzi, J. M. Gomes, R. M. González Delgado, T. Haines, J. D. Hernández-Fernández, C. Kehrig, A. R. López-Sánchez, M. Lyubenova, R. A. Marino, M. Mollá, A. Monreal-Ibero,

A. Mourão, P. Papaderos, M. Rodrigues, P. Sánchez-Blázquez, K. Spekkens, V. Stanishev, G. van de Ven, C. J. Walcher, L. Wisotzki, S. Zibetti, and B. Ziegler. Aperture corrections for disk galaxy properties derived from the CALIFA survey. Balmer emission lines in spiral galaxies. , 553:L7, May 2013. doi: 10.1051/0004-6361/201321460.

D. Heath Jones, Mike A. Read, Will Saunders, Matthew Colless, Tom Jarrett, Quentin A. Parker, Anthony P. Fairall, Thomas Mauch, Elaine M. Sadler, Fred G. Watson, Donna Burton, Lachlan A. Campbell, Paul Cass, Scott M. Croom, John Dawe, Kristin Fiegert, Leela Frankcombe, Malcolm Hartley, John Huchra, Dionne James, Emma Kirby, Ofer Lahav, John Lucey, Gary A. Mamon, Lesa Moore, Bruce A. Peterson, Sayuri Prior, Dominique Proust, Ken Russell, Vicky Safouris, Ken-Ichi Wakamatsu, Eduard Westra, and Mary Williams. The 6dF Galaxy Survey: final redshift release (DR3) and southern large-scale structures. , 399(2):683–698, October 2009. doi: 10.1111/j.1365-2966.2009.15338.x.

Lee S. Kelvin, Simon P. Driver, Aaron S. G. Robotham, David T. Hill, Mehmet Alpaslan, Ivan K. Baldry, Steven P. Bamford, Joss Bland-Hawthorn, Sarah Brough, Alister W. Graham, Boris Häussler, Andrew M. Hopkins, Jochen Liske, Jon Loveday, Peder Norberg, Steven Phillipps, Cristina C. Popescu, Matthew Prescott, Edward N. Taylor, and Richard J. Tuffs. Galaxy And Mass Assembly (GAMA): Structural Investigation of Galaxies via Model Analysis. , 421(2):1007–1039, April 2012. doi: 10.1111/j.1365-2966.2012.20355.x.

R. C. Kennicutt, K. A. Roettiger, W. C. Keel, J. M. van der Hulst, and E. Hummel. Induced Star Formation in Interacting Galaxies. In Carol J. Lonsdale Persson, editor, *NASA Conference Publication*, volume 2466 of *NASA Conference Publication*, pages 401–408, May 1987a.

Robert C. Kennicutt and Neal J. Evans. Star Formation in the Milky Way and Nearby Galaxies. , 50:531–608, September 2012. doi: 10.1146/annurev-astro-081811-125610.

Robert C. Kennicutt, Jr. Star Formation in Galaxies Along the Hubble Sequence. , 36:189–232, January 1998. doi: 10.1146/annurev.astro.36.1.189.

Robert C. Kennicutt, Jr., William C. Keel, J. M. van der Hulst, E. Hummel, and Kurt A. Roettiger. The Effects of Interactions on Spiral Galaxies. II. Disk Star Formation Rates. , 93:1011, May 1987b. doi: 10.1086/114384.

Lisa J. Kewley, Rolf A. Jansen, and Margaret J. Geller. Aperture Effects on Star Formation Rate, Metallicity, and Reddening. , 117(829):227–244, March 2005. doi: 10.1086/428303.

Lisa J. Kewley, Margaret J. Geller, and Elizabeth J. Barton. Metallicity and Nuclear Star Formation in Nearby Galaxy Pairs: Evidence for Tidally Induced Gas Flows. , 131(4):2004–2017, April 2006. doi: 10.1086/500295.

D. G. Lambas, S. Alonso, V. Mesa, and A. L. O'Mill. Galaxy interactions. I. Major and minor mergers. , 539:A45, March 2012. doi: 10.1051/0004-6361/201117900.

R. B. Larson and B. M. Tinsley. Star formation rates in normal and peculiar galaxies. , 219:46–59, January 1978. doi: 10.1086/155753.

Song-lin Li, Yong Shi, Dmitry Bizyaev, Christopher Duckworth, Ren-bin Yan, Yan-mei Chen, Long-ji Bing, Jian-hang Chen, Xiao-ling Yu, and Rogemar A. Riffel. The impact of merging on the origin of kinematically misaligned and counter-rotating galaxies in MaNGA. , 501(1):14–23, January 2021. doi: 10.1093/mnras/staa3618.

Lihwai Lin, Bau-Ching Hsieh, Hsi-An Pan, Sandro B. Rembold, Sebastián F. Sánchez, Maria Argudo-Fernández, Kate Rowlands, Francesco Belfiore, Dmitry Bizyaev, Ivan Lacerna, Rogréio Riffel, Yu Rong, Fangting Yuan, Niv Drory, Roberto Maiolino, and Eric Wilcots. SDSS-IV MaNGA: Inside-out versus Outside-in Quenching of Galaxies in Different Local Environments. , 872(1):50, February 2019. doi: 10.3847/1538-4357/aafa84.

J. Liske, I. K. Baldry, S. P. Driver, R. J. Tuffs, M. Alpaslan, E. Andrae, S. Brough, M. E. Cluver, M. W. Grootes, M. L. P. Gunawardhana, L. S. Kelvin, J. Loveday, A. S. G. Robotham, E. N. Taylor, S. P. Bamford, J. Bland-Hawthorn, M. J. I. Brown, M. J. Drinkwater, A. M. Hopkins, M. J. Meyer, P. Norberg, J. A. Peacock, N. K. Agius, S. K. Andrews, A. E. Bauer, J. H. Y. Ching, M. Colless, C. J. Conselice, S. M. Croom, L. J. M. Davies, R. De Propris, L. Dunne, E. M. Eardley, S. Ellis, C. Foster, C. S. Frenk, B. Häußler, B. W. Holwerda, C. Howlett, H. Ibarra, M. J. Jarvis, D. H. Jones, P. R. Kafle, C. G. Lacey, R. Lange, M. A. Lara-López, Á. R. López-Sánchez, S. Maddox, B. F. Madore, T. McNaught-Roberts, A. J. Moffett, R. C. Nichol, M. S. Owers, D. Palamara, S. J. Penny, S. Phillipps, K. A. Pimbblet, C. C. Popescu, M. Prescott, R. Proctor, E. M. Sadler, A. E. Sansom, M. Seibert, R. Sharp, W. Sutherland, J. A. Vázquez-Mata, E. van Kampen, S. M. Wilkins, R. Williams, and A. H. Wright. Galaxy And Mass Assembly (GAMA): end of survey report and data release 2. , 452(2):2087–2126, September 2015. doi: 10.1093/mnras/stv1436.

Rebecca McElroy, Connor Bottrell, Maan H. Hani, Jorge Moreno, Scott M. Croom, Christopher C. Hayward, Angela Twum, Robert Feldmann, Philip F. Hopkins, Lars Hernquist, and Bernd Husemann. The observability of galaxy merger signatures in nearby gas-rich spirals. , 515(3):3406–3419, September 2022. doi: 10.1093/mnras/stac1715.

Anne M. Medling, Luca Cortese, Scott M. Croom, Andrew W. Green, Brent Groves, Elise Hampton, I. Ting Ho, Luke J. M. Davies, Lisa J. Kewley, Amanda J. Moffett, Adam L. Schaefer, Edward Taylor, Tayyaba Zafar, Kenji Bekki, Joss Bland-Hawthorn, Jessica V. Bloom, Sarah Brough, Julia J. Bryant, Barbara Catinella, Gerald Cecil, Matthew Colless, Warrick J. Couch, Michael J. Drinkwater, Simon P. Driver, Christoph Federrath, Caroline Foster, Gregory Goldstein, Michael Goodwin, Andrew Hopkins, J. S. Lawrence, Sarah K. Leslie, Geraint F. Lewis, Nuria P. F. Lorente, Matt S. Owers, Richard McDermid, Samuel N. Richards, Robert Sharp, Nicholas Scott, Sarah M. Sweet, Dan S. Taranu, Edoardo Tescari, Chiara Tonini, Jesse van de Sande, C. Jakob Walcher, and Angus Wright. The SAMI Galaxy Survey: spatially resolving the main sequence of star formation. , 475(4): 5194–5214, April 2018. doi: 10.1093/mnras/sty127.

Valeria Mesa, Sol Alonso, Georgina Coldwell, Diego García Lambas, and J. L. Nilo Castellon. Satellites and central galaxies in SDSS: the influence of interactions on their properties. , 501(1):1046–1058, February 2021. doi: 10.1093/mnras/staa3720.

J. Christopher Mihos and Lars Hernquist. Gasdynamics and Starbursts in Major Mergers. , 464: 641, June 1996. doi: 10.1086/177353.

Mahesh Mohanan, Julia Bryant, Rebecca Brown, Scott Croom, Robert Content, Tony Farrell, Michael Goodwin, Jonathan Bland-Hawthorn, Ellen Houston, Urs Klauser, Jon Lawrence, Helen McGregor, Naveen Pai, David Robertson, Will Saunders, Lew Waller, Ross Zhelem, and Jessica Zheng. Hector spectrograph (spector): mechanical engineering overview. In Christopher J. Evans, Julia J. Bryant, and Kentaro Motohara, editors, *Ground-based and Airborne Instrumentation for Astronomy IX*, volume 12184 of *Society of Photo-Optical Instrumentation Engineers (SPIE) Conference Series*, page 121847P, August 2022. doi: 10.1117/12.2630617.

Jorge Moreno, Paul Torrey, Sara L. Ellison, David R. Patton, Asa F. L. Bluck, Gunjan Bansal, and Lars Hernquist. Mapping galaxy encounters in numerical simulations: the spatial extent of induced star formation. , 448(2):1107–1117, April 2015. doi: 10.1093/mnras/stv094.

Jorge Moreno, Paul Torrey, Sara L. Ellison, David R. Patton, Connor Bottrell, Asa F. L. Bluck, Maan H. Hani, Christopher C. Hayward, James S. Bullock, Philip F. Hopkins, and Lars Hernquist. Spatially resolved star formation and fuelling in galaxy interactions. , 503(3):3113–3133, May 2021. doi: 10.1093/mnras/staa2952.

Dylan Nelson, Volker Springel, Annalisa Pillepich, Vicente Rodriguez-Gomez, Paul Torrey, Shy Genel, Mark Vogelsberger, Ruediger Pakmor, Federico Marinacci, Rainer Weinberger, Luke Kelley, Mark Lovell, Benedikt Diemer, and Lars Hernquist. The IllustrisTNG simulations: public data release. *Computational Astrophysics and Cosmology*, 6(1):2, May 2019. doi: 10.1186/s40668-019-0028-x.

G. Neugebauer, H. J. Habing, R. van Duinen, H. H. Aumann, B. Baud, C. A. Beichman, D. A. Beintema, N. Boggess, P. E. Clegg, T. de Jong, J. P. Emerson, T. N. Gautier, F. C. Gillett, S. Harris, M. G. Hauser, J. R. Houck, R. E. Jennings, F. J. Low, P. L. Marsden, G. Miley, F. M. Olnon, S. R. Pottasch, E. Raimond, M. Rowan-Robinson, B. T. Soifer, R. G. Walker, P. R. Wesselius, and E. Young. The Infrared Astronomical Satellite (IRAS) Mission. , 278:L1–L6, March 1984. doi: 10.1086/184209.

Sree Oh, Keunho Kim, Joon Hyeop Lee, Minjin Kim, Yun-Kyeong Sheen, Jinsu Rhee, Chang H. Ree, Hyunjin Jeong, Luis C. Ho, Jaemann Kyeong, Eon-Chang Sung, Byeong-Gon Park, and Sukyoung K. Yi. Impact of galaxy mergers on the colours of cluster galaxies. , 488(3):4169–4180, September 2019. doi: 10.1093/mnras/stz1920.

L. Pasquini, G. Avila, A. Blecha, C. Cacciari, V. Cayatte, M. Colless, F. Damiani, R. de Propris, H. Dekker, P. di Marcantonio, T. Farrell, P. Gillingham, I. Guinouard, F. Hammer, A. Kaufer, V. Hill, M. Marteaud, A. Modigliani, G. Mulas, P. North, D. Popovic, E. Rossetti, F. Royer, P. Santin, R. Schmutzer, G. Simond, P. Vola, L. Waller, and M. Zoccali. Installation and commissioning of FLAMES, the VLT Multifibre Facility. *The Messenger*, 110:1–9, December 2002.

W. J. Pearson, L. Wang, M. Alpaslan, I. Baldry, M. Bilicki, M. J. I. Brown, M. W. Grootes, B. W. Holwerda, T. D. Kitching, S. Kruk, and F. F. S. van der Tak. Effect of galaxy mergers on star-formation rates. , 631:A51, November 2019. doi: 10.1051/0004-6361/201936337.

E. Pérez, R. Cid Fernandes, R. M. González Delgado, R. García-Benito, S. F. Sánchez, B. Husemann, D. Mast, J. R. Rodón, D. Kupko, N. Backsmann, A. L. de Amorim, G. van de Ven, J. Walcher, L. Wisotzki, C. Cortijo-Ferrero, and CALIFA Collaboration. The Evolution of Galaxies Resolved in Space and Time: A View of Inside-out Growth from the CALIFA Survey. , 764(1):L1, February 2013. doi: 10.1088/2041-8205/764/1/L1.

Jonathan Petersson, Florent Renaud, Oscar Agertz, Avishai Dekel, and Pierre-Alain Duc. From starburst to quenching: merger-driven evolution of the star formation regimes in a shell galaxy. , 518 (3):3261–3273, January 2023. doi: 10.1093/mnras/stac3136.

T. Robin, Sreeja S. Kartha, R. Akhil Krishna, Ujjwal Krishnan, Blesson Mathew, T. B. Cysil, Narendra Nath Patra, and B. Shridharan. The Interaction Jigsaw: investigating star formation in interacting galaxies. , 534(3):1902–1912, November 2024. doi: 10.1093/mnras/stae2211.

A. S. G. Robotham, P. Norberg, S. P. Driver, I. K. Baldry, S. P. Bamford, A. M. Hopkins, J. Liske, J. Loveday, A. Merson, J. A. Peacock, S. Brough, E. Cameron, C. J. Conselice, S. M. Croom, C. S. Frenk, M. Gunawardhana, D. T. Hill, D. H. Jones, L. S. Kelvin, K. Kuijken, R. C. Nichol, H. R. Parkinson, K. A. Pimbblet, S. Phillipps, C. C. Popescu, M. Prescott, R. G. Sharp, W. J. Sutherland, E. N. Taylor, D. Thomas, R. J. Tuffs, E. van Kampen, and D. Wijesinghe. Galaxy and Mass Assembly (GAMA): the GAMA galaxy group catalogue (G^3Cv1). , 416(4):2640–2668, October 2011. doi: 10.1111/j.1365-2966.2011.19217.x.

A. S. G. Robotham, S. P. Driver, L. J. M. Davies, A. M. Hopkins, I. K. Baldry, N. K. Agius, A. E. Bauer, J. Bland-Hawthorn, S. Brough, M. J. I. Brown, M. Cluver, R. De Propris, M. J. Drinkwater, B. W. Holwerda, L. S. Kelvin, M. A. Lara-Lopez, J. Liske, Á. R. López-Sánchez, J. Loveday, S. Mahajan, T. McNaught-Roberts, A. Moffett, P. Norberg, D. Obreschkow, M. S. Owers, S. J. Penny, K. Pimbblet, M. Prescott, E. N. Taylor, E. van Kampen, and S. M. Wilkins. Galaxy And Mass Assembly (GAMA): galaxy close pairs, mergers and the future fate of stellar mass. , 444(4):3986–4008, November 2014. doi: 10.1093/mnras/stu1604.

Amélie Saintonge, Linda J. Tacconi, Silvia Fabello, Jing Wang, Barbara Catinella, Reinhard Genzel, Javier Graciá-Carpio, Carsten Kramer, Sean Moran, Timothy M. Heckman, David Schiminovich, Karl Schuster, and Stijn Wuyts. The Impact of Interactions, Bars, Bulges, and Active Galactic Nuclei on Star Formation Efficiency in Local Massive Galaxies. , 758(2):73, October 2012. doi: 10.1088/0004-637X/758/2/73.

S. F. Sánchez, R. C. Kennicutt, A. Gil de Paz, G. van de Ven, J. M. Vílchez, L. Wisotzki, C. J. Walcher, D. Mast, J. A. L. Aguerri, S. Albiol-Pérez, A. Alonso-Herrero, J. Alves, J. Bakos, T. Bartáková, J. Bland-Hawthorn, A. Boselli, D. J. Bomans, A. Castillo-Morales, C. Cortijo-Ferrero, A. de Lorenzo-Cáceres, A. Del Olmo, R.-J. Dettmar, A. Díaz, S. Ellis, J. Falcón-Barroso, H. Flores, A. Gallazzi, B. García-Lorenzo, R. González Delgado, N. Gruel, T. Haines, C. Hao, B. Husemann, J. Iglésias-Páramo, K. Jahnke, B. Johnson, B. Jungwiert, V. Kalinova, C. Kehrig, D. Kupko, Á. R. López-Sánchez, M. Lyubenova, R. A. Marino, E. Mármol-Queraltó, I. Márquez, J. Masegosa, S. Meidt, J. Mendez-Abreu, A. Monreal-Ibero, C. Montijo, A. M. Mourão, G. Palacios-Navarro, P. Papaderos, A. Pasquali, R. Peletier, E. Pérez, I. Pérez, A. Quirrenbach, M. Relaño, F. F. Rosales-Ortega, M. M. Roth, T. Ruiz-Lara, P. Sánchez-Blázquez, C. Sengupta, R. Singh, V. Stanishev, S. C. Trager, A. Vazdekis, K. Viironen, V. Wild, S. Zibetti, and B. Ziegler. CALIFA, the Calar Alto Legacy Integral Field Area survey. I. Survey presentation. , 538:A8, February 2012. doi: 10.1051/0004-6361/201117353.

D. B. Sanders, N. Z. Scoville, J. S. Young, B. T. Soifer, F. P. Schloerb, W. L. Rice, and G. E. Danielson. Molecular Gas in High-Luminosity IRAS Galaxies. , 305:L45, June 1986. doi: 10.1086/184682.

A. L. Schaefer, S. M. Croom, J. T. Allen, S. Brough, A. M. Medling, I.-T. Ho, N. Scott, S. N. Richards, M. B. Pracy, M. L. P. Gunawardhana, P. Norberg, M. Alpaslan, A. E. Bauer, K. Bekki, J. Bland-Hawthorn, J. V. Bloom, J. J. Bryant, W. J. Couch, S. P. Driver, L. M. R. Fogarty, C. Foster, G. Goldstein, A. W. Green, A. M. Hopkins, I. S. Konstantopoulos, J. S. Lawrence, A. R. López-Sánchez, N. P. F. Lorente, M. S. Owers, R. Sharp, S. M. Sweet, E. N. Taylor, J. van de Sande, C. J. Walcher, and O. I. Wong. The SAMI Galaxy Survey: spatially resolving the environmental quenching of star formation in GAMA galaxies. , 464(1):121–142, January 2017. doi: 10.1093/mnras/stw2289.

Kasper B. Schmidt, Hans-Walter Rix, Elisabete da Cunha, Gabriel B. Brammer, Thomas J. Cox, Pieter van Dokkum, Natascha M. Förster Schreiber, Marijn Franx, Mattia Fumagalli, Patrik Jonsson, Britt Lundgren, Michael V. Maseda, Ivelina Momcheva, Erica J. Nelson, Rosalind E. Skelton, Arjen van der Wel, and Katherine E. Whitaker. The spatial extent and distribution of star formation in 3D-HST mergers at z ~ 1.5. , 432(1):285–300, June 2013. doi: 10.1093/mnras/stt459.

Francois Schweizer. Star Formation in Colliding and Merging Galaxies. In Sandra M. Faber, editor, *Nearly Normal Galaxies. From the Planck Time to the Present*, page 18, January 1987.

Nicholas Scott, S. Brough, Scott M. Croom, Roger L. Davies, Jesse van de Sande, J. T. Allen, Joss Bland-Hawthorn, Julia J. Bryant, Luca Cortese, Francesco D'Eugenio, Christoph Federrath, Ignacio Ferreras, Michael Goodwin, Brent Groves, Iraklis Konstantopoulos, Jon S. Lawrence, Anne M. Medling, Amanda J. Moffett, Matt S. Owers, Samuel Richards, A. S. G. Robotham, Chiara Tonini,

and Sukyoung K. Yi. The SAMI Galaxy Survey: global stellar populations on the size-mass plane. , 472(3):2833–2855, December 2017. doi: 10.1093/mnras/stx2166.

Nicholas Scott, Jesse van de Sande, Scott M. Croom, Brent Groves, Matt S. Owers, Henry Poetrodjojo, Francesco D'Eugenio, Anne M. Medling, Dilyar Barat, Tania M. Barone, Joss Bland-Hawthorn, Sarah Brough, Julia Bryant, Luca Cortese, Caroline Foster, Andrew W. Green, Sree Oh, Matthew Colless, Michael J. Drinkwater, Simon P. Driver, Michael Goodwin, Madusha L. P. Gunawardhana, Christoph Federrath, Lloyd Harischandra, Yifei Jin, J. S. Lawrence, Nuria P. Lorente, Elizabeth Mannering, Simon O'Toole, Samuel N. Richards, Sebastian F. Sanchez, Adam L. Schaefer, Katrina Sealey, Rob Sharp, Sarah M. Sweet, Dan S. Taranu, and Mathew Varidel. The SAMI Galaxy Survey: Data Release Two with absorption-line physics value-added products. , 481(2):2299–2319, December 2018. doi: 10.1093/mnras/sty2355.

Jillian M. Scudder, Sara L. Ellison, Paul Torrey, David R. Patton, and J. Trevor Mendel. Galaxy pairs in the Sloan Digital Sky Survey - V. Tracing changes in star formation rate and metallicity out to separations of 80 kpc. , 426(1):549–565, October 2012. doi: 10.1111/j.1365-2966.2012.21749.x.

SDSS Collaboration, Gautham Adamane Pallathadka, Mojgan Aghakhanloo, James Aird, Andrés Almeida, Singh Amrita, Friedrich Anders, Scott F. Anderson, Stefan Arseneau, Consuelo González Avila, Shir Aviram, Catarina Aydar, Carles Badenes, Jorge K. Barrera-Ballesteros, Franz E. Bauer, Aida Behmard, Michelle Berg, F. Besser, Christian Moni Bidin, Dmitry Bizyaev, Guillermo Blanc, Michael R. Blanton, Jo Bovy, William Nielsen Brandt, Joel R. Brownstein, Johannes Buchner, Esra Bulbul, Joseph N. Burchett, Leticia Carigi, Joleen K. Carlberg, Andrew R. Casey, Priyanka Chakraborty, Julio Chanamé, Vedant Chandra, Cristina Chiappini, Igor Chilingarian, Johan Comparat, Kevin Covey, Nicole Crumpler, Katia Cunha, Elena D'Onghia, Xinyu Dai, Jeremy Darling, Megan Davis, Nathan De Lee, Niall Deacon, José Eduardo Méndez Delgado, Sebastian Demasi, Mariia Demianenko, Delvin Demke, John Donor, Niv Drory, Monica Alejandra Villa Durango, Tom Dwelly, Oleg Egorov, Evgeniya Egorova, Kareem El-Badry, Mike Eracleous, Xiaohui Fan, Emily Farr, Douglas P. Finkbeiner, Logan Fries, Peter Frinchaboy, Nicola Pietro Gentile Fusillo, Luis Daniel Serrano Félix, Boris Gaensicke, Emma Galligan, Pablo García, Joseph Gelfand, Katie Grabowski, Eva Grebel, Paul J Green, Hannah Greve, Catherine Grier, Emily Griffith, Paloma Guetzoyan, Pramod Gupta, Zoe Hackshaw, Patrick B. Hall, Keith Hawkins, Viola Hegedűs, Saskia Hekker, T. M. Herbst, J. J. Hermes, Lorena Hernández-García, Pranavi Hiremath, David W Hogg, Jon Holtzman, Keith Horne, Danny Horta, Yang Huang, Brian Hutchinson, Maximilian Häberle, Hector Javier Ibarra-Medel, Alexander P. Ji, Paula Jofre, James W. Johnson, Jennifer Johnson, Evelyn J. Johnston, Mary Kaldor, Ivan Katkov, Arman Khalatyan, Sergey Khoperskov, Ralf Klessen, Matthias Kluge, Anton M. Koekemoer, Juna A. Kollmeier, Marina Kounkel, Kathryn Kreckel, Dhanesh Krishnarao, Mirko Krumpe, Ivan Lacerna, Chervin Laporte, Sebastien Lepine, Jing Li, Fu-Heng Liang, Guilherme Limberg, Xin Liu, Sarah Loebman, Knox Long, Yuxi Lu, Madeline Lucey, Alejandra Z. Lugo-Aranda, Mary Loli Martínez Martinez-Aldama, Kevin McKinnon, Ilija Medan, Andrea Merloni, Sean Morrison, Natalie Myers, Szabolcs Mészáros, Johanna Müller-Horn, Samir Nepal, Melissa Ness, David Nidever, Christian Nitschelm, Audrey Oravetz, Jonah Otto, Kaike Pan, Facundo Pérez Paolino, Castalia Alenka Negrete Peñaloza, Marc Pinsonneault, Manuchehr Taghizadeh Popp, Adrian Price-Whelan, Nadiia Pulatova, Anna Barbara Queiroz, Jordan Raddick, Amy Rankine, Hans-Walter Rix, Carlos Román-Zúñiga, Daniela Fernández Rosso, Jessie Runnoe, Serat Mahmud Saad, Mara Salvato, Sebastian F. Sanchez, Natascha Sattler, Andrew Saydjari, Conor Sayres, Kevin Schlaufman, Donald P. Schneider, Axel Schwope, Lucas M. Seaton, Rhys Seeburger, Javier Serna, Sanjib Sharma, Yue Shen, Amaya Sinha, Brian Sizemore, Marzena Sniegowska, Yingyi Song, Diogo Souto, Keivan Stassun, Matthias Steinmetz, Zachary Stone, Alexander Stone-Martinez, Guy S. Stringfellow, Aurora Mata Sánchez, José Sánchez-Gallego, Jonathan Tan, Jamie Tayar, Riley Thai, Ani Thakar, Pierre Thibodeaux, Yuan-Sen Ting, Andrew Tkachenko, Benny Trakhtenbrot,

Jose G. Fernandez Trincado, Nicholas Troup, Jonathan R. Trump, Natalie Ulloa, Roeland P. Van der Marel, Pablo Vera, Sandro Villanova, Jaime Villaseñor, Ji Wang, Zachary Way, Anne-Marie Weijmans, Adam Wheeler, John C. Wilson, Aida Wofford, and Tony Wong. The Nineteenth Data Release of the Sloan Digital Sky Survey. *arXiv e-prints*, art. arXiv:2507.07093, July 2025. doi: 10.48550/arXiv.2507.07093.

Robert Sharp, Will Saunders, Greg Smith, Vladimir Churilov, David Correll, John Dawson, Tony Farrel, Gabriella Frost, Roger Haynes, Ron Heald, Allan Lankshear, Don Mayfield, Lew Waller, and Dennis Whittard. Performance of AAOmega: the AAT multi-purpose fiber-fed spectrograph. In Ian S. McLean and Masanori Iye, editors, *Ground-based and Airborne Instrumentation for Astronomy*, volume 6269 of *Society of Photo-Optical Instrumentation Engineers (SPIE) Conference Series*, page 62690G, June 2006. doi: 10.1117/12.671022.

Greg A. Smith, Will Saunders, Terry Bridges, Vladimir Churilov, Allan Lankshear, John Dawson, David Correll, Lew Waller, Roger Haynes, and Gabriella Frost. AAOmega: a multipurpose fiber-fed spectrograph for the AAT. In Alan F. M. Moorwood and Masanori Iye, editors, *Ground-based Instrumentation for Astronomy*, volume 5492 of *Society of Photo-Optical Instrumentation Engineers (SPIE) Conference Series*, pages 410–420, September 2004. doi: 10.1117/12.551013.

B. T. Soifer, C. A. Beichman, J. R. Houck, G. Neugebauer, and M. Rowan-Robinson. Preliminary Scientific Results From The First Six Months Of The Infrared Astronomy Satellite (IRAS). In *Society of Photo-Optical Instrumentation Engineers (SPIE) Conference Series*, volume 430 of *Society of Photo-Optical Instrumentation Engineers (SPIE) Conference Series*, pages 297–301, January 1984. doi: 10.1117/12.936401.

B. T. Soifer, G. Neugebauer, and J. R. Houck. The IRAS view of the extragalactic sky. , 25:187–230, January 1987. doi: 10.1146/annurev.aa.25.090187.001155.

Martin Sparre, Joseph Whittingham, Mitali Damle, Maan H. Hani, Philipp Richter, Sara L. Ellison, Christoph Pfrommer, and Mark Vogelsberger. Gas flows in galaxy mergers: supersonic turbulence in bridges, accretion from the circumgalactic medium, and metallicity dilution. , 509(2):2720–2735, January 2022. doi: 10.1093/mnras/stab3171.

Volker Springel, Tiziana Di Matteo, and Lars Hernquist. Modelling feedback from stars and black holes in galaxy mergers. , 361(3):776–794, August 2005. doi: 10.1111/j.1365-2966.2005.09238.x.

S. Tacchella, C. M. Carollo, A. Renzini, N. M. Förster Schreiber, P. Lang, S. Wuyts, G. Cresci, A. Dekel, R. Genzel, S. J. Lilly, C. Mancini, S. Newman, M. Onodera, A. Shapley, L. Tacconi, J. Woo, and G. Zamorani. Evidence for mature bulges and an inside-out quenching phase 3 billion years after the Big Bang. *Science*, 348(6232):314–317, April 2015. doi: 10.1126/science.1261094.

Edward N. Taylor, Andrew M. Hopkins, Ivan K. Baldry, Michael J. I. Brown, Simon P. Driver, Lee S. Kelvin, David T. Hill, Aaron S. G. Robotham, Joss Bland-Hawthorn, D. H. Jones, R. G. Sharp, Daniel Thomas, Jochen Liske, Jon Loveday, Peder Norberg, J. A. Peacock, Steven P. Bamford, Sarah Brough, Matthew Colless, Ewan Cameron, Christopher J. Conselice, Scott M. Croom, C. S. Frenk, Madusha Gunawardhana, Konrad Kuijken, R. C. Nichol, H. R. Parkinson, S. Phillipps, K. A. Pimbblet, C. C. Popescu, Matthew Prescott, W. J. Sutherland, R. J. Tuffs, Eelco van Kampen, and D. Wijesinghe. Galaxy And Mass Assembly (GAMA): stellar mass estimates. , 418(3):1587–1620, December 2011. doi: 10.1111/j.1365-2966.2011.19536.x.

Romain Teyssier, Damien Chapon, and Frédéric Bournaud. The Driving Mechanism of Starbursts in Galaxy Mergers. , 720(2):L149–L154, September 2010. doi: 10.1088/2041-8205/720/2/L149.

Mallory D. Thorp, Sara L. Ellison, Luc Simard, Sebastian F. Sánchez, and Braulio Antonio. Spatially resolved star formation and metallicity profiles in post-merger galaxies from MaNGA. , 482(1):L55–L59, January 2019. doi: 10.1093/mnrasl/sly185.

B. M. Tinsley and R. B. Larson. Stellar population explosions in proto-elliptical galaxies. , 186: 503–517, February 1979. doi: 10.1093/mnras/186.3.503.

Alar Toomre and Juri Toomre. Galactic Bridges and Tails. , 178:623–666, December 1972. doi: 10.1086/151823.

Sujeeporn Tuntipong, Jesse van de Sande, Scott M. Croom, Stefania Barsanti, Joss Bland-Hawthorn, Sarah Brough, Julia J. Bryant, Sarah Casura, Amelia Fraser-McKelvie, Jon S. Lawrence, Andrei Ristea, Sarah M. Sweet, and Tayyaba Zafar. The SAMI galaxy survey: on the importance of applying multiple selection criteria for finding Milky Way analogues. , 533(4):4334–4359, October 2024. doi: 10.1093/mnras/stae2042.

J. V. Villumsen. Simulations of galaxy mergers. , 199:493–516, May 1982. doi: 10.1093/mnras/199.3.493.

Pauli Virtanen, Ralf Gommers, Travis E. Oliphant, Matt Haberland, Tyler Reddy, David Cournapeau, Evgeni Burovski, Pearu Peterson, Warren Weckesser, Jonathan Bright, Stéfan J. van der Walt, Matthew Brett, Joshua Wilson, K. Jarrod Millman, Nikolay Mayorov, Andrew R. J. Nelson, Eric Jones, Robert Kern, Eric Larson, C J Carey, İlhan Polat, Yu Feng, Eric W. Moore, Jake VanderPlas, Denis Laxalde, Josef Perktold, Robert Cimrman, Ian Henriksen, E. A. Quintero, Charles R. Harris, Anne M. Archibald, Antônio H. Ribeiro, Fabian Pedregosa, Paul van Mulbregt, and SciPy 1.0 Contributors. SciPy 1.0: Fundamental Algorithms for Scientific Computing in Python. *Nature Methods*, 17:261–272, 2020. doi: 10.1038/s41592-019-0686-2.

Wes McKinney. Data Structures for Statistical Computing in Python. In Stéfan van der Walt and Jarrod Millman, editors, *Proceedings of the 9th Python in Science Conference*, pages 56 – 61, 2010. doi: 10.25080/Majora-92bf1922-00a.

S. D. M. White. Simulations of merging galaxies. , 184:185–203, July 1978. doi: 10.1093/mnras/184.2.185.

S. D. M. White and M. J. Rees. Core condensation in heavy halos: a two-stage theory for galaxy formation and clustering. , 183:341–358, May 1978. doi: 10.1093/mnras/183.3.341.

Deborah Freedman Woods and Margaret J. Geller. Minor Galaxy Interactions: Star Formation Rates and Galaxy Properties. , 134(2):527–540, August 2007. doi: 10.1086/519381.

Donald G. York, J. Adelman, John E. Anderson, Jr., Scott F. Anderson, James Annis, Neta A. Bahcall, J. A. Bakken, Robert Barkhouser, Steven Bastian, Eileen Berman, William N. Boroski, Steve Bracker, Charlie Briegel, John W. Briggs, J. Brinkmann, Robert Brunner, Scott Burles, Larry Carey, Michael A. Carr, Francisco J. Castander, Bing Chen, Patrick L. Colestock, A. J. Connolly, J. H. Crocker, István Csabai, Paul C. Czarapata, John Eric Davis, Mamoru Doi, Tom Dombeck, Daniel Eisenstein, Nancy Ellman, Brian R. Elms, Michael L. Evans, Xiaohui Fan, Glenn R. Federwitz, Larry Fiscelli, Scott Friedman, Joshua A. Frieman, Masataka Fukugita, Bruce Gillespie, James E. Gunn, Vijay K. Gurbani, Ernst de Haas, Merle Haldeman, Frederick H. Harris, J. Hayes, Timothy M. Heckman, G. S. Hennessy, Robert B. Hindsley, Scott Holm, Donald J. Holmgren, Chi-hao Huang, Charles Hull, Don Husby, Shin-Ichi Ichikawa, Takashi Ichikawa, Željko Ivezić, Stephen Kent, Rita S. J. Kim, E. Kinney, Mark Klaene, A. N. Kleinman, S. Kleinman, G. R. Knapp, John Korienek, Richard G. Kron, Peter Z. Kunszt, D. Q. Lamb, B. Lee, R. French Leger, Siriluk Limmongkol,

Carl Lindenmeyer, Daniel C. Long, Craig Loomis, Jon Loveday, Rich Lucinio, Robert H. Lupton, Bryan MacKinnon, Edward J. Mannery, P. M. Mantsch, Bruce Margon, Peregrine McGehee, Timothy A. McKay, Avery Meiksin, Aronne Merelli, David G. Monet, Jeffrey A. Munn, Vijay K. Narayanan, Thomas Nash, Eric Neilsen, Rich Neswold, Heidi Jo Newberg, R. C. Nichol, Tom Nicinski, Mario Nonino, Norio Okada, Sadanori Okamura, Jeremiah P. Ostriker, Russell Owen, A. George Pauls, John Peoples, R. L. Peterson, Donald Petravick, Jeffrey R. Pier, Adrian Pope, Ruth Pordes, Angela Prosapio, Ron Rechenmacher, Thomas R. Quinn, Gordon T. Richards, Michael W. Richmond, Claudio H. Rivetta, Constance M. Rockosi, Kurt Ruthmansdorfer, Dale Sandford, David J. Schlegel, Donald P. Schneider, Maki Sekiguchi, Gary Sergey, Kazuhiro Shimasaku, Walter A. Siegmund, Stephen Smee, J. Allyn Smith, S. Snedden, R. Stone, Chris Stoughton, Michael A. Strauss, Christopher Stubbs, Mark SubbaRao, Alexander S. Szalay, Istvan Szapudi, Gyula P. Szokoly, Anirudda R. Thakar, Christy Tremonti, Douglas L. Tucker, Alan Uomoto, Dan Vanden Berk, Michael S. Vogeley, Patrick Waddell, Shu-i. Wang, Masaru Watanabe, David H. Weinberg, Brian Yanny, Naoki Yasuda, and SDSS Collaboration. The Sloan Digital Sky Survey: Technical Summary. , 120(3):1579–1587, September 2000. doi: 10.1086/301513.

Ross Zhelem, Robert Content, Will Saunders, Jon Lawrence, Jessica Zheng, Julia Bryant, Joss Bland-Hawthorn, David Robertson, Mahesh Mohanan, and Sudharshan Venkatesan. The Hector Instrument: optical design of the new higher-resolution spectrograph. In Christopher J. Evans, Julia J. Bryant, and Kentaro Motohara, editors, *Ground-based and Airborne Instrumentation for Astronomy VIII*, volume 11447 of *Society of Photo-Optical Instrumentation Engineers (SPIE) Conference Series*, page 114478U, December 2020. doi: 10.1117/12.2562634.

Luwenjia Zhou, Christoph Federrath, Tiantian Yuan, Fuyan Bian, Anne M. Medling, Yong Shi, Joss Bland-Hawthorn, Julia J. Bryant, Sarah Brough, Barbara Catinella, Scott M. Croom, Michael Goodwin, Gregory Goldstein, Andrew W. Green, Iraklis S. Konstantopoulos, Jon S. Lawrence, Matt S. Owers, Samuel N. Richards, and Sebastian F. Sanchez. The SAMI Galaxy Survey: energy sources of the turbulent velocity dispersion in spatially resolved local star-forming galaxies. , 470(4):4573–4582, October 2017. doi: 10.1093/mnras/stx1504.

APPENDIX A:

The following pages contain additional plots, graphs, and tables for the results found in Chapter 5.

A.1 Mergers vs Isolated Global

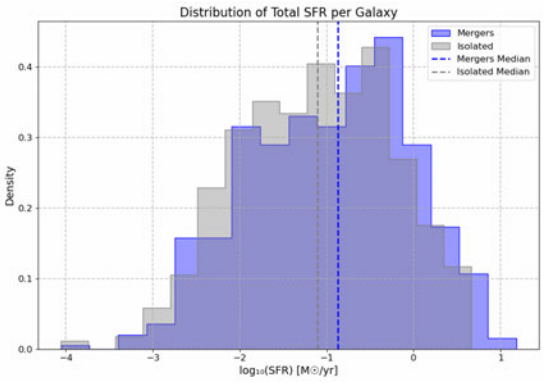

Figure A.1: Distribution of total SFR per galaxy

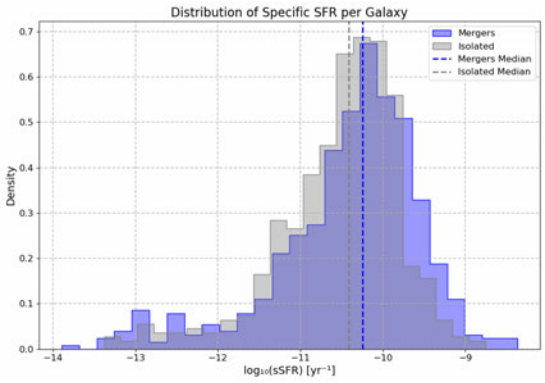

Figure A.2: Distribution of specific SFR per galaxy

Table A.1: Comparison of mergers vs isolated (mass-matched) galaxies using KS and MWU tests

Metric	KS statistic	KS p-value	MWU statistic	MWU p-value
logSFR	0.1043	0.00382	177852.0	0.001967
logSSFR	0.1352	5.54e-05	181598.0	0.0001607

A.2 Radial Bin

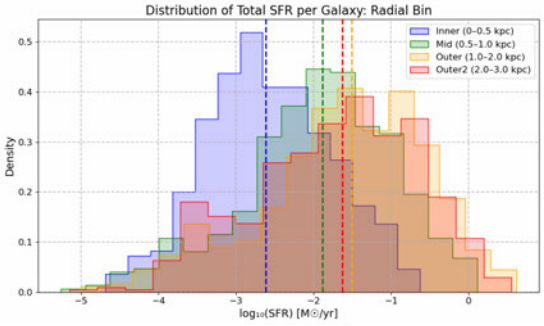

Figure A.3: Distribution of total SFR per galaxy - Radial binning

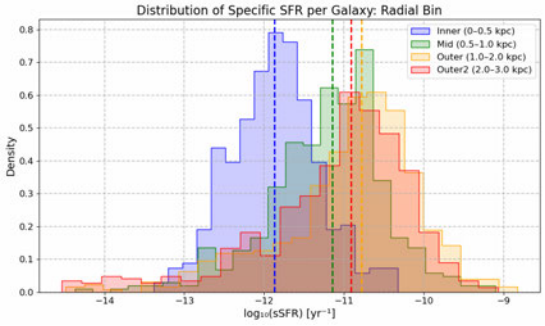

Figure A.4: Distribution of specific SFR per galaxy - Radial binning

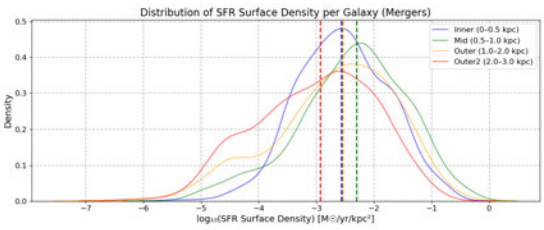

Figure A.5: Distribution of SFR surface density per galaxy - merging galaxies

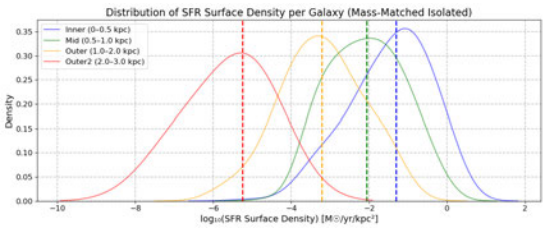

Figure A.6: Distribution of SFR surface density per galaxy - isolated galaxies

Table A.2: Comparison of mergers vs isolated (mass-matched) galaxies using KS and MWU tests

Metric	KS statistic	KS p-value	MWU statistic	MWU p-value
logSFR	0.1043	0.00382	177852.0	0.001967
logSSFR	0.1352	5.54e-05	181598.0	0.0001607

Table A.3: KS and MWU test results for radial bin comparisons of SFR and sSFR

Comparison	Metric	n_{bin1}	n_{bin2}	KS p-value	MWU p-value
Inner (0–0.5 kpc) vs Mid (0.5–1.0 kpc)	logSFR	379	468	1.42e-22	9.29e-25
Inner (0–0.5 kpc) vs Outer (1.0–2.0 kpc)	logSFR	379	535	2.46e-42	6.23e-45
Inner (0–0.5 kpc) vs Outer2 (2.0–3.0 kpc)	logSFR	379	574	2.71e-33	9.38e-36
Mid (0.5–1.0 kpc) vs Outer (1.0–2.0 kpc)	logSFR	468	535	6.25e-07	1.77e-08
Mid (0.5–1.0 kpc) vs Outer2 (2.0–3.0 kpc)	logSFR	468	574	1.45e-04	4.26e-04
Outer (1.0–2.0 kpc) vs Outer2 (2.0–3.0 kpc)	logSFR	535	574	9.45e-02	4.32e-02
Inner (0–0.5 kpc) vs Mid (0.5–1.0 kpc)	logSSFR	379	468	1.13e-44	7.25e-45
Inner (0–0.5 kpc) vs Outer (1.0–2.0 kpc)	logSSFR	379	535	1.62e-84	2.47e-64
Inner (0–0.5 kpc) vs Outer2 (2.0–3.0 kpc)	logSSFR	379	574	9.09e-67	2.09e-52
Mid (0.5–1.0 kpc) vs Outer (1.0–2.0 kpc)	logSSFR	468	535	7.05e-14	4.71e-13
Mid (0.5–1.0 kpc) vs Outer2 (2.0–3.0 kpc)	logSSFR	468	574	9.51e-07	3.67e-05
Outer (1.0–2.0 kpc) vs Outer2 (2.0–3.0 kpc)	logSSFR	535	574	8.39e-03	1.59e-03

Table A.4: KS and MWU test results for radial bin comparisons (Mergers only)

Comparison	Metric	n_{bin1}	n_{bin2}	KS p-value	MWU p-value
Inner (0–0.5 kpc) vs Mid (0.5–1.0 kpc)	logSFR	379	468	1.42e-22	9.29e-25
Inner (0–0.5 kpc) vs Outer (1.0–2.0 kpc)	logSFR	379	535	2.46e-42	6.23e-45
Inner (0–0.5 kpc) vs Outer2 (2.0–3.0 kpc)	logSFR	379	574	2.71e-33	9.38e-36
Mid (0.5–1.0 kpc) vs Outer (1.0–2.0 kpc)	logSFR	468	535	6.25e-07	1.77e-08
Mid (0.5–1.0 kpc) vs Outer2 (2.0–3.0 kpc)	logSFR	468	574	1.45e-04	4.26e-04
Outer (1.0–2.0 kpc) vs Outer2 (2.0–3.0 kpc)	logSFR	535	574	9.45e-02	4.32e-02
Inner (0–0.5 kpc) vs Mid (0.5–1.0 kpc)	SigmaSFR	379	468	1.02e-03	6.44e-04
Inner (0–0.5 kpc) vs Outer (1.0–2.0 kpc)	SigmaSFR	379	535	2.01e-02	7.45e-01
Inner (0–0.5 kpc) vs Outer2 (2.0–3.0 kpc)	SigmaSFR	379	574	3.02e-09	2.67e-09
Mid (0.5–1.0 kpc) vs Outer (1.0–2.0 kpc)	SigmaSFR	468	535	1.94e-03	2.01e-04
Mid (0.5–1.0 kpc) vs Outer2 (2.0–3.0 kpc)	SigmaSFR	468	574	1.12e-13	1.51e-19
Outer (1.0–2.0 kpc) vs Outer2 (2.0–3.0 kpc)	SigmaSFR	535	574	3.61e-05	4.49e-08

Table A.5: KS and MWU test results for radial bin comparisons (Isolated only)

Comparison	Metric	n_{bin1}	n_{bin2}	KS p-value	MWU p-value
Inner (0–0.5 kpc) vs Mid (0.5–1.0 kpc)	logSFR	497	534	4.54e-03	6.15e-03
Inner (0–0.5 kpc) vs Outer (1.0–2.0 kpc)	logSFR	497	513	9.55e-21	3.05e-22
Inner (0–0.5 kpc) vs Outer2 (2.0–3.0 kpc)	logSFR	497	6	1.62e-08	4.71e-09
Mid (0.5–1.0 kpc) vs Outer (1.0–2.0 kpc)	logSFR	534	513	1.84e-10	6.08e-15
Mid (0.5–1.0 kpc) vs Outer2 (2.0–3.0 kpc)	logSFR	534	6	1.67e-12	3.82e-12
Outer (1.0–2.0 kpc) vs Outer2 (2.0–3.0 kpc)	logSFR	513	6	1.37e-06	1.80e-06
Inner (0–0.5 kpc) vs Mid (0.5–1.0 kpc)	SigmaSFR	497	534	2.44e-17	6.69e-22
Inner (0–0.5 kpc) vs Outer (1.0–2.0 kpc)	SigmaSFR	497	513	1.67e-80	6.26e-95
Inner (0–0.5 kpc) vs Outer2 (2.0–3.0 kpc)	SigmaSFR	497	6	2.57e-12	2.75e-12
Mid (0.5–1.0 kpc) vs Outer (1.0–2.0 kpc)	SigmaSFR	534	513	7.91e-41	7.36e-56
Mid (0.5–1.0 kpc) vs Outer2 (2.0–3.0 kpc)	SigmaSFR	534	6	5.97e-14	5.97e-14
Outer (1.0–2.0 kpc) vs Outer2 (2.0–3.0 kpc)	SigmaSFR	513	6	3.98e-07	3.53e-07

Table A.6: KS and MWU test results for mergers vs isolated galaxies across radial bins

Comparison	Metric	$n_{mergers}$	$n_{isolated}$	KS p-value	MWU p-value
Mergers vs Isolated (Inner 0–0.5 kpc)	logSFR	379	497	1.60e-39	5.15e-45
Mergers vs Isolated (Mid 0.5–1.0 kpc)	logSFR	468	534	1.28e-02	3.87e-03
Mergers vs Isolated (Outer 1.0–2.0 kpc)	logSFR	535	513	1.26e-21	4.09e-22
Mergers vs Isolated (Outer2 2.0–3.0 kpc)	logSFR	574	6	2.31e-08	4.13e-09
Mergers vs Isolated (Inner 0–0.5 kpc)	SigmaSFR	379	497	1.60e-39	5.15e-45
Mergers vs Isolated (Mid 0.5–1.0 kpc)	SigmaSFR	468	534	1.28e-02	3.87e-03
Mergers vs Isolated (Outer 1.0–2.0 kpc)	SigmaSFR	535	513	1.26e-21	4.09e-22
Mergers vs Isolated (Outer2 2.0–3.0 kpc)	SigmaSFR	574	6	2.31e-08	4.13e-09

A.3 Separation

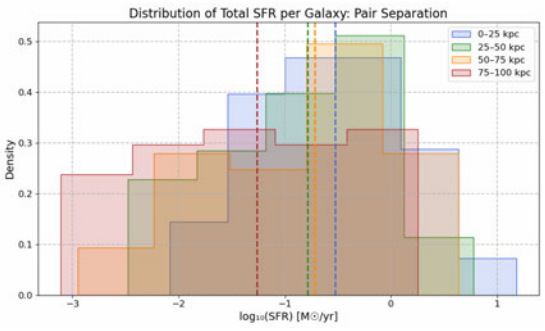

Figure A.7: Distribution of total SFR per galaxy - Pair Separation

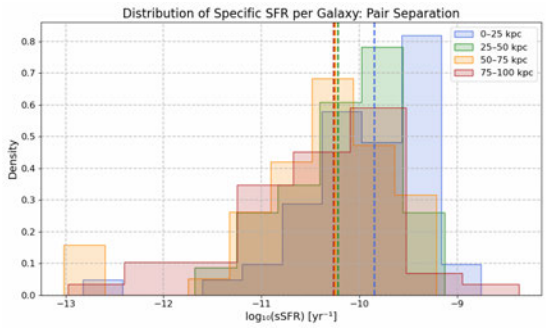

Figure A.8: Distribution of specific SFR per galaxy - Pair Separation

Table A.7: Global comparison of mergers vs isolated galaxies

Comparison	Metric	n-merg	n-iso	KS p-value	MWU p-value
Global	logSFR	601	535	0.003820	0.001967
Global	logSSFR	601	535	0.000055	0.000161

Table A.8: Radial separation comparisons of mergers vs isolated galaxies

Comparison	Metric	n1	n2	KS p-value	MWU p-value
0–25 kpc vs 25–50 kpc	logSFR	51	27	0.219308	0.182246
0–25 kpc vs 50–75 kpc	logSFR	51	45	0.116342	0.078056
0–25 kpc vs 75–100 kpc	logSFR	51	50	0.000399	0.000059
25–50 kpc vs 50–75 kpc	logSFR	27	45	0.505325	0.962891
25–50 kpc vs 75–100 kpc	logSFR	27	50	0.088744	0.043078
50–75 kpc vs 75–100 kpc	logSFR	45	50	0.058579	0.042245
0–25 kpc vs 25–50 kpc	logSSFR	51	27	0.094488	0.044850
0–25 kpc vs 50–75 kpc	logSSFR	51	45	0.004736	0.001404
0–25 kpc vs 75–100 kpc	logSSFR	51	50	0.004466	0.000377
25–50 kpc vs 50–75 kpc	logSSFR	27	45	0.606690	0.311561
25–50 kpc vs 75–100 kpc	logSSFR	27	50	0.469101	0.221590
50–75 kpc vs 75–100 kpc	logSSFR	45	50	0.963583	0.831774

A.4 Bar vs No Bar

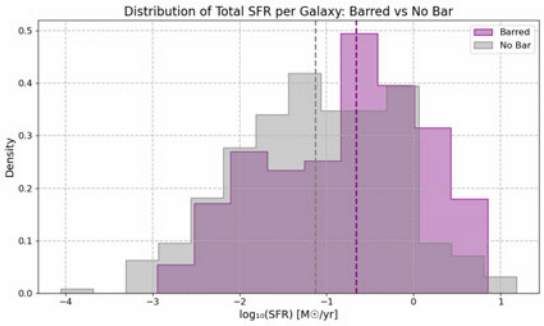

Figure A.9: Distribution of total SFR per galaxy - Barred vs Unbarred

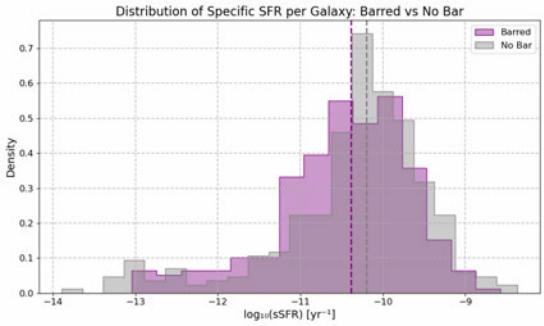

Figure A.10: Distribution of specific SFR per galaxy - Barred vs Unbarred

Table A.9: Comparison of barred vs non-barred galaxies - Global

Comparison	Metric	n-barred	n-nobar	KS p-value	MWU p-value
Barred vs No Bar	logSFR	263	338	0.000042	0.000028
Barred vs No Bar	logSSFR	263	338	0.007732	0.013865

Table A.10: KS and MWU test results for barred vs non-barred merger galaxies across radial regions

Region	Metric	n-barred	n-nobar	KS stat	KS p-value	MWU stat	MWU p-value
Inner	logSFR	236	313	0.053284	0.813594	37312.0	0.837445
Inner	logSSFR	236	313	0.077530	0.369139	35674.0	0.493654
Mid	logSFR	251	319	0.059062	0.681716	38850.0	0.544126
Mid	logSSFR	251	319	0.069540	0.477487	37946.0	0.284745
Outer	logSFR	218	291	0.045383	0.945432	31942.0	0.892211
Outer	logSSFR	218	291	0.049718	0.897490	30827.0	0.587171
Outer2	logSFR	91	126	0.099512	0.628385	6057.0	0.478442
Outer2	logSSFR	91	126	0.114774	0.449547	6024.0	0.524447

Table A.11: KS and MWU test results fpr barred vs non-barred isolated galaxies across radial regions

Region	Metric	n-barred	n-nobar	KS p-value	MWU p-value
Inner	logSFR	218	280	0.017333	0.045832
Inner	logSSFR	218	280	0.021865	0.005612
Mid	logSFR	225	279	0.003813	0.002193
Mid	logSSFR	225	279	0.129958	0.070381
Outer	logSFR	199	249	0.051210	0.011404
Outer	logSSFR	199	249	0.078000	0.173323
Outer2	logSFR	64	124	0.161428	0.179553
Outer2	logSSFR	64	124	0.184427	0.074065

A.5 Merger Ratio

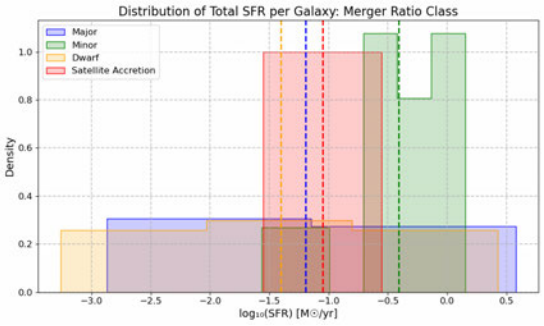

Figure A.11: Distribution of total SFR per galaxy - Merger Ratio Class

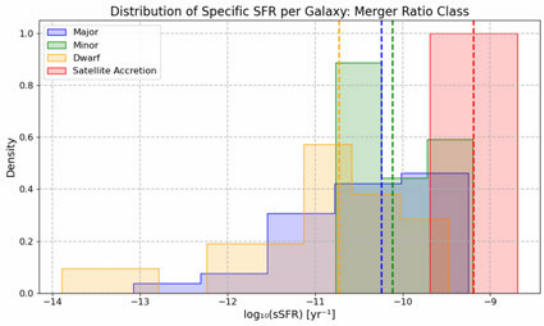

Figure A.12: Distribution of specific SFR per galaxy - Merger Ratio Class

Table A.12: KS and MWU test results for merger ratio class comparisons

Metric	Class 1	Class 2	n1	n2	KS p-value	MWU p-value
logSFR	Major	Minor	34	13	0.003602	0.006948
logSFR	Major	Dwarf	34	19	0.923878	0.649537
logSFR	Major	Satellite Accretion	34	1	0.971429	0.971429
logSFR	Minor	Dwarf	13	19	0.016956	0.041994
logSFR	Minor	Satellite Accretion	13	1	0.428571	0.428571
logSFR	Dwarf	Satellite Accretion	19	1	0.900000	0.900000
logSSFR	Major	Minor	34	13	0.218057	0.186857
logSSFR	Major	Dwarf	34	19	0.079522	0.046172
logSSFR	Major	Satellite Accretion	34	1	0.057143	0.057143
logSSFR	Minor	Dwarf	13	19	0.011059	0.002144
logSSFR	Minor	Satellite Accretion	13	1	0.142857	0.142857
logSSFR	Dwarf	Satellite Accretion	19	1	0.100000	0.100000

Table A.13: KS and MWU test results for merger classes across radial regions (Satellite Accretion excluded due to insufficient numbers)

Merger Class	Metric	Region 1	Region 2	n1	n2	KS p-value	MWU p-value
Major	logSFR	Inner	Mid	31	31	0.823454	0.592660
Major	logSFR	Inner	Outer	31	28	0.039863	0.079564
Major	logSFR	Inner	Outer2	31	11	0.000076	0.000224
Major	logSFR	Mid	Outer	31	28	0.039863	0.005101
Major	logSFR	Mid	Outer2	31	11	0.000036	0.000014
Major	logSFR	Outer	Outer2	28	11	0.020472	0.002111
Major	logSSFR	Inner	Mid	31	31	0.413545	0.499186
Major	logSSFR	Inner	Outer	31	28	0.173014	0.079564
Major	logSSFR	Inner	Outer2	31	11	0.001602	0.001355
Major	logSSFR	Mid	Outer	31	28	0.050314	0.024187
Major	logSSFR	Mid	Outer2	31	11	0.000392	0.000313
Major	logSSFR	Outer	Outer2	28	11	0.100618	0.047502
Minor	logSFR	Inner	Mid	11	11	0.832588	0.843831
Minor	logSFR	Inner	Outer	11	10	0.523787	0.378738
Minor	logSFR	Inner	Outer2	11	4	0.063004	0.039560
Minor	logSFR	Mid	Outer	11	10	0.258610	0.341786
Minor	logSFR	Mid	Outer2	11	4	0.021978	0.017582
Minor	logSFR	Outer	Outer2	10	4	0.409590	0.187812
Minor	logSSFR	Inner	Mid	11	11	0.832588	1.000000
Minor	logSSFR	Inner	Outer	11	10	0.523787	0.597406
Minor	logSSFR	Inner	Outer2	11	4	0.098168	0.055678
Minor	logSSFR	Mid	Outer	11	10	0.607514	0.418052

Continued on next page

Table A.13 – continued from previous page

Merger Class	Metric	Region 1	Region 2	n1	n2	KS p-value	MWU p-value
Minor	logSSFR	Mid	Outer2	11	4	0.035165	0.077656
Minor	logSSFR	Outer	Outer2	10	4	0.259740	0.239760
Dwarf	logSFR	Inner	Mid	14	14	0.999592	0.872238
Dwarf	logSFR	Inner	Outer	14	13	0.145759	0.076527
Dwarf	logSFR	Inner	Outer2	14	4	0.071895	0.232680
Dwarf	logSFR	Mid	Outer	14	13	0.288792	0.166666
Dwarf	logSFR	Mid	Outer2	14	4	0.141176	0.232680
Dwarf	logSFR	Outer	Outer2	13	4	0.704202	0.623529
Dwarf	logSSFR	Inner	Mid	14	14	0.635485	1.000000
Dwarf	logSSFR	Inner	Outer	14	13	0.012633	0.034782
Dwarf	logSSFR	Inner	Outer2	14	4	0.141176	0.277124
Dwarf	logSSFR	Mid	Outer	14	13	0.077703	0.068800
Dwarf	logSSFR	Mid	Outer2	14	4	0.141176	0.277124
Dwarf	logSSFR	Outer	Outer2	13	4	0.294118	0.295798

A.6 Morphology

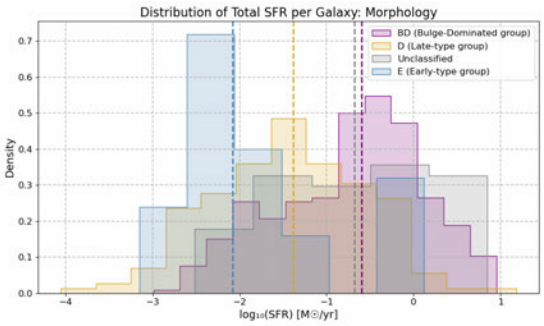

Figure A.13: Distribution of total SFR per galaxy - Morphology

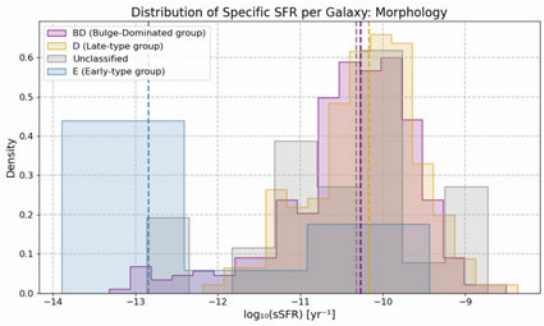

Figure A.14: Distribution of specific SFR per galaxy - Morphology

Table A.14: KS and MWU test results for morphology groups across radial regions - Mergers vs Isolated comparison

Morphology Group	Region	Metric	n-merg	n-iso	KS p-value	MWU p-value
BD	Inner	logSFR	283	309	0.534564	0.246713
BD	Inner	logSSFR	283	309	0.049791	0.125843
BD	Mid	logSFR	299	315	0.550877	0.229688
BD	Mid	logSSFR	299	315	0.219323	0.444742
BD	Outer	logSFR	259	276	0.795192	0.861170
BD	Outer	logSSFR	259	276	0.034048	0.035140

Continued on next page

Table A.14 – continued from previous page

Morphology Group	Region	Metric	n-merg	n-iso	KS p-value	MWU p-value
BD	Outer2	logSFR	116	116	0.676332	0.734284
BD	Outer2	logSSFR	116	116	0.784163	0.487971
D	Inner	logSFR	146	157	1.40e-07	3.82e-08
D	Inner	logSSFR	146	157	5.33e-04	1.09e-03
D	Mid	logSFR	152	155	7.06e-07	1.09e-06
D	Mid	logSSFR	152	155	7.28e-03	8.71e-02
D	Outer	logSFR	142	138	7.87e-04	2.53e-04
D	Outer	logSSFR	142	138	2.09e-01	8.51e-01
D	Outer2	logSFR	58	52	4.24e-03	1.37e-03
D	Outer2	logSSFR	58	52	6.09e-01	9.88e-01
Unclassified	Inner	logSFR	107	23	0.886835	0.941638
Unclassified	Inner	logSSFR	107	23	0.574468	0.541797
Unclassified	Mid	logSFR	106	25	0.720871	0.679662
Unclassified	Mid	logSSFR	106	25	0.267836	0.164209
Unclassified	Outer	logSFR	96	24	0.628313	0.480632
Unclassified	Outer	logSSFR	96	24	0.133083	0.086226
Unclassified	Outer2	logSFR	37	11	0.204939	0.128297
Unclassified	Outer2	logSSFR	37	11	0.886213	0.787292
E	Inner	logSFR	13	9	0.839685	1.000000
E	Inner	logSSFR	13	9	0.640135	0.504274
E	Mid	logSFR	13	9	0.723650	0.640181
E	Mid	logSSFR	13	9	0.556415	0.504274
E	Outer	logSFR	12	10	0.557718	0.448279
E	Outer	logSSFR	12	10	0.557718	0.766679
E	Outer2	logSFR	6	9	0.408392	0.606993
E	Outer2	logSSFR	6	9	0.779421	0.455944